Study of Heat Transfer in Circular Tubes with Supercritical Fluid by the STAR-CCM+ CFD Code

A thesis presented to the:

Department of NUCLEAR ENGINEERING, COLLEGE OF BASIC AND APPLIED SCIENCES, UNIVERSITY OF GHANA

By

(LUCKY FINIDEI WOKO, 10444961)

B.Eng. (Nigeria), 1998

In partial fulfillment of the requirements for the degree of

MASTER OF PHILOSOPHY

in

NUCLEAR SCIENCE AND TECHNOLOGY.

July, 2015

DECLARATION

This thesis is the result of research work undertaken by Lucky Finidei Woko in the Department of Nuclear Engineering School of Basic and Applied Sciences, University of Ghana, under the supervision of Dr. Seth Kofi Debrah and Dr. Vincent Yao Agbedemegbe.

LUCKY FINIDEI WOKO

Date: ----------

.

---------- ----------

Seth Kofi Debrah, Ph.D **Vincent Yao Agbodemegbe, Ph.D**

(Principal Supervisor) **(Co-Supervisor)**

Date: ---------- **Date:** ----------

ABSTRACT

Supercritical Cooled-Water Reactor (SCWR) which is planned to be deployed by 2030 derives its concept from Light Water Reactors (Boiling Water Reactor (BWR), Pressurized Water Reactor (PWR) and Fossil Fired Coal Plant but with a simpler design. Due to the strong variations of density at supercritical pressure, the SCWR is likely to inherit some of the issues related to the LWR's in terms of heat transfer (e.g. thermal crisis). This research was undertaken in order to better understand the phenomena of heat transfer as applied to SCWR and also to test the applicability of Reynolds-Average Navier-Stokes (STAR-CCM$^+$ CFD code). Kim's et al., (2005) data which employs supercritical CO_2 as a simulant of water at 8 MPa was used to test the applicability. The computational simulation by STAR-CCM$^+$ on the prediction of a 2-D axisymmetric heat transfer of carbon dioxide at supercritical pressure flowing upward through heated cross-section of a circular tube was performed with six (6) low-Reynolds number models; κ-epsilon AKN, EB, standard low-Re and V2F with two κ-ω turbulence models; SST and standard Wilcox with low y+ wall treatment. The results of heat fluxes of 20, 23, 30 and 40 kW/m^2 and mass flux of 314 kg/m^{2}s were compared to the experimental data of Kim et al., (2005). The Standard low-Reynolds turbulence models were seen to have better capabilities to predict the heat transfer behaviour of supercritical CO_2 as observed in the experiment. The κ-ω models did not perform favourably in the prediction of heat transfer deterioration. The V2F turbulence model performed better than the other models quantitatively when compared to the experimental data. The results of the simulation has been found to be able to reproduce the general features exhibited in the experimental data even though they over predicted the observed heat transfer deterioration both quantitatively and qualitatively.

DEDICATION

I dedicate this thesis work to Dr. Franklin Erepamo Osaisai for his encouragement and support to my educational career and my lovely wife Tessy Ifeoma Ayebatonye Woko for her care, love, support and understanding during the period of my study.

ACKNOWLEDGEMENT

I would like to express my sincere gratitude to Dr. Seth Kofi Debrah, Dr. Vincent Yao Agbodemegbe, Prof. Emeritus E. H. K Akaho and Dr. Emmanuel Ampomah-Amoako for their valuable guidance and support throughout my research work.

I would like thank the IAEA for the financial support throughout the period of my studies.

Special thanks also go to Dr. Franklin Erepamo Osaisai for his encouragement and valuable pieces of advice.

I would like to thank my mates at the School of Nuclear and Allied Sciences, College of Basic and Applied Sciences, University of Ghana who helped me through long discussions on technical details of my research, and the developers of the STAR-CCM+ CFD code software CD-Adapco which was used for the simulation of this research work.

I would also like to thank the Nigeria Atomic Energy Commission (N.A.E.C) for the opportunity given to me to undergo this course and my dear wife Tessy I. A. Woko for her care, love and support during the period of this research work.

TABLE OF CONTENTS

LIST OF FIGURES

NOMENCLATURE

Roman Letters	Description	Units
c_p	Specific Heat Capacity	[J/kg K]
D	Diameter	[m]
D_h	Hydraulic Diameter	[m]
f	Damping Functions	[-]
g	Gravity Acceleration	[m/s^2]
h	Enthalpy	[J/kg]
κ	Turbulence Kinetic Energy	[m^2s^2]
P	Pressure	[MPa]
Pr	Prandtl Number	[-]
Re	Reynolds Number	[-]
T	Temperature	[^{o} C]
U	Velocity	[m/s]
y +	Dimensionless Distance from the Wall	[-]

Greek Letters

ρ	Density	[kg/m^3]
μ	Dynamic viscosity	[kg/m s]
μ_t	Dynamic turbulence viscosity	[kg/m^2]
Δ	Difference	[-]
α	Heat transfer coefficient	[W/m^{2}K]
ε	Turbulence dissipation energy	[m^2 s^3]

Subscripts

b	Bulk
MWe	Megawatt Electricity
Mth	Megawatt Thermal
Pc	Pseudo Critical
SC	Supercritical
Tpc	Pseudo Critical Temperature
w	Wall

Abbreviations

2D	Two Dimension
3D	Three Dimension
ABWR	Advanced Boiling Water Reactor
AKN	Abe-Kondoh-Nagano
ANFIS	Adaptive Network-based Fuzzy Inference System
BWR	Boiling Water Reactor
CANDU	Canadian Deuterium Uranium
CFD	Computational Fluid Dynamics
CO_2	Carbon dioxide
DC	Direct Current
DNS	Direct Numerical Simulation
EB	Elliptic blending
ELFR	European Lead Fast Reactor
ELSY	European Lead-Cooled System
EPR	European Power Reactor
ESBWR	Economic Simplified Boiling Water Reactor
GFR	Gas-Cooled Fast Reactor
GIF	Generation IV International Forum
GT-MHR	Gas Turbine Modular Helium Reactor
HTD	Heat Transfer Deterioration
HTR	High Temperature Reactor

LFR	Lead-Cooled Fast Reactor
LOCA	Loss of Coolant Accident
LWR	Light Water Reactor
MSR	Molten Salt Fast Reactor
OECD	Organization for Economic Cooperation and Development
PBMR	Pebble Bed Modular Reactor
PFBR	Prototype Fast Breeder Reactor
PHWR	Pressurized Heavy Water Reactor
PWR	Pressurized Water Reactor
RANS	Reynolds-Averaged Navier-Stokes
RBMK	Reactor Bolshoy Moshchnosty Kanalny
RSME	Root Mean-Square Error
SCW	Supercritical Water
SCWR	Supercritical Water-Cooled Reactor
SFR	Sodium-Cooled Fast Reactor
SMR	Small Modular Reactor
SST	Shear Stress Transport
SSTAR	Small Secure Transportable Autonomous Reactor
STAR-CCM+	Simulation of Turbulent flow in Arbitrary Regions Computational Continuum Mechanics C ++ based
V2F	k-Ɛ-$\overline{v^2}$-f

CHAPTER ONE: BACKGROUND OF RESEARCH

1.0 INTRODUCTION

Supercritical fluids have been under investigation since the 1950's [1] and had been found attractive for the thermal power industry around the world. Research in this area was mainly preformed in the former USSR and in the USA in the 1950s to 1980s [1]. Studies were conducted in the early 1960s to investigate the possibility of using supercritical water in nuclear reactors [2]. The Supercritical Water Reactor (SCWR) is one of the six reactor technologies selected for research and development under the Generation IV program. SCWRs are basically light water reactors (LWRs) operating at higher pressures and temperatures with direct once-through cycle, simpler design and it draws its experience from PWR, BWR and fossil fired coal plants [3]. The SCWRs are advanced nuclear systems because of their high thermal efficiency (i.e., about 45% as compared to the current conventional plants of about 33%) [4]. This reactor concept is expected to be operational by the year 2030 and supposed to be operated at a pressure of 25 MPa with an inlet and outlet temperature of about 280 ^{o}C and 500 ^{o}C respectively [5]. SCWR is one of the six (6) promising reactor concepts chosen by the Generation IV International Forum (GIF) to address the following:

Sustainability: the sustainability goals include proper utilization of fuel through innovative fuel cycles, environmental protection, enhancing the ability of future generations to meet society's needs.

Economics: economics is an essential goal for the Generation IV to produce nuclear energy at competitive costs. These goals can be achieved through innovative advances in plant

designs, improved efficiency, plant simplification and allowance for the production of hydrogen, fresh water, district heating and other energy by-products.

Safety and reliability: Generation IV will pursue improved accident management, reduced need for off-site emergency response, more enhanced use of passive safety features and increased public confidence in nuclear energy.

Proliferation resistance and physical protection: it is required that the Generation IV systems increase the security for guarding nuclear materials against thefts, preventing the use of civilian nuclear establishments for proliferation of nuclear weapons and also increasing the robustness of the system against terrorist attacks.

1.1 Evolution of Nuclear Reactors

There are different generations of nuclear reactors over the past six to seven decades. Thus, a chronological approach has been taken by the research to start an overview and development of various nuclear power reactors**.** The following are the generations of nuclear reactors presented in Figure 1.1

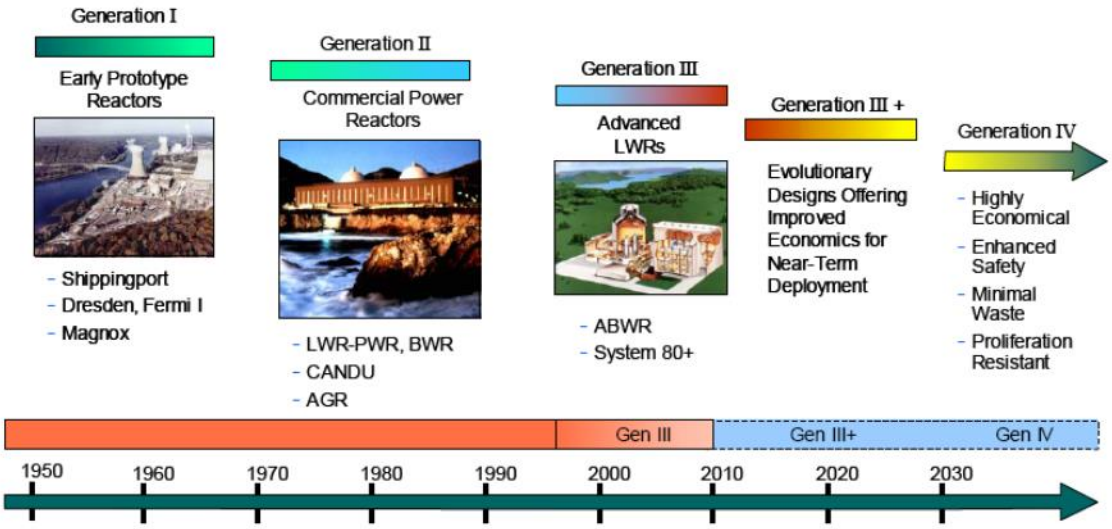

Figure 1.1: Chronological Roadmap for Nuclear Energy Systems [6]

Generation-I Reactors: These are reactors built in the initial period (1950s and 1960s) of nuclear power expansion and generally had primitive design features. All of these reactors have been shut down. Examples of such reactors are Magnox reactor (Calder Hall reactor in the United Kingdom) and first commercial power reactor at Shipping port in 1957 (in the state of Pennsylvania in the United States).

Generation-II Reactors: Most of the commercial nuclear power plants operating today are of Generation- II type and have been in operation since 1970s. These reactors incorporated improved design and safety features and productivity over Generation-I reactors. In the Western Hemisphere, a majority of commercial nuclear power plants have light water reactor (LWR), both pressurized water reactor (PWR) and boiling water reactor (BWR). It is important to note that LWRs were also built as Generation-I reactors (such as Shipping port facility with 60 MWe power capacity). Another variety is the CANDU (Canadian Deuterium Uranium) reactor, which is basically a pressurized heavy water reactor (PHWR).There are a few different versions of pressurized water reactors (e.g., RBMK type) in Russia and former Soviet-bloc countries. Generation-III and III+ Reactors: New

reactors being built or will be built within a few years are of Generation-III and III+ category. These are mainly advanced LWRs. Examples include advanced boiling water reactor (ABWR) and evolutionary or European power reactor (EPR). In the same line, Generation III+ category aims to provide reactor systems that have much improved designs and safety features, and much greater capacities. Notably, all these reactors are thermal in nature. Generation-IV reactors: They are the futuristic reactors for which research and development efforts are currently in progress. These reactors will be more efficient, safer, longer lasting (60 years and beyond), proliferation-resistant, and economically viable compared to the present nuclear reactors. Out of about 100 reactor concepts presented to GIF, only six reactor design concepts were considered as reasonable candidates for further research and development on the future Generation IV. The following are the six Gen-IV reactors: Gas-Cooled Fast Reactor (GFR), Lead-Cooled Fast Reactor (LFR), Molten Salt Reactor (MSR), Sodium-Cooled Fast Reactor (SFR), Supercritical-Water-Cooled Reactor (SCWR) and Very-High-Temperature Reactor (VHTR).

1.2 **SCWR Plant Concept**

SCWR is basically LWR which operates at higher pressure of 25 MPa as opposed to 15 MPa for PWR and higher temperatures of 500 ^{o}C as compared to 320 ^{o}C for PWR with a direct once through cycle [7]. Operating the reactor above the critical pressure (22.1 MPa) of coolant (water) eliminates coolant boiling, so the coolant remains in single-phase throughout the reactor system. Thus the need for recirculation and jet pumps, pressurizer, steam generators, steam separators and dryers is eliminated [8] as shown in Figure 1.2

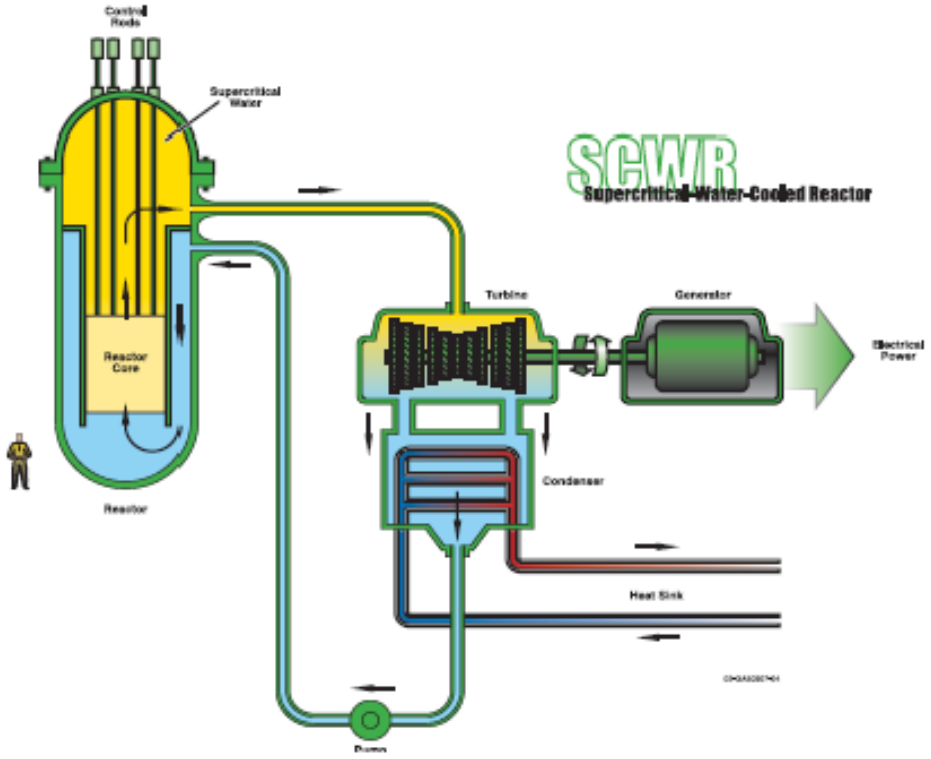

Figure 1.2: Schematic of a Supercritical Water Reactor [9]

The SCWR core average power density is about 70 kW/L (i.e., between the power density of boiling water reactors (BWRs) and PWRs). The reactor coolant system of the SCWR comprises the feed water lines and main steam lines up to the outermost set of containment isolation valves. Similar to a BWR, the SCWR uses two feed water lines made of carbon steel. However it has been determined that because of its high-density steam, the SCWR needs only two steam lines as opposed to four in a BWR of similar thermal power. This further adds to the economic strength of the SCWR concept. A pressure-suppression type containment with a condensation pool, essentially the same design as modern BWRs, was selected. The dry and wet well volumes were calculated to limit the pressure build-up to

typical BWR levels following a LOCA or a severe accident with core melting. The condensation pool water inventory was designed to provide ample margin for residual heat removal and meet the requirement that active safety systems are not needed during the first 24 hours following an initiating event resulting in a severe accident [10].

1.3 Thermodynamic Characteristics of Supercritical Fluid at Supercritical Pressures.

Supercritical fluids are often adopted as working fluids in fossil-fuelled power plants.

From the physical-chemical standpoint supercritical fluids have high diffusion rates and a remarkable ability to dissolve materials which make them a suitable and environmentally acceptable alternative to conventional organic solvents, carbon dioxide and water, for instance, are used for this purpose [11]. The thermodynamic critical point represents the highest temperature and pressure at which a substance can exist as saturated liquid and saturated vapor in equilibrium. Above the critical point the two distinct phases no longer exist, resulting in a single homogenous phase of supercritical fluid.

The properties of both water and CO_2 in the region of interest to this work are briefly described, since they have a strong influence on the behavior of the thermodynamic characteristics of the system. CO_2 is considered in this work as it is often preferred to be used in experiments because of its low critical pressure and temperature, thus facilitating the design, construction and operation of experimental apparatuses. The critical pressure and temperature for CO_2 are approximately 7 MPa and 31 ^{o} C [12]. At the critical pressure and temperature fluid initially undergo a relatively slow change in density with temperature and then, in a temperature range that is very narrow especially at pressures close to the

critical pressure, the density decreases sharply; i.e., the fluid changes from a high density, liquid-like fluid to a low density, gas-like fluid. However, with respect to an actual phase change, the process is gradual and without discontinuities.

Thermodynamic properties and transport properties at subcritical pressures change discontinuously or reach a maximum at the saturation line; so, the saturation line represents the locus of discontinuities at subcritical pressure [13]. On the other hand, at supercritical pressures, different thermodynamic and transport properties reach a maximum value at different temperatures. Moreover, while at subcritical pressures phase change is accompanied by absorption of energy and increase of specific heat at constant temperature, the transition at supercritical pressures is accompanied by a rather sharp peak in specific heat which makes the temperature to increase very slowly with heat input in the range of its occurrence [14]. The temperature at which the specific heat reaches a maximum is termed "pseudo-critical temperature" at the given operating pressure. The height of these specific heat peaks decreases with increasing pressure. This has an impact on the design of supercritical fossil fired boilers and of the core of supercritical reactors [15].

1.4 **Heat transfer characteristics**

The transfer of heat at supercritical pressure is mainly due to the thermal physical properties which vary strongly near pseudo-critical line. The line connecting the maximum values of specific heat is called the pseudo-critical line. The pseudo-critical temperature increases with increasing pressure. At a pressure of 25 MPa the pseudo-critical temperature is $384^{O}C$, near the pseudo-critical line the density decreases dramatically, which result in strong buoyancy and acceleration effects. The transport of heat by fluid is known as convection and its efficiency and conduction depends greatly on the fluid velocity and the

thermal properties of the medium. The effectiveness of heat transfer may become high near the pseudo-critical region temperature, this is caused primarily because of high value of specific heat under such conditions [16].

1.4.1 Forced convection

Convection is the mechanism of heat transfer through fluid in the presence of bulk fluid motion. The fluid in forced convection is forced to flow over a surface or a tube by external means such as pump or fan. The mechanism of heat transfer is complicated since it involves fluid motion as well as the conduction of heat. The fluid motion enhances heat transfer, as the velocity is high the heat transfer rate is higher. The convective heat coefficient h strongly depends on the fluid properties and the roughness of the solid structure and the type of fluid flow (laminar or turbulent) [17].

1.4.2 Mixed Convection

Mixed (combined) convection is a combination of forced and natural or (free) convections which is determined simultaneously by both an outer forcing system and inner volumetric (mass) forces, viz., by the non-uniform density distribution of a fluid medium in a gravity field. However, mixed convection is found in the systems of much smaller scales, i.e., in many engineering devices. Heating or cooling of channel walls, and at the small velocities of a fluid flow that are characteristic of a laminar flow, mixed convection is almost always realized. Studies of turbulent channel flows with substantial gravity field effects have actively developed since the 1960s after their becoming important in engineering practice by virtue of the growth of heat loads and channel dimensions in modern technological applications (thermal and nuclear power engineering, pipeline transport) [18].

1.4.2.1 Influence of Buoyancy

For a downward heated flow there is a continuous enhancement in heat transfer as buoyancy becomes relatively stronger. This behavior has been found with many fluids at supercritical pressure and also with other fluids. Not only is the heat transfer improved, but wall temperatures are less sensitive to heat flux.

Hall and Jackson [19] proposed a mechanism for which buoyancy will affect the heat transfer. The dominant factor is the modification of the shear stress distribution across the pipe, with a consequential change in turbulence production.

As mentioned before, buoyancy effects are also noticed in horizontal flows. Due to a stratification of the flow, the hotter (less dense) fluid can be found in the upper part of the pipe. There may also be an effect due to the damping effect of the stabilizing density gradient on turbulence near the upper surface of the pipe. At the lower surface heat transfer is frequently better than for forced convection alone, suggesting that there may be some amplification of turbulence by the destabilizing density gradient in this region.

Experiment performed by Belyakov et al. [20] show some measurements for heat transfer to supercritical water in horizontal pipes. The deterioration of the upper surface occurs progressively along the pipe and does not show the sharp peaks that are obtained with upward flow. As the ratio of the heat flux to the mass flow flux increases, the wall temperature and thus deterioration at the upper surface increases.

1.4.3 Influence of flow acceleration

Serious heat-transfer deterioration may occur in fluids at supercritical pressure owing to the effects of buoyancy, flow acceleration, and significant variations in thermo-physical

properties. Although there have been numerous experimental studies on this subject, no single heat-transfer correlation has been found to be capable of describing this phenomenon accurately. Relatively few experimental studies have been carried out on the fluid mechanics of supercritical flows because of the technical difficulties of dealing with turbulent flows and high heat fluxes simultaneously. Conversely, many computational fluid dynamics studies have examined a number of low-Reynolds number turbulence models. However, none have reproduced the buoyancy production of turbulence reasonably well because of limitations with the use of a constant turbulent Prandtl number. Direct numerical simulations (DNS) may provide more insight into the physics of fluids at supercritical pressure within a limited range of flow and heat-transfer conditions [19].

1.4.4 Heat Transfer Deterioration

Heat transfer deterioration is characterized with low values of wall heat transfer coefficient compared to those of normal heat transfer and hence have higher values of wall temperature within some part of the test section or the entire test section. Near the pseudo critical line the density decreases dramatically. There exist a large peak of thermal expansion coefficient which behaves very similar to the specific heat. The thermal conductivity decreases with increasing temperature, the thermal conductivity decreases sharply beyond the pseudo critical point with the dynamic viscosity also, due to sharp increase in specific heat capacity there exist a large peak of the Prandtl number at the pseudo critical point. With large increase in wall temperature, a strong reduction of heat transfer coefficient occur when the heat flux is high and the mass flux is low. Heat transfer deterioration is due

to buoyancy effect and the flow acceleration in the near-wall region due to rapid decrease in the fluid density near pseudo critical temperature [20].

1.4.5 Heat Transfer Enhancement

Heat transfer enhancement occurs mainly at low heat fluxes and at a bulk fluid temperature close to pseudo-critical region, which is mainly due to the increase in the specific heat. The effectiveness of heat transfer may become high near the pseudo critical region temperature, this is due to the high specific heat under such conditions. At pressure above critical point, fluid remain in single phase regardless of the enthalpy, and at such conditions they experience large variations in density and transport properties as temperature varies. The enhancement of heat transfer can be reduced with the increase in heat flux as a result of non-uniformity of density along the heated channel [20].

1.5 **PROBLEM STATEMENT**

The large variations in the properties of fluid at supercritical pressure pose problems to be handled. The change in the properties of fluid especially the coolant density which decreases from about 760 kg/m^3 at the core inlet to about 90 kg/m^3 at the core outlet of the reactor is large enough to raise problems that relate to those observed in boiling channels (i.e., critical heat flux and departure from nucleate boiling DBN), Due to the sharp variations of fluid properties in the supercritical region, phenomenon like heat enhancement and deterioration observed at sufficiently low and high heat-flux to mass-flux ratios, respectively, challenge the capabilities of engineering correlations. The

phenomenon of heat transfer to supercritical fluid is not fully understood and the STAR-CCM+ CFD code has not been fully explored in this area of science. For this reason an in-depth analysis is necessary to understand this phenomenon so as to perform accurate heat transfer predictions for use in SCWR design.

1.6 OBJECTIVES OF RESEARCH

The main objective of this research is to study the heat transfer to supercritical fluid in a circular tube using STAR-CCM+ CFD code. The investigation will therefore focus on the following:

- Perform a 2-D analysis of heat transfer to supercritical fluid in a circular tube with validation data from Kim et al., (2005) [21] and to determine the effect of heat transfer deterioration and enhancement with supercritical fluid at both low and high heat fluxes.
- To determine the effectiveness of Reynolds-Averaged Navier-Stokes (RANS) model to predict the heat transfer in supercritical fluid.

1.7 JUSTIFICATIONS

The research activities going on in the transfer of heat in tubes in the Supercritical Water Reactor (SCWR) over the years has identified some technological gaps that need more research, due to frictional, acceleration and buoyancy forces which exist near the heated wall. The study of heat transfer with supercritical fluid is complex, due to the strong variations of thermal-physical properties, especially near the pseudo-critical point, strong buoyancy effect and acceleration exist near the heated wall. Due to this strong variations of density and transport properties as temperature varies at these conditions, the heat

transfer to supercritical fluids in circular tubes is done with the purpose of predicting the convective heat transfer to fluids at supercritical pressure**.**

1.8 SCOPE

The scope of this research is limited to simulating two dimensional analysis (2D) axi-symmetric analysis using Computational Fluid Dynamics (CFD) code STAR-CCM+ to test the applicability of the low-Reynolds turbulence models and also determine the effect of heat transfer deterioration and enhancement to supercritical fluids at both low and high heat fluxes.

1.9 THESIS ORGANIZATION

Chapter One presents the introduction of the thesis work with a brief historical background of the supercritical water cooled reactor (SCWR), evolution of nuclear reactors , SCWR Plant concept, thermodynamic characteristics of supercritical fluids, Heat transfer characteristics, Goals and objectives, Problem statement, as well as the Relevance and justification.

Chapter Two discusses a review of the literature of the six Generation IV International Forum (GIF) nuclear reactor objective and the concept of the thermal reactors; The Very-high temperature reactor (VHTR), Molten-salt reactor (MSR), the Gas-cooled fast reactor (GFR), the Lead-cooled fast reactor (LFR), Sodium-cooled fast reactor (SFR), history of supercritical water in power engineering application, history of fossil-fired supercritical power plants, Supercritical-water-cooled reactor (SCWR), Major Advances in SCWR

development in the last decade, heat Transfer Experiments with Supercritical CO_2 as well as heat transfer numerical experiments with supercritical fluids.

Chapter Three presents the adopted STAR-CCM+ model choice for the current study, the six turbulence models used, the basic transport equation in the axisymmetric flow in the STAR-CCM+ code, the experimental conditions, the experimental data, the geometry and meshing parameters, the fluid physics, the simulation as well as the Governing equations of axisymmetric fluid flow in the STAR-CCM+.

Chapter Four presents the results obtained and discussions from computational simulation of the work done with the low Reynolds number turbulent models for predicting the heat transfer on circular tube with supercritical fluid and the comparison of the simulation with the experimental data for validation and the observations that are made from the analysis.

Chapter Five provides the general conclusions made from the different turbulence models, the behavior of the κ-ε and the κ-ω models and how they respond to the heat transfer at low and high heat fluxes and outlines possible areas of further studies, as well as the recommendations made.

CHAPTER TWO: LITERATURE REVIEW

This chapter deals with the various issues related to Supercritical Water (SCW) applications and SCWR heat transfer characteristics, previous important studies carried out over the years and the diverse techniques in the field of experimental heat transfer and numerical experimentation of heat transfer.

2.1 The Generation IV Nuclear Reactors

In January 2000, The Generation IV International Forum (GIF) was established with the objective of investigating innovative nuclear energy system concepts to meet future energy challenges. The GIF members include Argentina, Brazil, Canada, France, Japan, South Africa, South Korea, Switzerland, United Kingdom, and United States. OECD-Nuclear Energy Agency and the International Atomic Energy Agency are mandated as permanent observers. In July 2006 the GIF voted unanimously to accept the membership of China and Russia, with formal entry expected in November of 2006 [22]. The evolution of the current nuclear power plants can be divided into generations as already elaborated in Section 1.1 of this thesis. The next generation of nuclear energy systems, generation IV, must be licensed, constructed and operated to supply competitive energy price. Generation IV reactors are a set of mostly theoretical nuclear reactor designs currently being researched around the world. Most of these designs are generally not expected to be available for commercial construction before 2030 [23]. The Generation IV Nuclear Reactors comprises of three thermal reactor and three fast reactors. The Thermal Reactors utilizes slow or thermal neutrons and a moderator is used to slow the neutrons emitted by fission to make them more likely to be captured by fuel while the fast reactors directly uses the fast neutrons

emitted by fission with little or no moderation. The selected Gen-IV Reactors are listed below:

2.1.1 Very-high-temperature reactor (VHTR)

This is a thermal-neutron-spectrum reactor and it produces hydrogen through high-temperature electrolysis and process heat. Graphite is used as the moderator while helium is used as the coolant. The inlet temperature is 640 ^{0}C and the outlet temperature is 1000 ^{O}C, at a pressure of 7 – 9 MPa [24]. Due to such high outlet temperatures, the thermal efficiency of VHTR is projected to be above 50% and it also becomes extremely attractive for chemical, oil and iron industries. The electric power conversion may employ either a direct (helium gas turbine) or indirect (gas mixture turbine) Brayton cycle. A reference VHTR system that produces hydrogen is shown in Figure 2.1

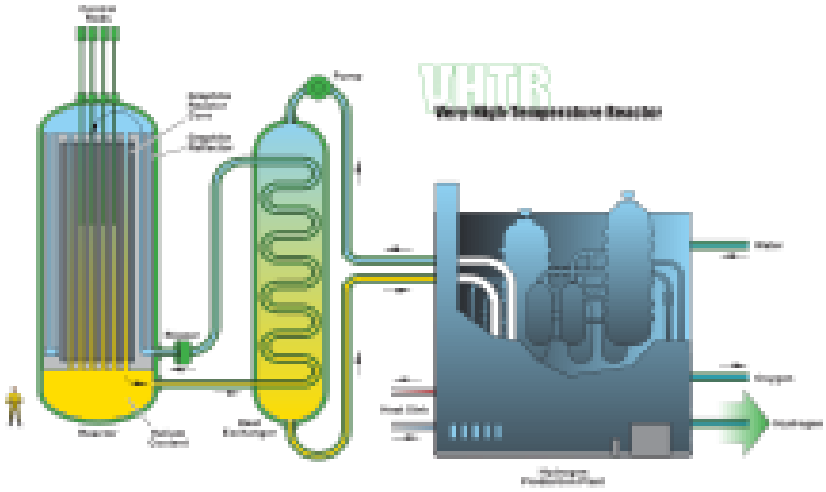

Figure 2.1: Schematic of Very-High-Temperature Reactor (VHTR) [24]

600 MWth VHTR dedicated to hydrogen production can yield over 2 million normal cubic meters per day. VHTR can generate electricity with high efficiency, ~50 % at 950 °C,

compared with 47 % at 850 °C. The generation of hydrogen, heat and power makes the VHTR an attractive heat source for large industrial complexes. It has excellent safety characteristics, the VHTR can be deployed in refineries and petrochemical industries to substitute large amounts of process heat at different temperatures, including hydrogen generation for upgrading heavy and sour crude oil.

2.1.2 Molten-salt reactor (MSR)

The (MSR) is a thermal-neutron-spectrum reactor, it uses a molten fluoride salt with dissolved uranium while the moderator is made of graphite. The inlet temperature of the coolant (e.g., fuel-salt mixture) is 565 °C while the outlet temperature reaches 700 °C. However, the outlet temperature of the fuel-salt mixture can even increase to 850 °C when co-generation of hydrogen is considered as an option. Compared with solid-fueled fast reactors, thermal-spectrum MSRs have lower fissile inventories, no radiation damage constraint on fuel burnup, no fabrication of fuel forms, no spent nuclear fuel assemblies, and a homogeneous isotopic composition of fuel in the reactor [24]. The MSR has a unique design features with high thermal efficiencies (between 45 and 50%) which make it very attractive option for future reactors.

2.1.3 Gas-Cooled Fast Reactor (GFR)

The (GFR) or High Temperature Reactor (HTR) is fast-neutron-spectrum reactor with a closed fuel cycle, which can also be for co-generation of hydrogen through thermochemical cycles or high-temperature electrolysis. The coolant is helium with inlet and outlet

temperatures of 490 and 850°C, respectively with direct Brayton helium-gas-turbine cycle. Indirect Rankine steam cycle or even indirect supercritical carbon-dioxide Brayton gas-turbine cycle are also considered. It combines the advantages of fast-spectrum systems [25] with those of high-temperature systems [26]. It combines the advantages of fast-spectrum systems for long-term sustainability of uranium resources and waste minimization (through fuel multiple reprocessing and fission of long-lived actinides), with those of high-temperature systems (high thermal cycle efficiency and industrial use of the generated heat, similar to VHTR). The advantages of the gas coolant are that it is chemically inert and single phase (eliminating boiling), and it has low neutron moderation. However, there are some technological challenges associated with the use of gas coolant without the graphite that is common in the HTR system. Its low thermal inertia leads to rapid heat-up of the core following loss of forced cooling. Since the power density is high in the GFR, the HTR-type "conduction cool-down" will not work for the removal of the decay heat, and other solutions must be considered. Also, the gas-coolant density is too low to achieve enough natural convection to cool the core, and the power requirements for the blower are important at low pressure. Lastly, additional consideration will need to be given to the effects of the fast neutron dose on the reactor pressure vessel in the absence of core moderation (the graphite moderator provides protection for HTR systems). The reference design for GFR is currently based around 2400 MWth, since the 600 MWth reactor presented in the original roadmap could not meet the break-even-breeding requirement. The 600 MWth is still considered as an option for a gas-cooled small modular reactor (SMR) that does not need to be a breakeven-breeder.

The direct power conversion cycle chosen as a reference in the original roadmap is no longer considered the only option. It was originally assumed that the HTR community would develop this technology in projects such as PBMR in South Africa and GT-MHR in the United States and Russia. Today in the United States, a commercial entity is developing the conceptual design of a small GFR and its associated technologies. Some near-term thermal HTR projects have moved away from the direct cycle concept, favouring the indirect cycle because of its lower technological risk and higher flexibility with respect to the choice of working fluid for the turbine. Therefore, the reference concept is an indirect cycle with helium on the primary circuit; a Brayton cycle on the secondary circuit and a steam cycle on the tertiary circuit (see Figure 2.2).

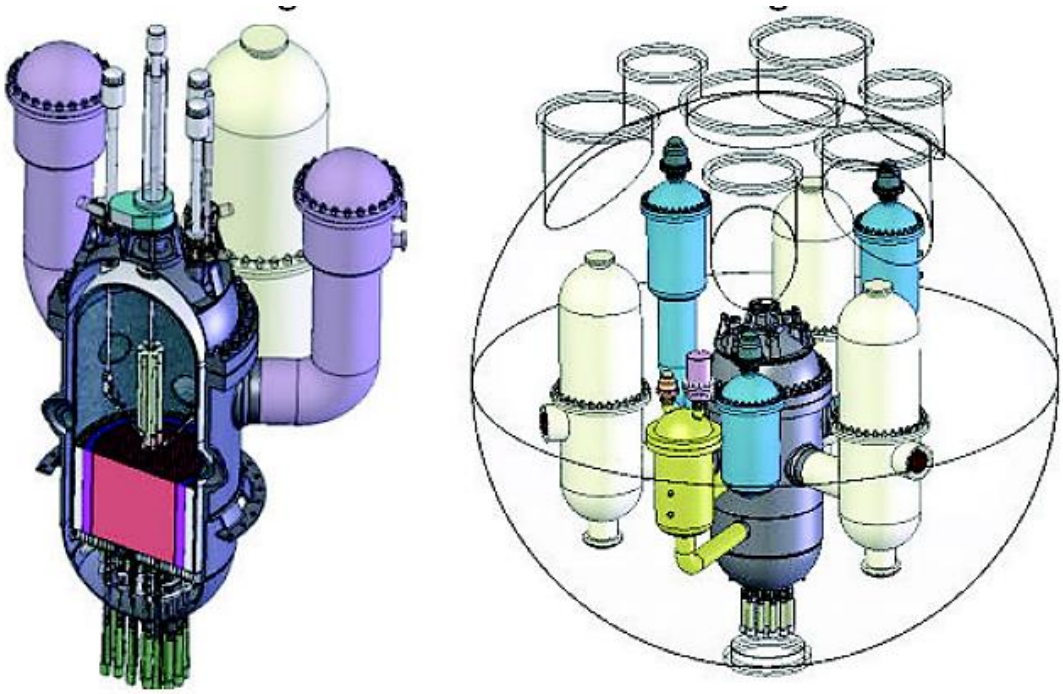

Figure 2.2: GFR reference design [24]

2.1.4 Lead-cooled fast reactor (LFR)

LFR is a fast-neutron-spectrum reactor with a closed fuel cycle, which uses lead or lead-bismuth as the reactor coolant. The outlet temperature of the coolant is about 550 °C (but can be as high as 800 °C) at atmospheric pressure. The primary choice of fuel is a nitride fuel. The supercritical carbon-dioxide Brayton gas-turbine cycle has been chosen as a primary choice for the power cycle in US and some other countries, while the supercritical-steam Rankine cycle is considered as the primary choice in Russia. The designs that are currently proposed as options are two pool-type reactors [24] - the small secure transportable autonomous reactor (SSTAR) and the European lead-cooled system (ELSY). LFRs are Pb or Pb-Bi-alloy-cooled reactors operating at atmospheric pressure and at high temperature because of the very high boiling point of the coolant (up to 1743°C). The core is characterized by a fast-neutron spectrum due to the scattering properties of lead. However, several drawbacks must be overcome, including the need for coolant chemical (oxygen) control for prevention of lead erosion-corrosion effects1 on structural steels at high temperatures and flow rates, and seismic/structural issues because of the weight of the coolant. The opacity of lead, in combination with its high melting temperature, presents challenges related to inspection and monitoring of reactor in-core components as well as fuel handling. In particular, in the case of reactor system cooled by pure Pb, the high melting temperature of lead (327°C) requires that the primary coolant system be maintained at temperatures adequately high to prevent the solidification of the lead coolant.

Although Pb-Bi reactors have been operated successfully in some of the Russian submarine programmes, this experience cannot be easily extrapolated to the LFR since the propulsion reactors were small, operated at low capacity factors, featured an epithermal (not fast)

neutron spectrum and operated at significantly lower temperatures2 than those anticipated in Gen-IV lead-cooled fast reactors. An additional issue with the lead-bismuth cooled reactors is related to the accumulation of volatile Polonium-210 which is a strong alpha emitter. In the Russian Federation, techniques to trap and remove ^{210}Po have been developed. The LFR systems identified by GIF include a wide range of plant ratings from the small to intermediate and large size. Important synergies exist among the different systems so that a co-ordination of the efforts carried out by participating countries will be one of the key points of LFR development. The options considered are: a small transportable system of 10 - 100 MWe size (Small Secure Transportable Autonomous Reactor or SSTAR – United States) that features a very long core life; a system of intermediate size (BREST 300 – Russia); and a larger system rated at about 600 MWe (European Lead Fast Reactor or ELFR – Euratom), intended for grid-connected power generation (see Figure 2.3).

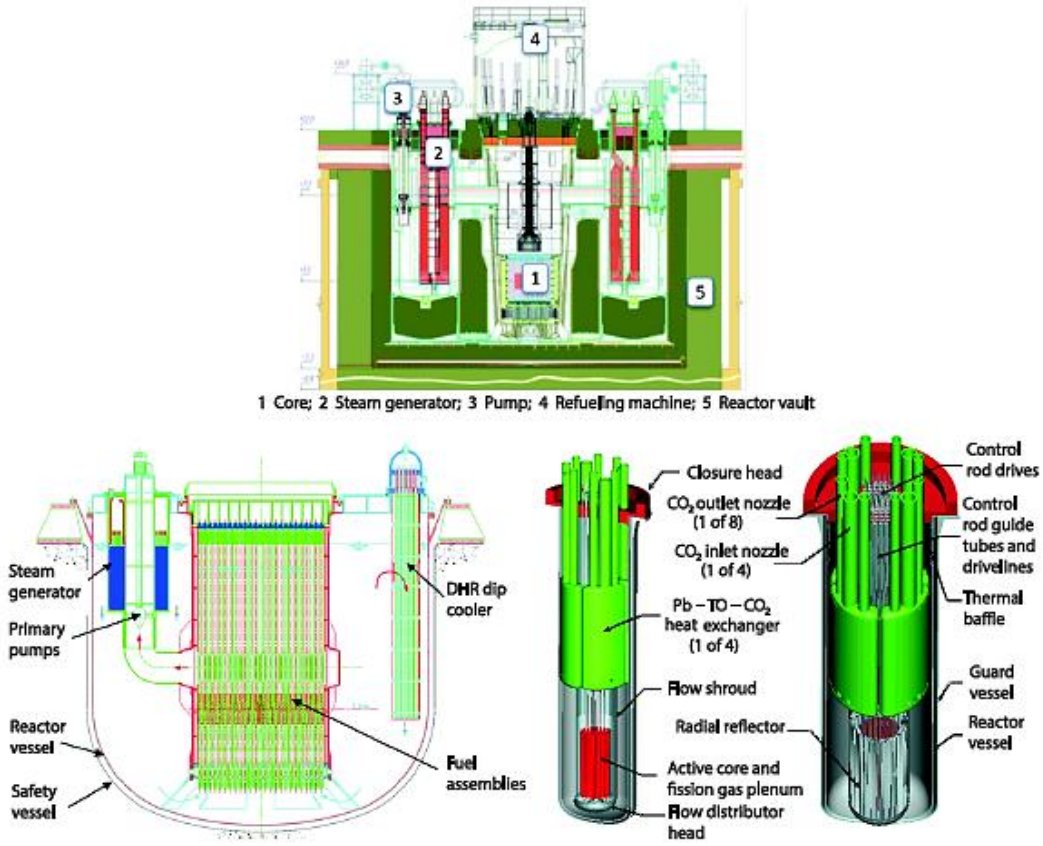

Figure 2.3: LFR reference designs: BREST-OD-300 (top), ELFR (left) and SSTAR (right) [24]

2.1.5 Sodium-Cooled Fast Reactor (SFR)

SFR is a fast-neutron-spectrum reactor that uses liquid sodium as the reactor coolant, It has high power density with low coolant volume fraction. SFR closed fuel cycle enables breeding of fissile fuel and facilitates the management of high-level radioactive wastes. The primary choices of fuel for SFR are oxide and metallic fuels with supercritical CO_2 as a working fluid for power conversion thermo system. Currently, SFR is the only one Generation IV power reactor implemented in the power industry. Russia and Japan are leaders within this area. India also has a Prototype Fast Breeder Reactor (PFBR) which is 500MWe pool type, sodium cooled nuclear reactor currently under advanced stage of

construction. Much of the basic technology for the SFR has been established in former fast reactor programs and is being confirmed by Phenix end-of-life tests in France, the lifetime extension of BN-600, the restart of Monju in Japan, startup of BN-800/BN-1200 in Russia, and the startup of the China Experimental Fast Reactor [24]. Water/steam and alternative fluids are considered for the power conversion system to achieve high performance in terms of thermal efficiency, safety and reliability.

2.2 History of Supercritical Water in Power Engineering Applications

Most expertise on Supercritical Water technology is due to experience gained during the building and operation of conventional fossil fuel power plant. SCWR research is thus not complete without mentioning of the history of the fossil-fired plants. This is a history that spans half a century of power engineering of coal burning SCW plants. The coal industry hopes to improve the durability of the high end SCW plants as the nuclear SCW research stems partially from the conventional plants [27].

2.2.1 History of Fossil-Fired Supercritical Power plants

A water drum boiler, in which the water is boiled in a drum and the steam is led straight to the turbine, and a once-through boiler which heats flowing water continuously are two varieties of boilers for fossil fired power plants. The latter boiler had been designed to accommodate the steam pressure to be raised as high as the boiler material allows, thus promoting the use of the supercritical regime of water. The once-through boiler design was patented during the 1920's, yet the boiler couldn't attain supercritical pressures in a

commercial operation until several decades later. Even though super criticality was achieved later, a variety of engineering challenges had to be overcome before the supercritical region became the industry standards. A list of SCW power plants problems encountered and their solutions can be found in literature, for example, in [27]. In the 1950's, the United States earliest commercial SCW plants were designed and commissioned with Philo 6 and Eddystone 1 being classical examples of first-generation coal-fired power plants. Eddystone 1 was designed to operate under steam conditions of 34.5 MPa and 650/565/565 °C. However, because of the mechanical and metallurgical challenges, Eddystone 1 was re-rated and operated below 32.4 MPa and 605 °C for most of its service life [28]. The challenges were due to high thermal stresses and fatigue cracking of the heavy section components. The challenges and the low availability of supercritical plants temporarily dampened the interest of the utility companies in supercritical (SC) plants. This resulted to most producers reverting to plants with sub-critical conditions of about 525 °C and 17 MPa. The mid 1960s saw one of the two early pioneers of coal-fired SCW power plants by the Soviet Union: The Russian SCW power plant was built and commissioned in 1966 with a rated power of 100 MWe, steam pressure of 30 MPa and temperature 650 °C. This was the year that propelled the super criticality application Era. Regardless the disappointing results of the first generation of the SCW plants during the 1950's and unfavourable economic conditions of the times, research and development of the technology continued. The energy crisis of the mid-70s and the subsequent increase in fuel prices was a blessing in disguise for the SCW because the crisis led to a renewed interest into more efficient power plants. With the increasing global awareness of the consequences of the pollution, along with the growing public distrust of

the nuclear option as of that time was an additional imperative for modernization of fossil fuel fired plants. Several coordinated research and development activities were formed [29] in Japan [29], the USA [30] and in Europe [31] in the early 1980's to see to the realization of the SCW fossil plants. Despite the research activities, the falling energy prices, low growth rates and the commitment of investment funds to environment protection measures prevented the construction of new power stations for a period during the 1980's. Generally one could conclude that the SCW technology lowered the fuel costs but also increased the capital cost for the power plant. This combined with the relative cheapness of the fuels has kept the interest in the high thermal efficiency technology at bay pre-90's everywhere but Japan Supercritical water boilers had proven themselves as a more reliable and established technology by the 90's. The efficiency of the new power plants has become more important than ever with the growing concerns of the global climate change. Adding to that, the successes achieved in materials research and boiler design, the capital costs and availability of the SCW plants were now comparable to those of the subcritical systems. According to some studies, low-end SCW coal-fired plants capital cost is about the same as high-end subcritical ones, with about two percentage increase in efficiency. Hence, it was not surprising that about 85 % of the new coal-fired power plants built in Organization for Economic Co-operation and Development (OECD) countries during 1997-2000 employed SCW technology. While the new SCW plants were dominantly supercritical, the installed capacity for OECD countries was dominated by subcritical steam technology due to historical reasons of lower capital costs and better operational availability and reliability. For SCW plants to be profitable, the plants do require higher level of expertise to manufacture, maintain and operate them than the subcritical units. The SCW plants have

larger portion of their operation costs due to interest from the initial capital cost than the more conventional power plants of equivalent MW_e, which in the final analysis pay more for the fuel. Thus, the operating reliability and capacity factor is more important to the economy of the SCW plants than to the conventional power plants, a situation similar to the comparison between nuclear power plants and fossil-fired ones. Given the considerations above, it may not be a surprise that in developing countries, such as Ghana and Nigeria, most of the new power plants are still subcritical [31]. Some studies projects that only about 5 % of the fossil power plants are to be built at the turn of the century in south-east Asia would have supercritical boilers [32].

2.3 Supercritical-water-cooled reactor (SCWR)

SCWRs are high temperature, high-pressure, light water reactors that operate above the thermodynamic critical point of water (374 °C, 22.1 MPa). The reactor core may have a thermal or a fast-neutron spectrum, depending on the core design. The concept may be based on current pressure-vessel or on pressure-tube reactors, and thus may use light water or heavy water as a moderator. Unlike current water-cooled reactors, the coolant will experience a significantly higher enthalpy rise in the core, which reduces the core mass flow for a given thermal power and increases the core outlet enthalpy to superheated conditions. For both pressure-vessel and pressure-tube designs, a once through steam cycle has been envisaged, omitting any coolant recirculation inside the reactor. As in a boiling water reactor, the superheated steam will be supplied directly to the high pressure steam turbine and the feed water from the steam cycle will be supplied back to the core. Thus the SCWR concepts combine the design and operation experience gained from hundreds of water-cooled reactors with the experience from hundreds of fossil-fired power plants

operated with supercritical water (SCW). In contrast to some of the other Generation IV nuclear systems, the SCWR can be developed step-by-step from current water-cooled reactors. Pre-conceptual core design studies for a core outlet temperature higher than 500 °C have been performed in Japan, assuming either a thermal or a fast neutron spectrum, as summarized by Oka et al. [33] Both options are based on a coolant heat-up in two steps with intermediate mixing below the core. Additional moderator for a thermal neutron spectrum is provided by feed water inside water rods. The fast-spectrum option uses zirconium-hydride (ZrH_2) layers to minimize hardening of the neutron spectrum in case of core voiding.

2.3.1 Major Advances in SCWR Development in the last Decade

A pre-conceptual design of safety systems for both options has been studied with transient analyses. A pre-conceptual plant design with 1700 MW net electric power based on a pressure vessel- type reactor has been studied by Yamada et al. [34] and has been assessed with respect to efficiency, safety and cost. The study confirms the target net efficiency of 44% and estimates a cost reduction potential of 30% compared with current pressurized water reactors. Safety features are expected to be similar to advanced boiling water reactors. A pre-conceptual design of a pressure-vessel-type reactor with a 500°C core outlet temperature and 1000 MW electric power has been developed in Europe as summarized by Schulenburg and Star flinger [35].

The core design is based on coolant heat up in three steps. Additional moderator for the thermal neutron spectrum is provided in water rods and in gaps between assembly boxes. The design of the nuclear island and balance of plant confirms results obtained in Japan, namely an efficiency improvement of up to 43.5% and a cost reduction potential of 20 to

30% compared with the latest boiling water reactors. Safety features, as defined by the stringent European Utility Requirements, are expected to be met. Canada is developing a pressure-tube-type SCWR concept with a 625°C core outlet temperature and a pressure of 25 MPa.[36] The concept is designed to generate 1200 MW electric power (a 300 MW concept is also being considered). It has a modular fuel channel configuration with separate coolant and moderator. A high-efficiency fuel channel is incorporated to house the fuel assembly. The heavy-water moderator is in direct contact with the pressure tube and is contained inside a low-pressure calandria vessel. In addition to providing moderation during normal operation, it is designed to remove decay heat from the high-efficiency fuel channel during long-term cooling, using a passive moderator cooling system. A mixture of thorium oxide and plutonium is introduced as the reference fuel, which aligns with the GIF position paper on thorium fuel. The safety system design of the Canadian SCWR is similar to that of the ESBWR. However, the introduction of the passive moderator cooling system coupled with the high-efficiency fuel channel could reduce significantly the core damage frequency during postulated severe accidents such as large-break loss-of-coolant or station black-out events. Pre-conceptual designs of three variants of pressure-vessel-type supercritical reactors with thermal, mixed and fast neutron spectrum have been developed in Russia [37, 38], which joined the SCWR System Arrangement in 2011. Outside of the GIF framework, two conceptual SCWR designs with thermal and mixed neutron spectrum cores have been established by research institutes in China under the framework of Chinese national R&D projects from 2007-2012, covering some basic research projects on materials and thermal hydraulics, core/fuel design, main system design (including the conventional part), safety systems design, reactor structure design and fuel assembly structure design.

The related feasibility studies have also been completed, and show that the design concept has promising prospects in terms of overall performance, integration of design, component structure feasibility and manufacturability. Prediction of heat transfer in supercritical water can be based on data from fossil fired power plants as discussed by Pioro et al. [39] Computational tools for more complex geometries like fuel assemblies are available but still need to be validated with bundle experiments. System codes for transient safety analyses have been upgraded to include SCW, such as depressurization transients to subcritical conditions. Flow stability in the core has been studied numerically. As in boiling water reactors, flow stability can be ensured using suitable inlet orifices in fuel assemblies.

A number of candidate cladding materials have been tested in capsules, autoclaves and recirculating loops up to 700°C at a pressure of 25 MPa. Stainless steels with more than 20% chromium are expected to have the required corrosion resistance up to a peak cladding temperature of 650°C. More work is needed to develop alloys suitable for use at the design peak cladding temperatures of 850°C for the Canadian SCWR concept. Further work is also needed to better identify the coolant conditions that lead to stress corrosion cracking. It has been shown that the creep resistance of existing alloys can be improved by adding small amounts of elements such as zirconium, as reported by Kaneda et al. [40] In the longer term, the experimental oxide dispersion-strengthened steel alloys offer an even higher potential, whereas nickel-based alloys that are being considered for use in ultra-supercritical fossil-fired plants are less favourable for use in SCWRs due to their high neutron absorption and associated swelling and embrittlement.

2.4 Heat Transfer Experiments with Supercritical Carbon dioxide

Experiment performed by Bringer and Smith [41] where Heat transfer coefficients were measured experimentally for carbon dioxide in turbulent flow in an 4.6 mm I.D. pipe. The pressure used was 8.27 MPa and the bulk temperature varied from 21°C to 49°C. In this critical region the coefficients between fluid and tube wall ranged from 43.2 W/ (m K) to 374.7 W/ (m K) and the Reynolds number interval of 30,000 to 300,000 showed that existing empirical and semi theoretical correlations were found inadequate in this region, where the thermal conductivity, viscosity, density, and specific heat are all varying rapidly and non-uniformly with temperature. Deissler proposed a method of integrating the heat and momentum transfer equations with different variable physical properties and it was applied to the experimental data and it was found that it fit well to the experiment. Extensive calculations were needed which was done with an Electro data digital computer. The application required extensive calculations, which were carried out with an Electro data digital computer. A simplified procedure was proposed for estimating heat transfer coefficients in the critical region by using a semi theoretical equation developed for zero heat flow. Simple rules were suggested for estimating the temperature at which to evaluate the physical properties when this equation is applied to the real case of finite heat transfer. The method worked well when compared with the computed heat transfer coefficients of Deissler for supercritical water but showed about 30% deviation when compared with the carbon dioxide results.

Wood and Smith [42] conducted an experiment on heat transfer in the critical region-temperature and velocity profile in turbulent flow, in the experiment it was observed that near the thermodynamic critical point an unusual phenomena of heat transfer occurred

between the solid surfaces and the fluids. In order to understand these phenomena better temperature, velocity profiles and local heat coefficient were measured for turbulent flow of carbon dioxide in a tube at 7.411 MPa. The results indicate a severe flattening of the radial temperature profiles, a maximum in the velocity profile between the wall and the tube axis, and a maximum in *h*' when the bulk fluid temperature passes through the transposed critical temperature. The results can be explained qualitatively by considering the variation with temperature of thermal conductivity near the tube wall and specific heat in the turbulent core.

Tanaka et al. [43] performed experiments on forced convection heat transfer under considerable high heat fluxes to supercritical carbon dioxide at 80 kg/cm^2 flowing upwards in a vertically placed circular tube of 6 mm ID, the tube surface roughness used for the test section was 0.2 μ and 1.4 μ and the surface roughness effect was investigated in the experiment tube. The heat transfer coefficient phenomena near the pseudo critical temperature and the wall temperature profiles were obtained.

Baskov et al. [44] carried out experiments to investigate the convection heat transfer of CO_2 at super-critical pressures in vertical multi-port mini-channels and small tubes for cooling conditions. The test section for small tube was a 150 mm-long vertical tube-in-tube counter-flow heat exchanger. The inner tube was smooth stainless steel 1Cr18N9T tube with inside and outside diameters of 2.00 mm and 3.14 mm. The test section for multi-port mini-channels was also counter-flow heat exchanger and the same flow direction of both cooling water and CO_2. The length, width and height of the multi-port mini-channel cooled directly by the water were 200.0 mm, 16.54 mm and 1.78 mm, respectively. The inner diameter of the mini-channels was 0.82 mm. The effects of cooling water mass flux, CO_2

mass flux, inlet temperature and pressure were investigated, respectively. In all cases with small tube concerned, wall temperatures were lower than pseudo critical temperature, while bulk temperatures are higher than pseudo critical temperature in the inlet and approached pseudo critical temperature in the outlet.

Effect of cooling: the effect of cooling on the heat transfer coefficient at temperature of CO_2 at 0 ^{0}C was 55 ^{0}C and pressure of 8.8 MPa, G = 0.53 kg/h along the tube. Here, pseudo critical temperature was 38.91 ^{o} C at a pressure of 8.8 MPa. As the same situation for the case with multi-port mini-channels, increasing cooling water mass flux caused a slight increase for the heat transfer coefficient. This can be explained when the cooling water mass flow rate increases, the heat transfer between the cooling water and the external surface of the tube wall is enhanced accordingly, which results in an increase of the heat flux from the CO_2 inside the tube to the tube wall, and the bulk temperature of CO_2 approaches more to the pseudo critical temperatures, as a result, the heat capacity of CO_2 bulk increases. It was observed that the mass flux of CO_2 has a great influence to the heat transfer coefficient, which increased significantly with the mass flow rate of CO_2. This is consistent with the results of regular fluids whose thermos-physical properties do not vary too much with temperature. When mass flow rate is doubled, the peak value of heat transfer coefficient increased by a factor 1.5. This is mainly due to the increase of turbulence kinetic energy with the increase of mass flow rate, which results in a strong mixing effect and acceleration of fluids, and therefore leads to an enhancement to the heat transfer between the fluid and solid tube wall. This is also the explanation for the increase of heat transfer coefficient with mass flow rate for regular fluids. For CO_2 at supercritical pressure, another reason is that the wall temperature increased with the increase of mass flow rate and

approaches to the pseudo critical temperature, as a result, the heat capacity of the CO_2 near the wall greatly increased, as well as the heat conductivity, which also results in an enhancement of heat transfer between the CO_2 and the solid tube wall.

Kim et al., [21] performed an experiment on the heat transfer characteristics of turbulent supercritical flow in vertical circular tubes. The fluid was carbon dioxide operating at a constant pressure of 8 MPa, the experiment was conducted with bulk temperature 15 to 32^{o}C, and the heat flux was from 3 to 180 kW/m^2 and mass flux from 209 to 1230 kg /m^{2}s. The Reynolds number were ranging from 3×10^4 to 1.4×10^5. The test region is composed of an entrance region of 600 mm long and heating region of 1200 mm long. The hydraulic diameter of tube is about 8 mm. the wall temperature distribution along the stream wise direction are compared at the same heat flux and mass flux conditions, local increase in wall temperature is observed due to heat deterioration, which is caused by the rapid thermal physical property variation of fluid near pseudo-critical temperature and by buoyancy near inner wall. Based on the results, the heat transfer deterioration criterion was determined in terms of heat flux and mass flux at a given inlet bulk temperature. An improved heat transfer correlation, which accommodates the effect of property variation and buoyancy is proposed by comparing it with previous ones existing in literature.

2.5 Heat Transfer Numerical Experiments with Supercritical Fluids

The heat transfer characteristics of supercritical carbon dioxide turbulent flow were investigated experimentally in a horizontal circular pipe with an inner diameter of 8.7 mm. Local convection coefficients and Nusselt numbers of the flow were obtained at different locations along the pipe with a constant heat flux ranging from 16 to 64 kW/m^2.

Experiments were performed for fluid mass flow rate ranging from 0.011 to 0.017 kg/s, an inlet fluid temperature ranging from 24 to 28 ^{o}C, and a flow pressure ranging from 7.5 to 9.0 MPa to investigate their effects on the convection heat transfer in the pipe. Both enhancement as well as deterioration in the heat transfer coefficient was observed for the flow conditions examined in this work. Experimental results were then compared with the widely used empirical correlation for pipe flow. Three commonly used buoyancy parameters were utilized to investigate their applicability in the present test conditions. Results indicate that all the parameters show a strong presence of buoyancy effects in the present test conditions. The trend and magnitude of these parameters, however, do not agree with the trend and magnitude of heat transfer enhancement and deterioration along the pipe [46].

Jang., Zhang and Shi [46] performed an experiment to provide a model for convection heat transfer of turbulent supercritical carbon dioxide flow in a vertical circular tube with a hydraulic diameter of 7.8 mm and inlet bulk temperature of 15 °C and a 8 MPa constant pressure by empirical results obtained by Kim et al. [46] and adaptive neuro-fuzzy inference system (ANFIS). At first, Nux was considered as a target parameter and qw, G, Bo* and x+ as input parameters. They randomly divided 123 empirical data into train and test sections in order to accomplish modeling. ANFIS network was instructed by 75% of the empirical data. Twenty-five percent of primary data which had been considered for testing the appropriateness of the modeling were entered into the ANFIS model. Results were compared by two statistical criterions (R2 and RMSE) with empirical ones. Considering the results, it was obvious that their proposed modeling by ANFIS was efficient and valid and it can be expanded for more general states.

Zang [47] performed an Experiment on Convection heat transfer of CO_2 at supercritical pressures in a 0.27 mm diameter, The vertical mini tube was investigated experimentally and numerically for upward and downward flows at relatively low inlet Reynolds numbers (2900 and 1900). The effects of inlet temperature, pressure, mass flow rate, heat flux, flow direction, buoyancy and flow acceleration on the convection heat transfer were investigated. For inlet Reynolds numbers less than 2.9×10^3, the local wall temperature varies non-linearly for both flow directions at high heat fluxes (113 kW/m^2). For the mini tube used in the current study, the buoyancy effect is normally low even when the heating is relatively strong, while the flow acceleration due to heating can strongly influence the turbulence and reduce the heat transfer for high heat fluxes. For relatively low Reynolds numbers (Rein $\leqslant 2.9 \times 10^3$) and the low heat flux (30.0 kW/m^2) the predicted values using the LB low Reynolds number correspond well with the measured data. However, for the high heat flux (113 kW/m^2), the predicted values do not correspond well with the measured data due to the influence of the flow acceleration on the turbulence.

2.6 Description of Kim et al. Test Facility

Figure 2.4 shows the test facility of the Kim et al., (2005) experiment. It was composed of a main loop for carbon dioxide flow and a secondary loop for cooling water. The working fluid is carbon-dioxide with 99.5% purity, which is pressurized to 8 MPa by using an air-driven booster pump and an accumulator. The working fluid is pumped round the main loop by a magnetic gear pump. The mass flow rate is controlled by the pump rpm and measured by a coriolis type flow meter. The carbon-dioxide was delivered to the electric preheater and/or to the bypass line when it is necessary to adjust the flow rate or to stabilize

the system. The electric preheater allows the fluid temperature to rise up automatically to a desired temperature at the inlet of the test section.

After being heated above the critical point in the test section, the fluid cools down to a temperature lower than the inlet temperature when it passes through two shell-and-tube type coolers. The chiller is used for supplying the city or chilled water to the two coolers with appropriate flow rate and temperature. The three tubes are made of Inconel 625. The test tubes are vertically mounted to generate aiding mixed convection flows. To provide uniform heat flux at the heating region of the test section, a DC heating method is adapted. The outer wall temperature variations along the test tubes are measured by chromium-aluminum sheath type thermocouples. The sheath type thermocouple is electrically insulated. Forty-one thermocouples are silver-soldered to the tube wall at every 30 mm from the starting point of the heating region. To confirm the uniformity in temperature variation along the circumference of the non-circular tubes, twenty thermocouples are additionally soldered at the corner at every 60 mm, and ten thermocouples at every 120 mm in the middle of the corner and the center of a side**.** The outer walls of the test tubes are thermally well insulated by ceramic-wool which is suitable for the high temperature insulation, and wrapped by ceramic-tape. To measure conduction to the non-heating region of the test tube, two thermocouples are attached at the upstream of the starting position of the heating region. Fluid temperature is measured at the inlet and outlet of the test section by using the same kind of thermocouples. The bulk fluid temperature at the outlet was measured in the outlet mixing chamber [21].

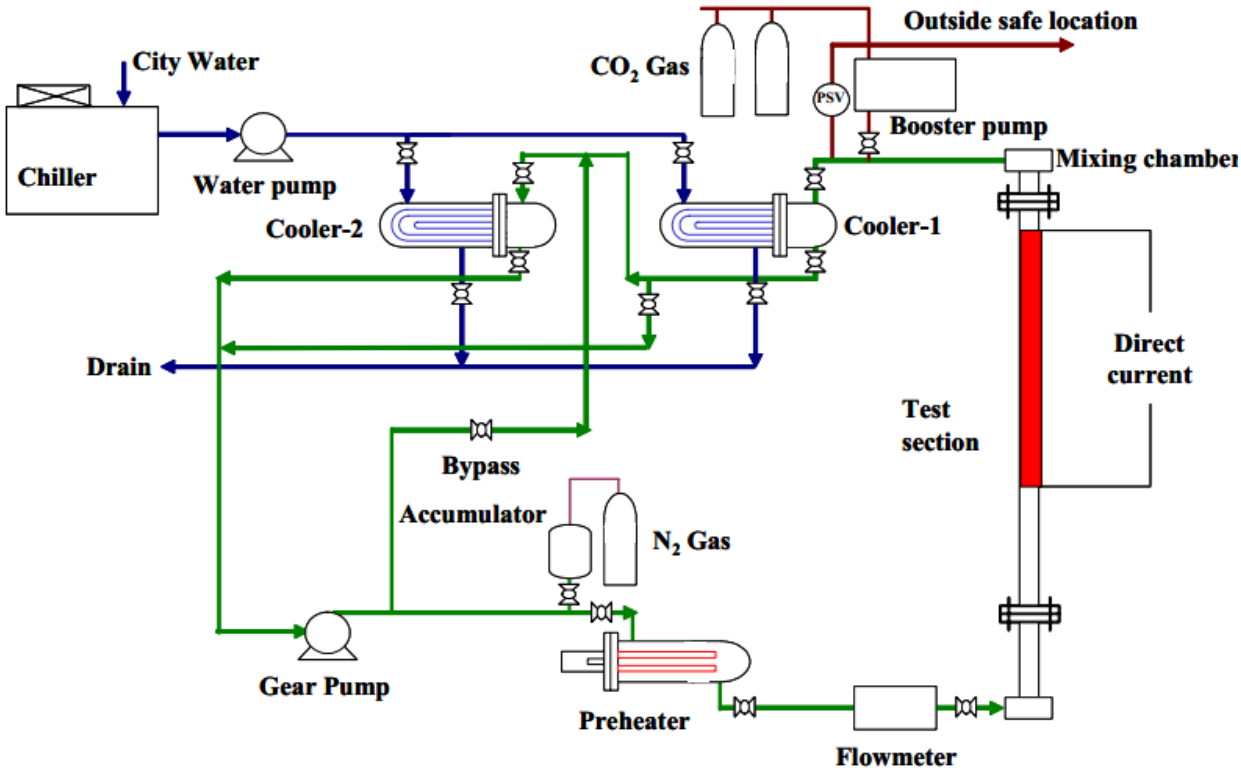

Figure 2.4: Schematic of Kim et al., facility [21]

CHAPTER THREE: METHODOLOGY

3.1 INTRODUCTION

The chapter presents the methodology used in the study of heat transfer mechanism with supercritical carbon dioxide as the working fluid. The experimental data of Kim et al. (2005) [21] is used as input data for both inlet and outlet boundary conditions for modelling in the STAR-CCM+ CFD code.

3.1.1 STAR-CCM+ CFD code

The STAR-CCM+ CFD code is a "general multipurpose" commercial software for computational fluid dynamics. A software STAR-design as geometric modeling and grid generation tool to create geometry and surface/volume mesh. The code is characterized by the full interactivity between user and solution: the integrated analysis and visualization tool provide a live feedback on the progress of the simulation. This allows changing parameters without stopping the solution, observing directly the consequent effects. STAR-CCM+ CFD code is an entire engineering process for solving problems involving flow heat transfer and stress. It provides a suite of integrated components that combine to produce a powerful package that can address a wide variety of modeling needs. It is specifically designed to handle large models quickly and efficiently using a unique client–server architecture that seamlessly meshes and simultaneously solves and post-processes over multiple computing resources without requiring additional effort from the user. The object-oriented nature of the code can be seen in the user interface. An object tree is provided for each live simulation, containing object representations of all the data associated with the

simulation. The objects presented on the simulation tree reside on the server, which can run as either a serial or a parallel process [48].

3.2 Governing Equations in the Axi-symmetric Flow STAR-CCM+

This thesis work concerns axisymmetric flows in circular tubes therefore a brief description of the governing equation in axisymmetric form is presented. The adopted notations in the equations are U represent the axial velocity and V represent the radial velocity; x represent the axial coordinate and r is the radial coordinate, ρ = density, P = pressure, μ = molecular viscosity, μ_e = effective dynamic viscosity and g = gravity.

The following represent the Reynolds- average equations.

3.2.1 Continuity equation

Fluid density is kept under the sign of differentiation to take into account its variation with pressure and temperature. In general, variation of fluid properties is accounted for by employing formulas in a separate module. All the flow variables appearing in the continuity equation and in all the other transport equations are considered as mean flow, time- (or ensemble-) averaged ones, according to the classical Reynolds-averaging approach.

$$\frac{\partial \rho}{\partial t} + \frac{\partial (\rho U)}{\partial x} + \frac{1}{r}\frac{\partial (\rho U)}{\partial r} = 0 \qquad (3.1)$$

Where U represent the axial velocity, ρ = density, r is the radial distance, x is the axial coordinates and t is the time.

In the momentum equations, the Reynolds stresses that result from the process of averaging of the instantaneous Navier-Stokes equations are modelled using the Boussinesq approximation, i.e., assuming that they are proportional to mean rates of deformation, with the turbulent viscosity μ_t as the proportionality factor.

3.2.2 U-momentum equation

The Reynolds stresses that result from the process of the instantaneous Navier-Stokes equations are modelled using Bassinesq approximation, i.e., assuming that they are proportional to mean rates of deformation, with turbulent viscosity μ_t as the proportionality factor, the equations 3.2 and 3.3 represent the turbulent momentum equations:

$$\frac{\partial\left(\rho U^2\right)}{\partial t}+\frac{\partial}{\partial x}\left(\rho U^2-\mu_e\frac{\partial U}{\partial x}\right)+\frac{1}{r}\frac{\partial}{\partial r}\left(\rho rUV-r\mu_e\frac{\partial U}{\partial r}\right)=-\frac{\partial p}{\partial r}+\rho g_x \tag{3.2}$$

Where μ_e is the effective dynamic, r is the radial distance, x is the axial coordinates, ρ is the density, U is the axial velocity, g_x is the gravity acceleration and V is the radial velocity.

3.2.3 V- Momentum equation is given by

$$\frac{\partial(\rho V)}{\partial t}+\frac{\partial}{\partial x}\left(\rho UV-\mu_e\frac{\partial V}{\partial x}\right)+\frac{1}{r}\frac{\partial}{\partial r}\left(\rho rV^2-r\mu_e\frac{\partial V}{\partial r}\right)=-\frac{\partial P}{\partial r}-2\frac{\mu_e V}{r^2}+\frac{\partial}{\partial x}\left(\mu_e\frac{\partial U}{\partial r}\right)+\frac{1}{r}\frac{\partial}{\partial r}r\mu_e\frac{\partial V}{\partial r}=0 \quad (3.3)$$

Where μ_e is the effective dynamic, r is the radial distance, x is the axial coordinates, ρ is the density, U is the axial velocity, and V is the radial velocity.

3.2.4 Energy Balance equation

Supercritical fluid properties vary dramatically as a function of temperature in the vicinity of the pseudo-critical temperature. These sharp variations can give rise to numerical instabilities that make convergence difficult.

$$\frac{\partial}{\partial x}(pUT)+\frac{1}{r}(prVT) \quad =\frac{\partial}{\partial x}\left[\left(\frac{\mu}{pr}+\frac{\mu_T}{\sigma_T}\right)\frac{\sigma T}{\partial x}\right]+$$

$$\frac{1}{r}\frac{\partial}{\partial r}\left[r\left(\frac{\mu}{pr}+\frac{\mu_T}{\sigma_T}\right)\frac{\partial T}{\partial r}\right] \quad (3.4)$$

Where U is the axial velocity, T is the temperature, μ is the molecular viscosity, r is the radial velocity, V is the radial velocity, x is the axial coordinate, and ρ is the density.

3.2.5 The κ-equation is given by

$$\frac{\partial(\rho\kappa)}{\partial t}+\frac{\partial}{\partial x}\left[\rho Uk-\left(\mu+\frac{\mu_t}{\sigma_\kappa}\right)\frac{\partial\kappa}{\partial x}\right]+\frac{1}{r}\frac{\partial}{\partial r}\left[\rho rVk-r\left(\mu+\frac{\mu_t}{\sigma_\kappa}\right)\frac{\partial\kappa}{\partial r}\right]= \quad (3.5)$$

$$P_\kappa+G_b-\rho\varepsilon$$

Where p_k is turbulent production term, x is the axial coordinate, μ is the molecular viscosity, G_b is the production term, Ɛ is the energy dissipation rate and ρ is the density.

The turbulent production term is calculated from:

$$p_\kappa = \mu\left[2\left(\frac{\partial U}{\partial x}\right)^2 + 2\left(\frac{\partial V}{\partial r}\right)^2 + 2\left(\frac{V}{\partial r}\right)^2 + \left(\frac{\partial U}{\partial r} + \frac{\partial V}{\partial x}\right)^2\right] \tag{3.6}$$

In the equation above, U is the axial velocity, V is the radial velocity, r is the radial distance, p_k is the turbulent production term, x is the axial coordinate, μ is the molecular viscosity, G_b is the production term, Ɛ is the energy dissipation rate and ρ is the density.

3.2.6 ε-equation is given by

The ε- equation is the energy dissipation rate and it is the most widely used in the simulations for supercritical water due to its good performance in the free-shear layer flows. However damping functions has to be employed in the modelling of STAR-CCM+ CFD code in order to avoid inherent singular defects in the near wall region.

$$\frac{\partial(\rho\varepsilon)}{\partial t} + \frac{\partial}{\partial x}\left[\rho U\varepsilon - \left(\mu + \frac{\mu_t}{\sigma_\varepsilon}\right)\frac{\partial\varepsilon}{\partial x}\right] + \frac{1}{r}\frac{\partial}{\partial r}\left(\rho r V\varepsilon - r\left(\mu + \frac{\mu_t}{\sigma_\varepsilon}\right)\frac{\partial\varepsilon}{\partial y}\right) = \tag{3.7}$$

$$\frac{\varepsilon}{\kappa}\left(f_1 c_\varepsilon I p_\kappa + c_3 G_b\right) - c_{\varepsilon 2} f_2 \rho\frac{\varepsilon^2}{\kappa} + \rho E$$

In the above equation, κ is the kinetic energy, ε is the energy dissipation rate, C is a constant, U is the velocity, μ is the molecular viscosity, r is the radial distance, V is the

radial velocity, x represent the axial coordinate, y is the radial coordinate, ρ is the density, f is damping function, T is the temperature, G_b is the production term, p_k is the turbulent production term and g is the gravitational acceleration, the subscript μ_e is the effective dynamic viscosity, and E is the enthalpy.

3.3 **Turbulence Modelling**

Computational modelling play a vital role in improving the understanding of the physics of convective heat transfer to fluids at supercritical pressures and assist with the development of correlation for engineering application. Raynolds-Averaged Navier-Stokes (RANS) approach which uses time average quantities and has the advantage to shorten computing time was used. The two types of turbulence models used in this work were the κ-ε and the κ-ω turbulence models. The Ɛ is the energy dissipation rate of k, while the ω is the specific heat dissipation rate of κ proposed by Wilcox in 1998 [58].

Six turbulence models were selected for this work to predict the heat transfer deterioration and enhancement, namely; κ-epsilon Abe-Kondoh-Nagano turbulence model (AKN), Elliptic blending turbulence model (EB), V2F κ-epsilon turbulence model, standard low-Reynolds turbulence model, κ-omega Shear-Stress Transport turbulence model (SST) and the Standard Wilcox κ-omega turbulence model: The basic transport equations of the six different turbulence models, their κ terms and ε terms as well as their constants are discussed below:

3.3.1 V2F κ-ε turbulence model

The V2F κ-ε turbulence model [50, 51, and 52] is known to capture near-wall turbulence effects, which is crucial for accurate prediction of heat transfer, skin friction and flow

separation. The model solves two additional turbulence quantities which are the normal stress function and the elliptic function in addition to κ and ε. The model is designed to handle wall effects in turbulent boundary layers and to accommodate non-local effects.

3.3.1.1 Turbulence Equation for V2F turbulence model

- The κ term for V2F model is given by

$$\int_v \left(\frac{\partial \rho k}{\partial t} - G_k - G_b + \rho(\varepsilon - \varepsilon_0)\gamma_M - S_k \right) dV = \int_A \left[\left(\mu + \frac{\mu_t}{\sigma_k} \right) \nabla k - \rho k (v - v_g) \right] da \quad (3.8)$$

- The ε term for the V2F model is given by

$$\int_v \frac{\partial \rho \varepsilon}{\partial t} - \left[\rho_{\varepsilon_1} \left(1 - a\sqrt{\frac{k}{\sigma^2}} \right) \frac{G_\kappa}{T} + \rho_{\varepsilon_2} (\varepsilon - \varepsilon_0) \frac{\varepsilon}{\kappa} - S_\varepsilon \right] dV = \int_A \left[\left(\mu + \frac{\mu_t}{\sigma_\varepsilon} \right) \nabla \varepsilon - \rho \varepsilon (v - v_g) da \right] \quad (3.9)$$

Where G_k = turbulent production term

γ_M = dilation dissipation

μ_t = turbulent viscosity

G_b = Production term

κ = kinetic energy

ε = dissipation rate

ρ= density

S_κ And S_ε are the user-specified source term, ε_0 is the ambient turbulence value in the source terms that counteract turbulence decay.

3.3.2 Standard low-Reynolds κ-ε turbulence model

This model has identical coefficients to the Standard κ-ε model, but provides more damping functions. These functions let it be applied in the viscous-affected regions near walls. It involves transport equation for turbulent kinetic energy and its dissipation rate Ɛ. The transport equation are suggested by Jones and Launder [53] with the coefficients suggested by [54]. Some additional terms have been added to the model in STAR-CCM+ to account for effects such as buoyancy and compressibility.

3.3.2.1 Turbulence Equation for standard low-Reynolds turbulence model

- The κ term for standard low-Reynolds is given by

$$\int_v \frac{\partial \rho k}{\partial t} - \left[G_k - G_b + \rho\left(\varepsilon - \varepsilon_0\right)\gamma_M - S_k\right]dV = \int_A \left[\left(\mu + \frac{\mu_t}{\mu_k}\right)\nabla k - \rho k\left(v - v_g\right)\right]da \tag{3.10}$$

Where S_k = source term, κ = turbulent kinetic energy, ρ= density, ν = velocity, ν_g = velocity of gas, ε = rate of dissipation of κ, ε_0 = ambient turbulence value, μ = viscosity, μ_t = turbulent viscosity, μ_k = turbulent kinetic energy, G_b = production term, G_k = kinetic energy production term, ∂a = change in area, ∂V = change in volume, f_1, f_2 and f_3 are damping functions.

- The ε term for standard low-Reynolds is given by

$$\int_v \frac{\partial \rho k}{\partial t} - \frac{1}{T}\left[C_{\varepsilon_1}\left(G_k - G_{n_1} - G - C_{\varepsilon_3}G_b\right) + C_{\varepsilon_2} - f_2\rho\left(\varepsilon - \varepsilon_0\right) - pY - S_\varepsilon\right]dV = \int_A\left[\left(\mu + \frac{\mu_t}{\sigma_k}\right)\nabla\rho\varepsilon - \rho\left(\nu - \nu_g\right)\right]da \quad (3.11)$$

Where S_k and S_ε are the user-specified source term, ε_0 is the ambient turbulence value in the source term that counteract turbulence decay and G' is an additional term.

$$G = Df_2\left(G_k + 2\mu\frac{k}{y^2}\exp\left(-E\,\mathrm{Re}_y^2\right)\right) \quad f_2\text{=1-Cexp} \quad \mathrm{Re}_T^2 \quad \mathrm{Re}_y = \sqrt{\frac{ky}{\nu}} \quad \mathrm{Re}_t = \frac{k^2}{\varepsilon\nu}$$

3.3.3 Abe-Kondoh-Nagano (AKN) κ-ε Turbulence Model

The AKN model [55] work well for wide range of complex flows. It has different coefficients than standard low-Reynolds model and uses different damping functions than

standard low-Reynolds number. This model is a good choice for applications such as compact heat exchangers, where the Reynolds numbers are low but the flow is relatively complex.

3.3.3.1 Turbulence Equation for AKN Turbulence Model

- The κ term for AKN is given by

$$\int_v \left(\frac{\partial \rho k}{\partial t} - G_k - G_b + \rho(\varepsilon - \varepsilon_0)\gamma_M - S_k \right) dV = \int_A \left[\left(\mu + \frac{\mu_t}{\sigma_k} \right) \nabla k - \rho k (v - v_g) \right] da \tag{3.12}$$

- The ε term for AKN is given by

$$\int_v \left[\frac{\partial \rho \varepsilon}{\partial t} - \frac{1}{T}\frac{\varepsilon}{k}\left(C_{\varepsilon_1}(G_k - C_\varepsilon G_b) + C_{\varepsilon_2} - \rho(\varepsilon - \varepsilon_0) - PY_y - S_\varepsilon \right) \right] dV = \int_A \left[\left(\mu + \frac{\mu_t}{\sigma_k} \right) \nabla k - \rho k (v - v_g) \right] da \tag{3.13}$$

Where S_k and S_ε are user-specified source term , ε_0 is the ambient turbulence value in source terms that counteract turbulence decay and f_2 is a damping function and is given by

$$F_2 = \left[1 - \exp\left(\frac{-\mathrm{Re}_\varepsilon}{3.1} \right) \right]^2 \left\{ 1 - 0.3 \exp\left[-\left(\frac{\mathrm{Re}_t}{6.5} \right)^2 \right] \right\} \quad \mathrm{Re} = \frac{(v\varepsilon)^{1/4} y}{v} \tag{3.14}$$

3.3.4 Elliptic Blending (EB) κ-ε Turbulence Model

The concept of the EB model was proposed by Durbin [56] for Reynolds stress models. The initial model required the solution of six additional transport equation, but the number was later reduced by single additional equation. The model was later simplified by Manceau and Hanjalic [57]. The elliptic relaxation model led to the development of some two eddy-viscosity models, starting with the V2F.

These are some important modification that makes it truly robust;

- An improvement of the existing realizable κ-ε model in terms of accuracy, especially in the near-wall region.
- An improvement in terms of stability over the SST κ-ω model.

3.3.4.1 Turbulence Equation for EB turbulence model

The κ term for EB model is given by

$$\frac{dPk}{dt} = P_k + P_b - P\varepsilon + \frac{\partial}{\partial xj}\left[\left(\frac{\mu}{2} + \frac{\mu_t}{\sigma_k}\right)\frac{\partial k}{\partial xj}\right] \tag{3.15}$$

The ε term for EB model is given by

$$\frac{dp\varepsilon}{dt} = \frac{1}{T}\left(c_{\varepsilon 1}P_k + c_{\varepsilon 1}c_{\varepsilon 3}P_b - PE - c_{\varepsilon 3}\varepsilon\right) + \frac{\partial}{\partial xj}\left[\left(\frac{\mu}{2} + \frac{\mu_t}{\sigma_\varphi}\right)\frac{\partial \varphi}{\partial xj}\right] \tag{3.16}$$

3.3.5 Shear-Stress Transport (SST) κ-ω Turbulence Model

This model was developed by Menter [58] in 1994, the Shear Stress Transport κ-Omega model takes advantage of accurate formulation of the κ-ω model in the near-wall region with the free-stream independence of the κ-ε model in the far field. It does so by multiplying the final additional term, obtained from deriving the κ-ε model, by a blending function. Close to wall the damped cross-diffusion derivative term is zero (leading to the standard ω equation), whereas remote from wall the blending function is unity (corresponding to the standard ε equation).

3.3.5.1 Turbulence Equation for SST Turbulence Model

- The κ term in the SST model is given by

$$\int_v \left[\frac{\partial \rho k}{\partial t} - Y_{eff} G_k + YP\beta^* f_{\beta*}\left(\omega k + \omega_0 k_0\right) - S_k - \rho\omega \right] dV = \int_A \left[\left(\mu + \frac{\mu_t}{\sigma_k} \right) - \rho k \left(v - v_g \right) \right] da \tag{3.17}$$

- The κ term for SST model is given by

$$\int_v \left[\frac{\partial \rho \omega}{\partial t} - G_w + \rho B F_B \left(w^2 + w_0{}^2 \right) - D_w - S_w \right] dV = \int_A \left[\left(\mu + \sigma_w \mu_t \right) - \rho\omega \left(v - v_g \right) \right] da \tag{3.18}$$

where S_k and S_ω are the user-specified source term K_0 and ω_0 are the ambient turbulence source terms that counteract turbulence decay γ_{eff} is the intimacy provided by the Gamma Re Theta Transitional model $\gamma^{'}$ = min [max(γ_{eff} ,0.1), 1]

D_w = cross-derivation term

3.3.6 Standard Wilcox Turbulence Model

Wilcox revised his original model in 1998 and then in 2006 [58]. These version includes

- ❖ A revised set of model coefficient
- ❖ Two corrections to account for sensitivity to free-stream / inlet conditions both were based on products of ∇_k and ∇_w. The first model introduced in 1998 is a modification of the turbulent kinetic energy equation. The most recent revision [58] is the introduction of cross-diffusion term that is similar to that used in the SST κ-ω model.
- ❖ A correction to improve the free shear-stress-flow spreading rates of the model
- ❖ A compressibility correction
- ❖ Low-Reynolds number correction that allow the κ-ω to be better applied in prediction of low-Reynolds numbers or transitional flows.

3.3.6.1 Turbulence Equation in the Standard Wilcox Turbulence Model

- The κ term for standard Wilcox model is given by

$$\int_v \left[\frac{\partial \rho k}{\partial t} - G_k + \rho \beta^* f_{\beta^*}\left(\omega k + \omega_0 k_0\right) - S_k\right] dV = \int_A \left[\left(\mu + \sigma_k \mu_t\right)\nabla k - \rho k\left(v - v_g\right)\right] da \tag{3.19}$$

- The ε term for standard Wilcox model is given by

$$\int_v \left[\frac{\partial \rho \omega}{\partial t} - G_{w\_PB} f_B\left(\omega^2 + \omega_0{}^2\right) - D_w - S_w\right] dV = \int_A \left[\left(\mu + \sigma_w \mu_t\right)\nabla \omega - \rho \omega\left(v - v_g\right)\right] da \tag{3.20}$$

3.4 Models Constants

Table 3.1: Turbulence model constants for κ-ε models

model	C_{μ}	$C_{\varepsilon 1}$	$C_{\varepsilon 2}$	σ_k	σ_{ε}
AKN	0.09	1.5	1.9	1.4	1.4
V2F	0.09	1.4	1.9	1.0	1.3
Standard low-Re	0.09	1.44	1.92	1.0	1.3
EB	0.09	1.4	1.9	1.0	1.4

3.5 Turbulence model constants for SST κ-ω

The model coefficients are calculated from the blending function f_1 such that each coefficient φ is given by $\varphi = f_1 \phi_1 + (1+ f_1)\phi_2$

The coefficients for set 1 are given as

$\beta_1 = 0.0750,\ \sigma_{k1} = 0.85, \sigma_{\omega 1},\ \kappa = 0.41$

$$\Upsilon_1 = \frac{\beta_1}{\beta^*} - \sigma_{\omega 1}\frac{k^2}{\sqrt{\beta^*}}$$

The coefficients of set 2 (φ_2) are $\beta_2 = 0.0828,\ \sigma_{k2} = 1.0,\ \sigma_{\omega 2} = 0.856,\ \kappa = 0.41$

$$\Upsilon_2 = \frac{\beta_2}{\beta^*} - \sigma_{\omega 2}\frac{k^2}{\sqrt{\beta^*}}$$

Both set 1 and set 2 gives $\beta^* = 0.09,\ \alpha^* = 1$

3.6 Standard Wilcox omega Model Constants

$\beta^* = 0.09,\ \beta = \frac{9}{125},\ \alpha = \frac{13}{25},\ \alpha^* = 1,\ \sigma_k = 0.5,\ \sigma_\omega = 0.$

3.7 Heat transfer Coefficients

The Heat transfer coefficient must be defined using correlation, it is often given in terms of the particle Nusselt number.

$$Nu_p \equiv \frac{hD_p}{k}$$

Where k= the thermal conductivity of continuous phase, h= enthalpy, D_p= hydraulic diameter and Nu_p= Nusselt number

Ranz correlation method is used in STAR-CCM+ CFD code for defining heat transfer coefficient.

The Ranz Marshall correlation [59] is suitable for spherical particles up to $\mathrm{Re}_p \sim 500$. It is formulated as $Nu_p = 2\left(1 + 0.3\mathrm{Re}_p^{\frac{1}{2}}\mathrm{Pr}^{\frac{1}{3}}\right)$ (3.14)

Where Nu_p= Nusselt number, Re_p= Reynolds number and Pr = Prandtl number

3.8 Boundary Conditions

The boundary conditions that were used in the simulation of the different turbulence models are show in tables 3.1 and 3.2 below.

Table 3.2: control parameters

Inlet fluid temperature	15 ^{o}C
Pressure	8 MPa
Mass flux	314 kg/m^{2}s
Heat fluxes	20 kW/m^2, 23 kW/m^2, 30 kW/m^2 and 40 kW/m^2

3.8.1 Tube dimensions

Table 3.3: experimental dimensions

Hydraulic diameter	7.8 mm
Wall thickness	1.0 mm
Heated length	1.2 m
Entrance length	0.8 m

3.8.2 Experimental data

The experimental data of Kim et al. [21] was used as the input data for both inlet and outlet boundary conditions for modelling in STAR-CCM+ code. Circular tube cross section of hydraulic diameter of 7.8 mm. The hydraulic diameter is made of Inconel-625 with a thickness of 1.0 mm and an axial distance of 2.0 m. The CO_2 at a constant pressure flowed upward in the test section in the uniformly heated vertical sections under conditions of buoyancy aided mixed convection. The heated section of the channels is 1.2 m long and was preceded by an adiabatic stabilization section of 0.8 m long. On the outer wall of the section, a DC heating system was imposed with 41 chromium-aluminum sheath type thermocouples, silver soldered on the outer section surface every 30 mm from the beginning of the heated section. The outer wall of the test section was thermally insulated by ceramic wool and wrapped by ceramic tapes. In-depth details about the experiment can be found in Kim et al. [21]. The control parameters in the experiments were inlet pressure 8 MPa, inlet fluid temperature 15^{o}C, wall heat fluxes 20 kW/m^2, 23kW/m^2, 30kW/m^2 and 40 kW /m^2 with mass flux 314 kg/m^{2}s are the experimental conditions that were considered in this work.

3.9 Geometry

A parallepipedal structure was generated and it was projected on to one face to become a rectangle.

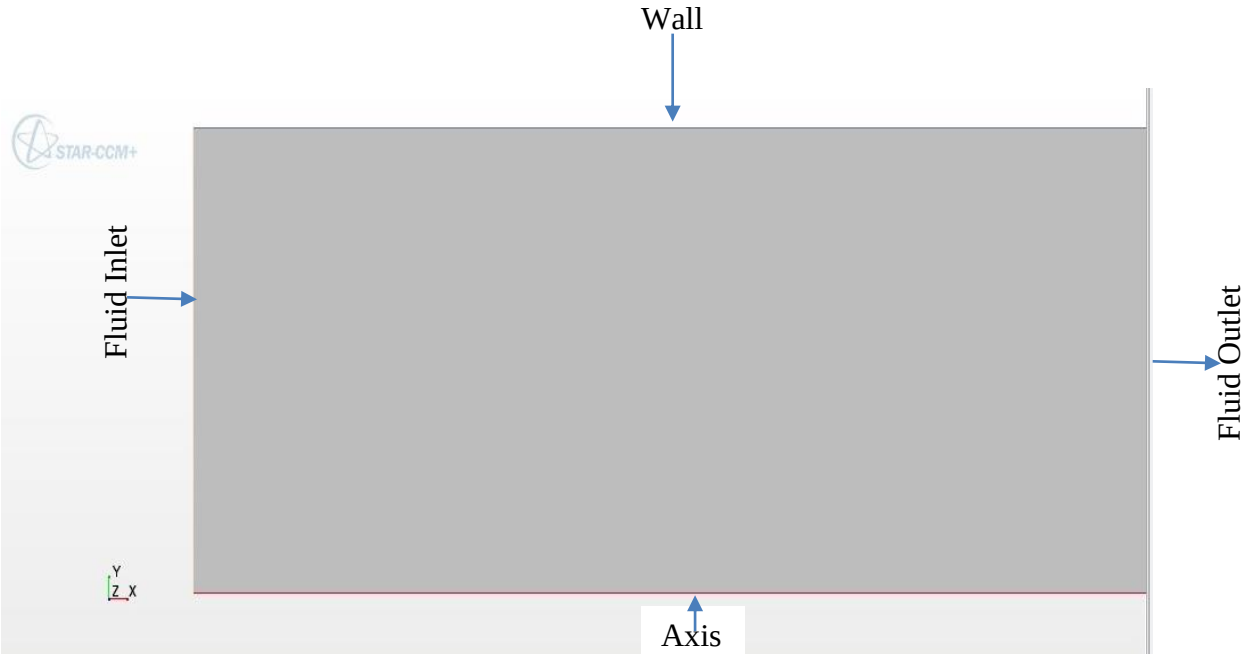

Figure 3.1: Geometry for thesis work

In the figure 3.1 the parallelpipedal structure was first projected onto one of its face to become a rectangle. A circular pipe with length 2 m and heated length of 0.8 m and the diameter of the pipe is 7.8 mm. The heated portion of the pipe was neglected at the level of generating the geometry but was only dealt with at the level of imposing boundary conditions. After imposing the boundary conditions, the parallelpipedal was generated with a length and height of 3.9 mm.

3.9.1 Meshing

The STAR-CCM+ contains tools which can be used to generate mesh starting from the surface. The volume mesh contain either trimmed, polyhedral or tetrahedral type of cell for each region determined via the selection of mesh models. In this research trimmed meshes were selected. “Trimmed” cell meshes provide a robust and efficient method of producing high quality grid for both simple and complex mesh generation. In trimmed cells, automatic feature refinement is included to further optimize the cell distribution. The adopted 2D

axisymmetric mesh parameters are shown in figure 3.4. Firstly a 3D mesh was generated and then converting it to 2D within the STAR-CCM+ environment. Size scaling feature available in the code were used in order to obtain a full 2 m tube fluid region containing 200 uniform axial nodes.

Table 3.4: parameters for meshing

Parameter	Value
base size	0.1mm
prism layer stretching	1.0
prism layer thickness	1.1mm
number of prism layer	60
surface growth rate	1.3
surface proximity (points in gaps)	2.0
relative minimum size	0.025mm
relative target size	0.1mm

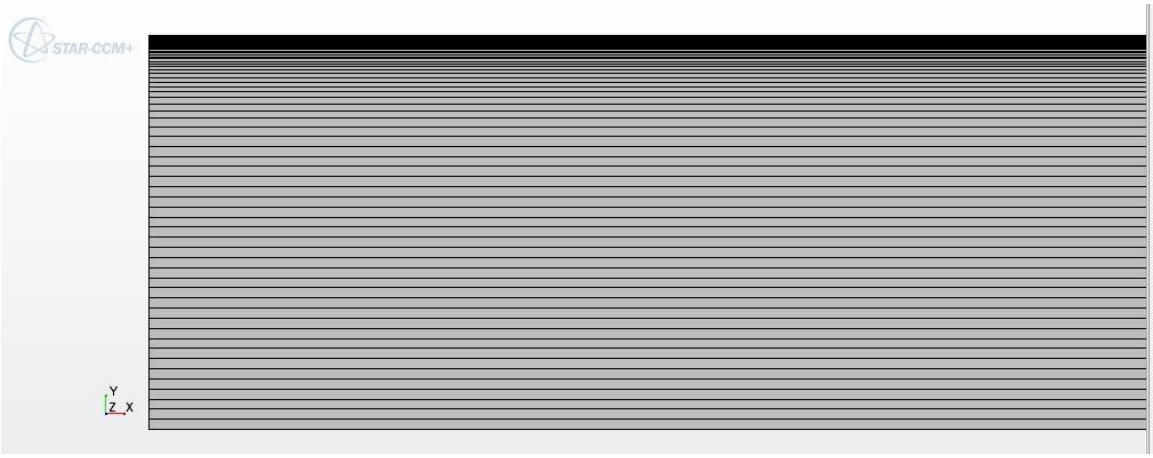

Figure 3.2: Grid adopted 2D mesh for the circular tube

3.10 Physics Models

The physics models define the primary variables of the simulation, including pressure, temperature and velocity and the mathematical formulation. In this research the flow is turbulent and compressive. The segregated flow model together with the default k-epsilon turbulent model were used. In STAR-CCM+ the physics models are defined on a physics continuum. The following selection were required for the simulation as shown in the table 3.5.

Table 3.5: Fluid physics and model specification

Models	Model Specification
Space model	2-D
Time model	Steady state
Material medium	Single phase carbon dioxide
Equation of state	Polynomial density
Flow model	Segregated flow
Energy model	Segregated fluid temperature
Viscous regime	Turbulent
Turbulent model	κ-epsilon
κ-epsilon model	Realizable two layer
Wall function	Low y+ wall treatment

3.11 Simulation

The models described in 3.3.1 to 3.3.6 above was run with a constant mass flow rate of 314 kg/m^{2}s, inlet fluid temperature of 15 ^{O}C, pressure of 8 MPa and heat fluxes of 20, 23,

30 and 40 kW/m^2. The simulation was run in a steady-state condition with segregated flow model and κ-ε turbulent model as default, the material medium was single phase carbon dioxide (gas) with segregated fluid temperature. The low y+ wall treatment was chosen because it is suitable only for low Reynolds turbulence models in which it is assumed that the viscous sub-layer is properly resolved. The simulation was run for 20,000 iteration as the maximum step or stopping criteria, it was observed in the residual as it converged to a reasonable level.

CHAPTER FOUR: RESULTS AND DISCUSSION

This chapter presents the simulation results and discussions on heat transfer in a circular tube of 7.8 mm hydraulic diameter and the six (6) turbulence models namely; AKN, EB, V2F, Standard Low-Reynolds, SST and standard Wilcox and compared with the experimental data of Kim et al. [21].

4.1 Turbulence Models Comparison of Wall Temperature

The obtained results of wall temperature distribution along the axial distance are discussed in the following sub-section with a constant mass flow rate of 314 kg/m^2.s and variable heat fluxes of 20 kW/m^2, 23 kW/m^2, 30 kW/m^2 and 40 kW/m^2 as seen in the simulation.

4.1.1 Turbulence Models comparison at 20 kW/m^2

Figure 4.1 shows a comparison of the wall temperature distribution predicted by six low Reynolds turbulence models namely; κ-ε AKN, EB, standard low-Reynolds and k-ω SST and standard Wilcox with heat flux of 20 kW/m^2 and mass flux of 314 kg/m^{2}s. The computational study was compared with Kim et al. [21] experimental data.

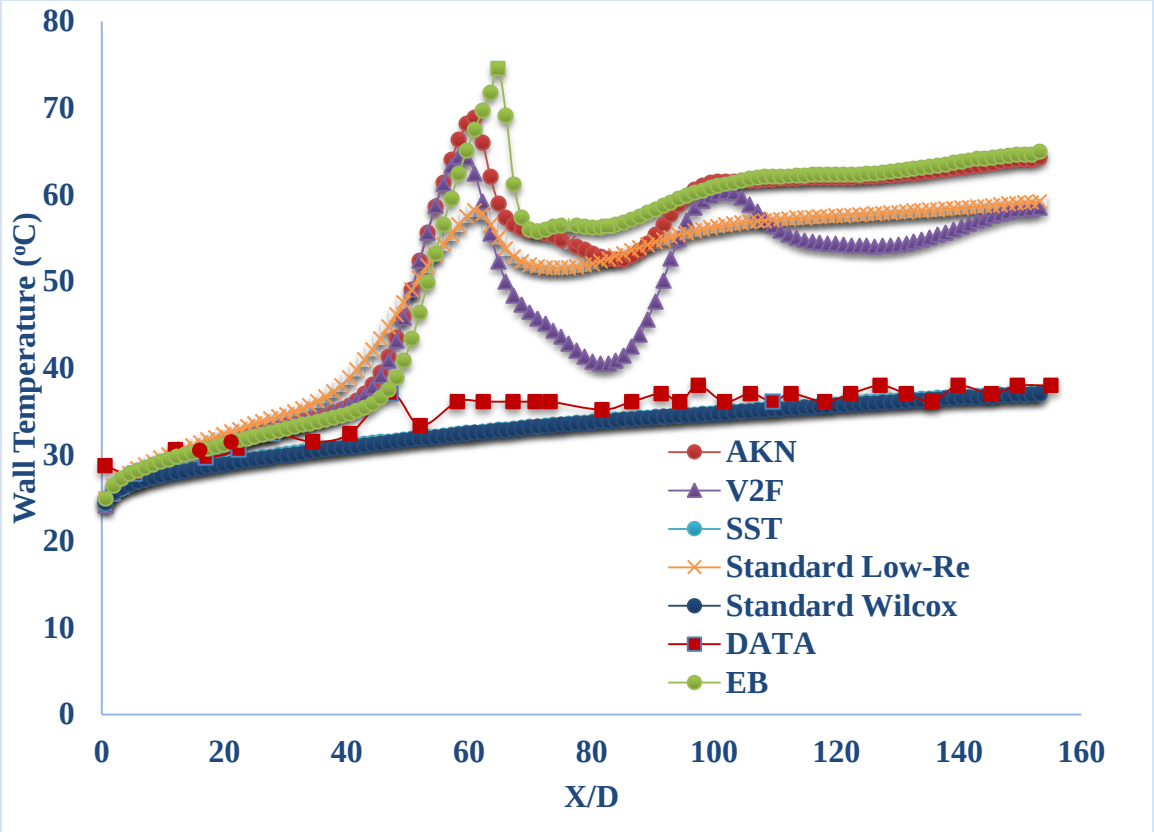

Figure 4.1: Turbulence Models comparison of wall temperature at heat flux of 20 kW/m^2

From the Figure 4.1, the experimental data did not show any major deterioration or enhancement. In this case, the wall temperature was seen to be relatively smooth even though uneven. From the six (6) low Reynolds turbulence employed in this research, the k-ω turbulence models (SST and Standard Wilcox) was able to qualitatively predict the wall temperature as in the experiment but not quantitatively. The rest of the models predicted an enhancement and deterioration which is not present in the experimental data. This might be due to the fact that they over predict and calculate the frictional and buoyancy forces within the system. This over prediction can also be attributed to the Nusselts correlation used in the development of the STAR-CCM+ code (Rans-Marshall correlation). It must be stated that up till date researchers are conducting various research to come up

with correlations that better suit super critical water experiment since most correlations are entirely based on sub-critical flows. It can the seen from the graph that the AKN, V2F and Standard Low-Reynolds models predicted heat transfer deterioration around X/D = 60 but the V2F model predicted two peaks at approximately X/D = 60 and 120. The peaks might be due to the over prediction of frictional and buoyancy forces. Among all the models used, the EB predicted the highest deterioration which was not even present in the experimental data.

4.1.2 Turbulence Models comparison at 23 kW/m^2

Figure 4.2 displays the comparison of wall temperature predicted by six low Reynolds models at a heat flux of 23 kW/m^2 and mass flux of 314 kg/m^{2}s and compared with the experimental data of Kim et al. [21].

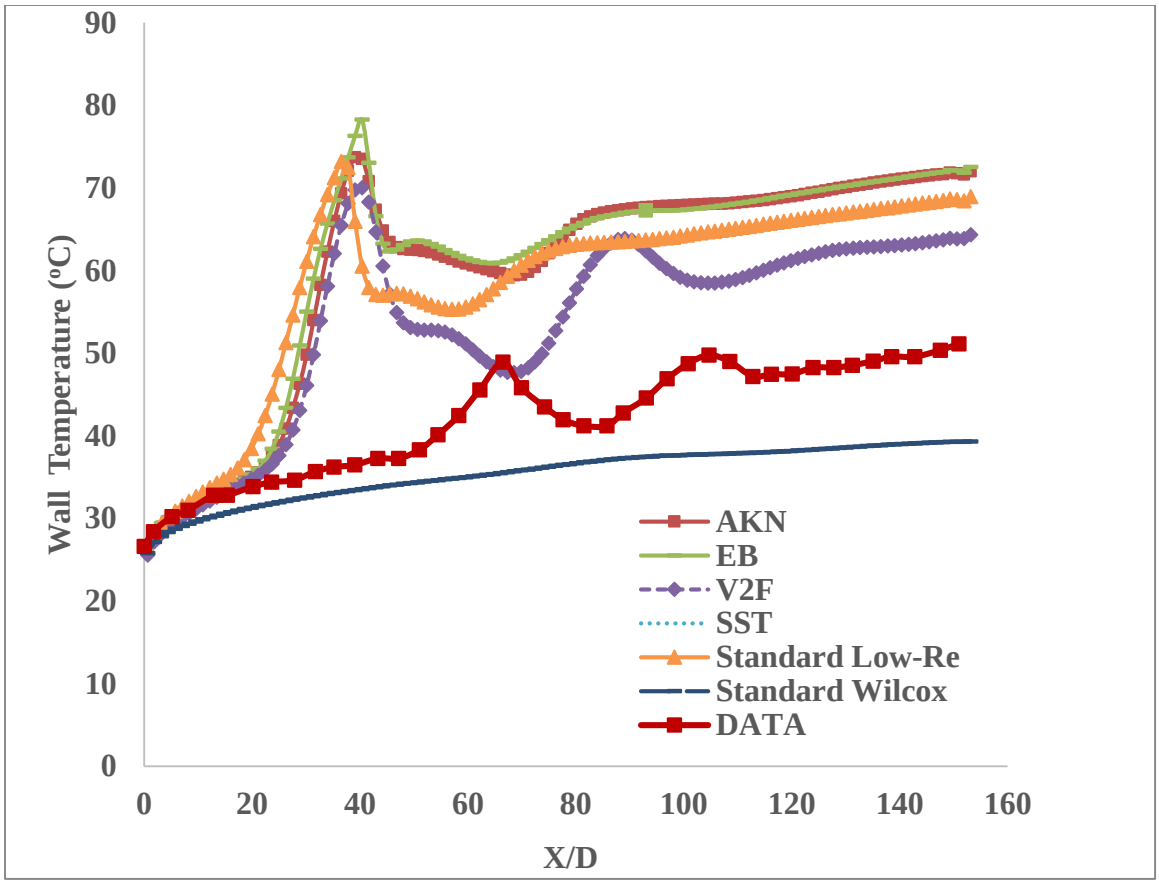

Figure 4.2: Turbulence Models comparison of wall temperature at heat flux of 23 kW/m^2

From the Figure 4.2, the experimental data shows that the temperature rose steadily from the point X/D = 0 and then exhibited a characteristics of heat transfer deterioration at about X/D = 66 and a second peak at about X/D = 104. The appearance of the experimental data curve was simulated with the κ-ε models; AKN, EB and standard low-Reynolds and the V2F turbulence models. It is seen that the AKN, EB and Standard Low-Reynolds models were able to predict the first peak at about at X/D = 40 even though it was over predicted in terms of the wall temperature. The V2F turbulence model was the only model that was able to capture the two peaks shown by the experimental data. Even though it was able to predict the two peaks, it also over predicted these peaks in terms of temperature at about

X/D = 40 and 86. The reason for the over prediction of these two peaks can again be attributed to the code's ability to perfectly predict the friction factors in the region of super criticality. From the simulations, the κ-ω (SST and standard Wilcox) models showed no presence of any deterioration.

4.1.3 Turbulence Models comparison at 30 kW/m^2

Figure 4.3 shows the comparison of wall temperature distribution which was predicted by AKN, EB, Standard Low-Re, V2F, SST and Standard Wilcox models with heat flux of 30 kW/m^2 and mass flux of 314 kg/m^{2}s. The simulation results was compared with Kim et al. [21] experimental data which predicted the heat transfer deterioration at around X/D = 30. The Figure show that all the κ-ε models were able to predict the heat transfer deterioration at around X/D = 30 but showed an over estimation of the wall temperature.

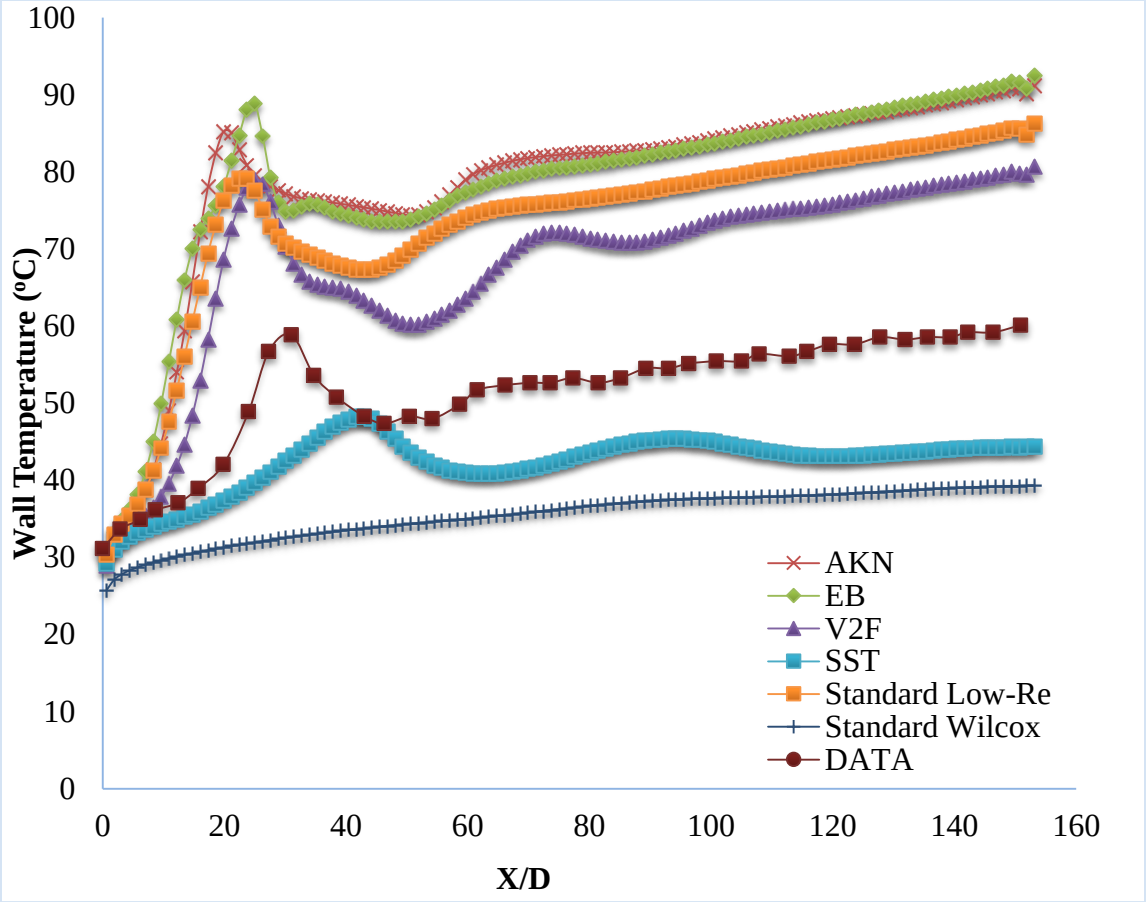

Figure 4.3: Turbulence Models comparison of wall temperature at heat flux of 30 kW/m^2

The κ-ω SST turbulence model in this case was able to predict the deterioration observed in the Kim's experiment with around X/D = 42 but under predicted the wall temperature. The κ-ω Standard Wilcox turbulence model was not able to predict the deterioration observed in the experiment. It must be stated that even though the SST model under predicted the wall temperature of the experiment, an over prediction is always preferred than under prediction for the use of safety analysis. Even though over prediction is preferred, it must be within a good limit.

4.1.4 Turbulence Models comparison at 40 kW/m^2

The Figure 4.4 shows the comparison of wall temperature distribution which was predicted by six low Reynolds models; κ-ε AKN, EB, standard low-Re and V2F and k-ω models with heat flux of 40 kW/m^2 and mass flux of 314 kg/m^{2}s. The results on the various simulations were also compared with the experimental data of Kim et al. [21]. From the Figure, the experimental data predicted heat transfer deterioration around X/D = 20.

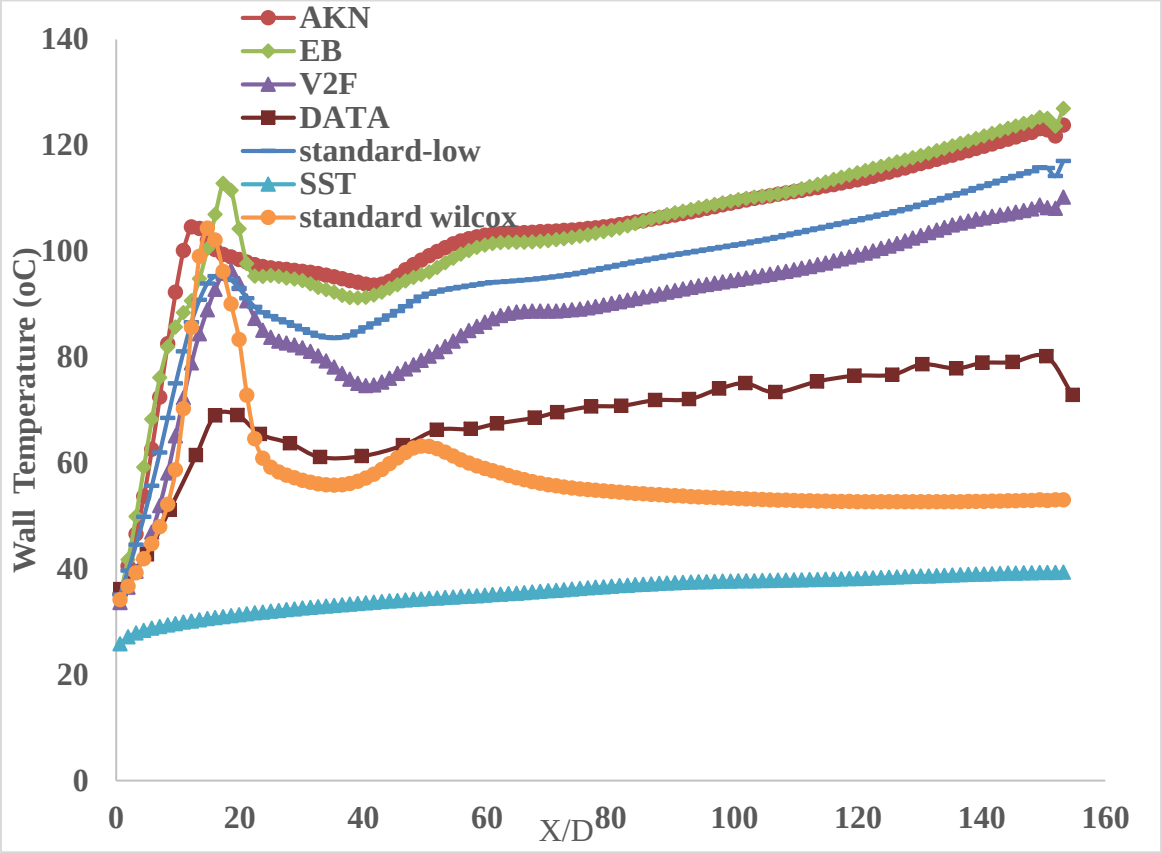

Figure 4.4: Turbulence Models comparison of wall temperature at heat flux of 40 kW/m^2

4.2 Fluid Velocity within the Circular Tube

From the wall temperatures graphs obtained in Figures 4.1 – 4.4 and for the sake of brevity, only the κ-ε models would be considered in this part of the research. Figure 4.5 shows the velocity profile of the circular tube at heat flux of 23 kW/m^2 and mass flux of 314 kg/m^{2}s at a distance of 1.4 m along the tube. From the Figure 4.5, it can be observed that the various turbulence models predict the radial velocity profile. It can be seen from the Figure that the velocity obtained from the simulation initially has a value around 0.3 m/s. As the simulation continues, the velocity increases steadily as it gets to the walls of the tube. The maximum of the velocity is achieved just before the prism layer of the tube was created. The profile from here shows a sharp downward trend. This downward trend shows that there truly is a laminar sub-layer just beneath the walls and mimicked by the prism layer created in the physical model. In this laminar sub-layer, it shows that fluid movement is very slow and can be described as the molecules of the CO_2 coming to a stop.

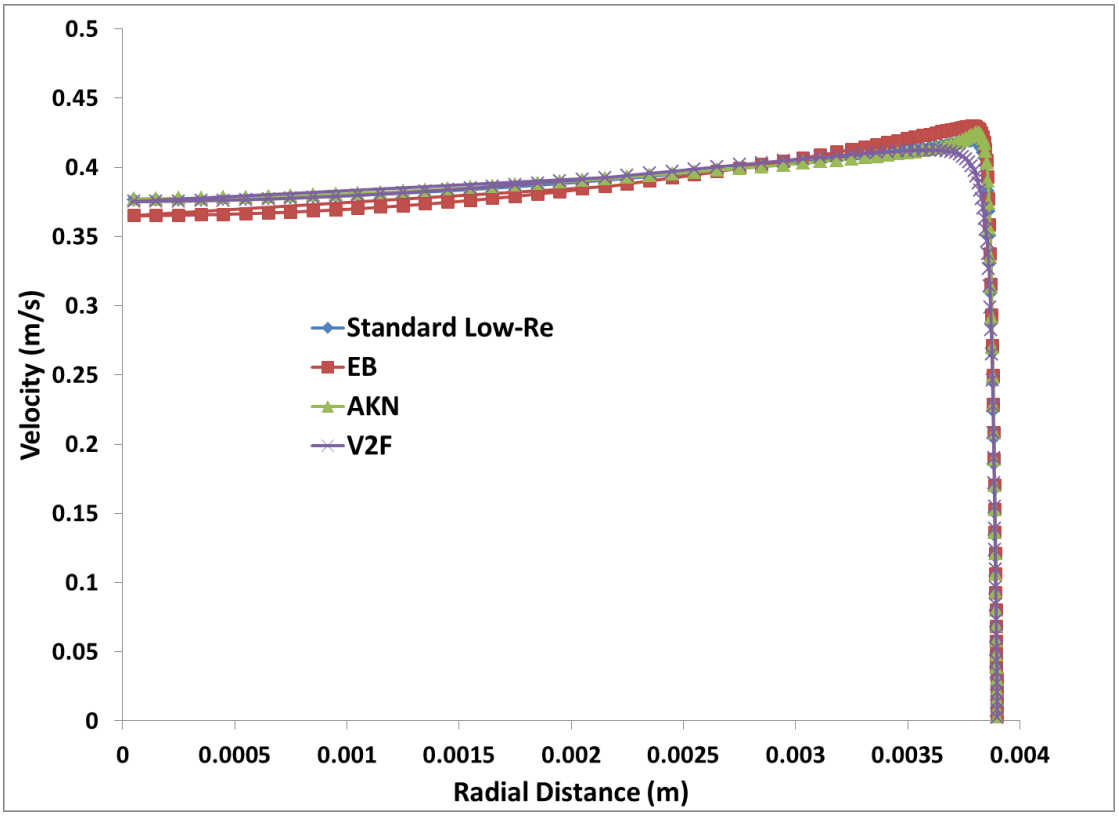

Figure 4.5: Radial velocity at a distance of 1.4 m with heat flux of 23 kW/m^2

It is worth noting that even though the various κ-ε models predicted the same shape of velocity, there seems to be some differences in the velocities obtained by the different models. Velocity profile details of other radial distances with different heat fluxes are presented in Appendix I.

4.3 Fluid Density within the Circular Tube

Again for the sake of brevity, only the κ-ε models used in this research would be considered since they gave appreciable results when compared with the wall temperatures obtained from the experimental data. Figure 4.6 show the radial density profile of the flow with supercritical CO_2 at an axial distance of 1.4 m with a heat flux of 23 kW/m^2. The κ-

ε models of AKN, EB, Standard Low-Reynolds and V2F describes the density of supercritical CO_2 at 8 MPa at a radial distance of 1.4 m. From the Figure, the supercritical fluid at the middle of the tube shows a relatively constant density. As the fluid come close to the walls of the tube, the density begins to drop very sharply. It can be said that its drop is almost instantaneous showing that the fluid has reached it pseudo-critical point. This is the region which has proven challenging for current correlations in the field of engineering to deal with.

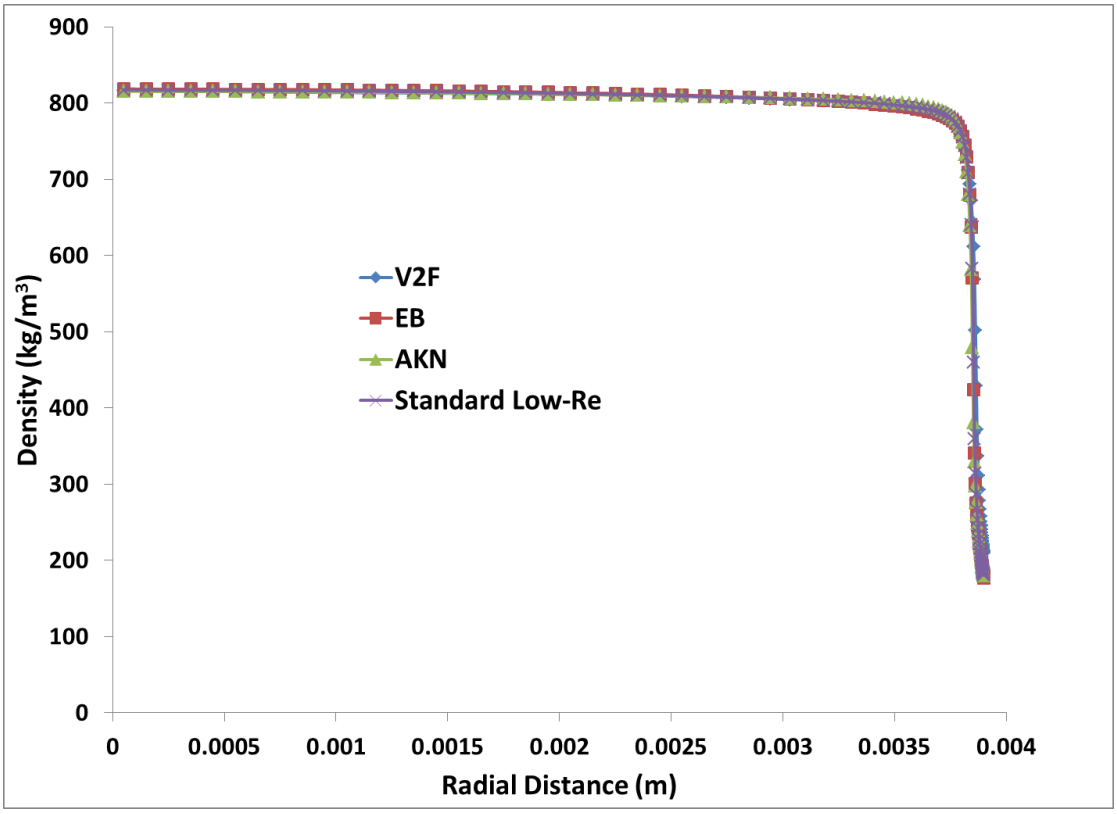

Figure 4.6: shows the density at a distance of 1.4 m with heat flux of 23 kW/m^2

Density profile details of other radial distances with different heat fluxes are also presented in Appendix II.

4.4 y+ Wall Treatment

The wall y+ is a non-dimensional distance and is often used in CFD to describe how coarse or fine a mesh is for a particular flow. It is a ratio between turbulent and laminar influence in a cell. The low y+ wall treatment is suitable only for low Reynolds turbulence models in which it is assumed that the viscous sub-layer is properly resolved. Turbulence flows are significantly affected by the presence of walls, where the viscous-affected regions have large gradients in the solution variable and accurate presentation of the near-wall determines successful prediction of wall bounded turbulence flow.

Very close to the wall, viscous damping reduces the tangential velocity fluctuations, while kinematic blocking reduces the normal fluctuations. Towards the outer part of the near-wall region, however, the turbulence is rapidly augmented by the production of turbulent kinetic energy due to the large gradients in mean velocity.

Figure 4.7 shows the heat fluxes of 20, 23, 30 and 40 kW/m^2, it indicates that the heat fluxes increases as the y+ wall profile moves away from the near-wall region, this is due to the effect of viscosity, buoyance, acceleration and the friction of the turbulence modification.

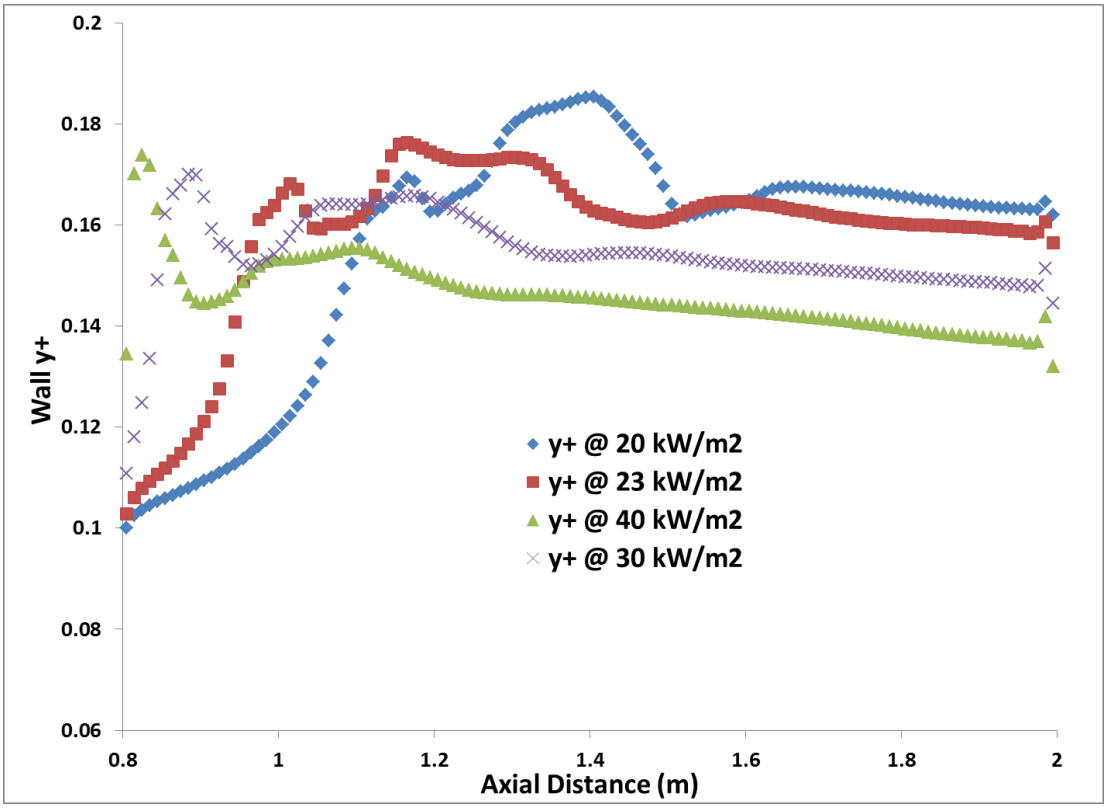

Figure 4.7: y+ wall treatment at different heat fluxes

CHAPTER FIVE: CONCLUSIONS AND RECOMMENDATIONS

5.1 CONCLUSIONS

Analysis of heat transfer in circular tube with super critical CO_2 has been carried out using STAR-CCM$^+$. The results of the simulation has been found to be able to reproduce the general features exhibited in the experimental data, However, in some cases, the details of the simulation results were very different from the experimental data, the κ-ε models; AKN, EB, V2F and Standard low-Reynolds turbulence models have better capabilities to predict the heat transfer behavior of supercritical CO_2 flowing upward in circular tube. The turbulence models were all able to predict the heat transfer deterioration both quantitatively and qualitatively.

The simulation was performed for various heat fluxes (20, 23, 30, 40 kW/m^2) and a constant mass flux of 314 kg/m^{2}s. It was noted that as the heat flux was increased with constant mass flux, the predictability of the models was better in the case of the κ-ε models. The models were able to improve their predictability in terms of where the deterioration was observed experimentally.

Results from the various simulations show that there is a laminar sub-layer or what is termed as a buffer, present. The effect of this buffer can be seen in the plot of velocity against the radial distance of the circular tube. Based on the results of simulations, it is noted that at low heat flux, the effect of deterioration is still evident in the κ-ε models even though this phenomena is not experienced in the experiment. This was attributed to the heat transfer correlation used in the development of the code. At high heat fluxes the deterioration observed in experiment was also evident during the simulation even though it was over predicted by the models used.

It can be said that the effect of deterioration has been effectively modeled and accounted for. The effect of heat transfer enhancement was neither seen in any of the cases studied during the research nor was it seen in the experimental case used as the benchmark experiment for this research.

The behaviour of the κ-ε low-Reynolds models namely; AKN, EB, standard low-Re and V2F show superior character than κ-ω; SST and standard Wilcox as experienced in the experiment. It indicates that the κ-ω turbulence model are unsuitable for this problem, Hence the κ-ε low-Reynolds turbulence models are recommended for the prediction of heat transfer deterioration since they have better capabilities to predict the heat transfer behavior of supercritical CO_2 as compared to the experimental data under the same working conditions.

5.2 RECOMMENDATIONS

- Since most of the models are over predicting and some are under predicting the heat transfer deterioration region as compared to the experimental data, correlations which could be used to determine onset of heat transfer deterioration and calculating the heat transfer coefficient should be studied in details for supercritical fluids.
- The hydraulic diameter of the tube is one of the most important parameters, because heat transfer decreases by increasing the diameter of the tube therefore it is important to study in details different hydraulic parameters and how they enhance or deteriorate a fluid flow for both water and CO_2.

- Special attention should be given to the conditions of heat transfer increase during turbulent fluid flow because of severe property variations of fluid at supercritical pressures and temperatures, The Dittus-Boelter correlation could be used as a basis to designing new heat transfer correlation to fit supercritical fluids for the applications to supercritical water reactor.

REFERENCES

[1] Shires, G.L and Polezhaev, Y.V. (1998). International Encyclopedia of Heat & Mass Transfer. Supercritical heat transfer (Boca R., ed), pp 1112-1117 CRC Press, Forida, USA.

[2] Duffey, R.B., Pioro, I., Zhou, T., Zirn, U., Kuran, S., Khartabil, H. and Naidin, M. (2008). Supercritical Water-Cooled Nuclear Reactors (SCWRs): Current and Future Concepts - Steam-Cycle. Paper presented at 16th International conference 11-15 May 2008, Florida, USA.

[3] Duffey, R.B. and Pioro I.L. (2005). Experimental heat transfer of supercritical carbon dioxide flowing inside channels. J Nuclear Engineering and Design 235:913–924.

[4] Naterer, G., Suppiah, S. and Lewis, M. (2009). Recent Canadian Advances in Nuclear-Based Hydrogen Production and the Thermochemical Cu-Cl Cycle. International Journal of Hydrogen Energy 34:6-17.

[5] Pioro, I.L., and Duffey, R.B. (2007). Heat Transfer and Hydraulic Resistance at Supercritical Pressures in Power Engineering Applications. Journal Nuclear Engineering and Design 1:79-91

[6] U.S. DOE (2002), A Technology Roadmap for Generation IV Nuclear Energy Systems, GIF-002-00 U.S DOE Nuclear Energy Research Advisory Committee and the Generation IV International Forum.

[7] Naidin, M., Pioro, I., Zirn, U., Mokry, S. and Naterer, G. (2009). Supercritical Water-Cooled NPPs with Co-Generation of Hydrogen: General Layout and Thermodynamic-Cycles Options. Paper presented at the 4th International Symposium on Supercritical Water-Cooled Reactors, 8-11 March, 2009, Heidelberg, Germany.

[8] Patanker S.V., Minkowyez, W.J. and Sparrow, E.M. (1980). Numerical Heat Transfer and Fluid Flow, Hemisphere Publishing Corporation, Washington, New York.

[9] Versteeg, H.K. and Malalasekera, W. (1995). An introduction to computational fluid dynamics. The finite method (John Wiley ed) Longman Scientific and Technical, New York, USA.

[10] Chang, K.C., Hsieh, W.D. and Chen, C.S. (1995). A modified low-Reynolds number Turbulence model applicable to recirculating flow in pipe expansion. Journal of fluid Engineering 117:417–423.

[11] Tulkki, V. (2006). Supercritical Water cooled Reactors. Master's Thesis, Helsinki University of Technology, Otaniemi Finland.

[12] Jiang, P. X., Li, M., Xu, Y. J. and Ren, Z. P. (2002). Numerical simulation of convection heat transfer of CO_2 at super-critical pressures in porous media. Journal of Engineering Thermophysics 23:200-202.

[13] Krasnoshchekov, E. A. and Protopopov, V. S. (1966). Experimental study of heat exchange in carbon dioxide in the supercritical range at high temperature drops. (in Russian) Teplofizika Vysokikh Temperature 4:3:389-398.

[14] Gallaway, T., Antal, S. P. and Podowski, M. Z. (2008). Multidimensional Model of Fluid Flow and Heat Transfer in Generation-IV Supercritical Water Reactor. J Nuclear Engineering & Design 238.

[15] Watts, M. J. (1980). Heat transfer to supercritical pressure water – Mixed convection with up flow and down flow in a vertical tube. PhD Thesis. University of Manchester, UK.

[16] Jackson, J. D., and Hall, W. B. (1979). Forced convection heat transfer to fluids at supercritical pressure, in: turbulent forced convection in channels and bundles. J Nuclear Engineering & Design 238.

2:321-334

[17] Podowski, M.Z. (2008). Thermal-Hydraulic Aspects of SCWR Design. Journal of Power and Energy Systems 2:1:6-8

[18] Jackson, J.D. and Hall, W.B. (1980). Influences of buoyancy on heat transfer to fluids flowing in vertical tubes under turbulent conditions. Turbulent Forced Convection in Channels and Rod Bundles (Kakacs S. and Spalding D.B, ed) pp 563-611. Hemisphere Publishing Corporation, USA.

[19] Hall, W. B. (1971). Heat Transfer near the Critical Point, Advances in Heat Transfer, International Journal of Heat and Mass transfer 7:1-86.

[20] Shitsman, M.E. (1959). Heat transfer to water, oxygen and carbon dioxide in the approximately critical range Teploenergetiky. 1:68-72.

[21] Jong K., Hong K.J., Jung Y. Y. and Sik L. (2005). Experimental Study on Heat Transfer Characteristics of turbulence Supercritical Flow in Vertical Circular/ non circular Tubes.

School of Mechanical and Aerospace Engineering, Seoul National University, Seoul 151-742

[22] Cheng, X., Kuang, B. and Yang, Y. H. (2007). Numerical analysis of Heat Transfer in supercritical water Cooled Flow Channels. J Nuclear Engineering Design 240-252.

[23] Yang, J., Oka, Y., Ishiwatari, Y., Liu, J. and Yoo, J. (2007). Numerical investigation of heat transfer in upward flows of supercritical water in circular tubes and tight fuel rod bundles. J Nuclear Engineering Design 237:420–430.

[24] Department of Energy (DOE), (2002). A Technology Roadmap for Generation IV Nuclear Energy Systems. Washington, D. C., Department of Energy.

[25] Dittus, F. W. and Boelter, L. M. K. (1930). Heat Transfer in Automobile Radiators of the Tubular Type, University of California, Berkeley. Publications on Engineering 2:13:443-461.

[26] Pioro, I.L. and Duffey, R.B. (2007). Heat Transfer and Hydraulic Resistance at Supercritical Pressures in Power Engineering Applications, pp 328, ASME Press, New York, USA.

[27] Pioro, I. (2011). The Potential Use of Supercritical Water-Cooling in Nuclear Reactors.Science, Technology, and Applications (Krivit S.B., Lehr J.H. and Kingery T.B ed) pp 309-347. Wiley & Sons, Hoboken, New Jersey, USA.

[28] Podowski, M. Z. (1992). Instabilities in Two-Phase Systems, in Boiling Heat Transfer, Elsevierl Publishing Corporation.

[29] Gallaway, T., Antal, S.P. and Podowski, M.Z. (2008). Multidimensional Model of Fluid Flow and Heat Transfer in Generation-IV Supercritical Water Reactors. J Nuclear Engineering & Design 238.

[30] Oka, Y., Koshizuka, S., Ishiwatari, Y. and Yamaji, A. (2010). Super Light Water Reactors and Super-Fast Reactors. Supercritical- Pressure Light Water Reactor, Springer ISBN 978-1-4419-6034-4.

[31] Masuyama, F. (2001). History of Power Plants and Progress in Heat Resistant Steels. ISIJ International journal 41:6:612

[32] Scott, D. and Nilsson, P. (1999). Competitiveness of Future Coal-Fired Units in Different Countries. Report on IAEA Coal Research 1999. 80:10:2757-2764.

[33] McEligot D.M. and Jackson J.D. (2004). Deterioration criteria for convective heat transfer in gas flow through non-circular ducts, Short Communication. J Nuclear Engineering and Design 232:327–333.

[34] Yamada, K., Sakurai, S., Asanuma, Y., Hamazaki, R., Ishiwatari, Y., and Kitoh K. (2011). Overview of the Japanese SCWR concept developed under the GIF collaboration. Paper presented at the 6th Joint International conference 13-16 March 2011, Vancouver, Canada.

[35] Schulenberg, T. and Starflinger, J. (2012). High performance light water reactor – design and analyses, KIT Scientific Publishing.

[36] Ville, T. (2006). Supercritical Water Reactors A Survey on International State of Research in 2006. Master's Thesis. Helsinki University of Technology, Helsinki, Finland

[37] Luby, P. and Susta, M. R. (2002). Steam Power Plants – New Wave of Super criticality, Power-Gen Europe, Milan, Italy.

[38] Oakey, J.E., Allen, D.H. and Staubli, M. (2000). Power Generation in the 21st Century – The New European COST Action, Cambridge, UK.

[39] Pioro I.L., Khartabil H.F. and Duffey R.B. (2004). Heat Transfer to Supercritical Fluids Flowing in Channels – Empirical Correlations (Survey). J Nuclear Engineering Design. 230:69-91.

[40] Kaneda J., Kasahara, S., Kano, F., Saito, N., Shikama, T. and Matsui H. (2011). Material development for supercritical water-cooled reactor. Paper presented at the 6th Joint International conference 13-16 March 2011, Vancouver, Canada.

[41] Bringer, R.P.and Smith, J.M. (1957). Heat transfer in the critical region. AIChE J 3:1:49–55.

[42] Wood, R.D. and Smith, J.M. (1964). Heat transfer in the critical region–temperature and velocity profiles in turbulent flow. AIChE J 10:2:180–186

[43] Tanaka, H., Nishiwaki, N., Hirata, M. and Tsuge, A. (1971). Forced convection heat transfer to fluid near critical point flowing in circular tube. International Journal. Heat Mass Transfer 14:6:739–750.

[44] Baskov, V.L., Kuraeva, I.V. and Protopopov, V.S. (1977). Heat transfer with the turbulent flow of a liquid at supercritical pressure in tubes under cooling conditions. Journal Nuclear Engineering Design 15:1:81–86.

[45] Danga, C. B. and Hihara, E. J. (2004). In-Tube Cooling Heat Transfer of Supercritical Carbon Dioxide. Part 1: Experimental Measurement. International Journal of Refrigeration 27:7:736-747.

[46] Kim, J. K., Jeon, H. K. and Lee, J. S. (2007). Wall temperature measurement and heat transfer correlation of turbulent supercritical carbon dioxide flow in vertical circular/noncircular tubes. J Nuclear Engineering and Design 237:1795–1802.

[47] Zhang, Y. (2006). Convection Heat Transfer of CO_2 at Supercritical Pressures in Mini/Micro Scale Tubes. M.Sc. Dissertation, Tsinghua University Beijing, China.

[48] CD-Adapco, (2012), User Guide, STAR-CCM+ Version7.04006

[49] Chien, K.Y. (1982). Predictions of channel and boundary-layer flows with a low Reynolds number turbulence model. AIAA Journal 23:33–38.

[50] Abe, K., Kondoh, T. and Nagano, Y. (1994). A new turbulence model for predicting fluid flow and heat transfer in separating and reattaching flows—I. Flow field calculations. International Journal, Heat Mass Transfer 3:139–151.

[51] Davidson, L., Nielsen, P. V. and Sveninsson A. (2003). Modification of V2F model for computing the flow in a 3D wall jet. J turbulence Heat and Mass Transfer 7:577-584.

[52] Lien, L.S., Kalitz G. and Durbin, P. A. (1998). RANS modeling for compressible and transitional flows, center for Turbulence Research Proceedings of Summer Program.

[53] Durbin, P. A. (1986). On the k-epsilon stagnation point anomaly. J. turbulence Heat and Mass Transfer 17:89-90.

[54] Jones, W. P. and Launder, B. E. (1972). The prediction of Laminarization with a Two-Equation model of turbulence model, International Journal, Heat and mass Transfer. 15: 301-314.

[55] Launder, B. E. and Sharma, B. I. (1972). Application of Energy Dissipation Model of Turbulence to calculation of Flow near Spinning Disc. International journal Heat and Mass Transfer 2:131-138.

[56] Abe, K., Kondoh T. and Nagano, Y. (1994). A new turbulence model for predicting fluid flow and heat transfer in separated and buoyant flows 1 Flow Field calculations. International journal Heat transfer 37:139-151.

[57] Durbin, P. A. (1993). A Reynolds stress model for near-wall turbulence. Journal of fluid mechanics. J Nuclear Engineering & Design 249:1:465-498.

[58] Manceau, R. and Hanjalic, K. (2002). Elliptic blending model: A new near-wall Reynolds-stress turbulence closure. Physics of fluids International journal Heat transfer. J Nuclear Engineering & Design 14:744.

[59] Menter, F.R. (1994). Two-equation eddy-viscosity turbulence models for engineering applications. AIAA journal 32:8:1598–1605.

[60] Ranz, W.E. and Marshall, W.R. (1952). Evaporation from drops Part I and II, Chemical Engineering Program. International journal Heat transfer 48:3:141.

APPENDICES

APPENDIX I: Radial velocity data at different axial distances and heat fluxes

AKN model simulation results data

Table 1: AKN model data at flux of 20 kW/m^2

Position [0.0, 1.0, 0.0] (m)-0.8 m	Velocity: Component 0-0.8 m (m/s)	Position [0.0, 1.0, 0.0] (m)-1.0 m	Velocity: Component 0-1.0 m (m/s)	Position [0.0, 1.0, 0.0] (m)-1.2 m	Velocity: Component 0-1.2 m (m/s)	Position [0.0, 1.0, 0.0] (m)-1.4 m	Velocity: Component 0-1.4 m (m/s)	Position [0.0, 1.0, 0.0] (m)-1.6 m	Velocity: Component 0-1.6 m (m/s)	Position [0.0, 1.0, 0.0] (m)-1.8 m	Velocity: Component 0-1.8 m (m/s)	Position [0.0, 1.0, 0.0] (m)-2.0 m	Velocity: Component 0-2.0 m (m/s)	Position [0.0, 1.0, 0.0] (m)-0.01 m	Velocity: Component 0-0.01 m (m/s)
0.0039	0.4337	0.0039	0.4144	0.0039	0.3708	0.0039	0.2615	0.0039	0.3860	0.0039	0.3822	0.0039	0.3999	0.0038	0.2599
0.0039	0.4336	0.0039	0.4144	0.0039	0.3708	0.0039	0.2623	0.0039	0.3860	0.0039	0.3823	0.0039	0.3999	0.0038	0.2476
0.0039	0.4333	0.0039	0.4143	0.0039	0.3709	0.0039	0.2641	0.0039	0.3861	0.0039	0.3825	0.0039	0.4001	0.0038	0.2351
0.0039	0.4329	0.0039	0.4142	0.0039	0.3711	0.0039	0.2667	0.0039	0.3862	0.0039	0.3829	0.0039	0.4004	0.0038	0.2226
0.0039	0.4324	0.0039	0.4140	0.0039	0.3712	0.0039	0.2701	0.0039	0.3864	0.0039	0.3833	0.0039	0.4007	0.0038	0.2100
0.0039	0.4318	0.0039	0.4138	0.0039	0.3715	0.0039	0.2743	0.0039	0.3866	0.0039	0.3838	0.0039	0.4011	0.0038	0.1976
0.0039	0.4310	0.0039	0.4136	0.0039	0.3718	0.0039	0.2790	0.0039	0.3869	0.0039	0.3845	0.0039	0.4016	0.0039	0.1853
0.0039	0.4301	0.0039	0.4133	0.0039	0.3721	0.0039	0.2842	0.0039	0.3872	0.0039	0.3852	0.0039	0.4022	0.0039	0.1732
0.0039	0.3164	0.0039	0.4129	0.0039	0.3725	0.0039	0.2899	0.0039	0.3875	0.0039	0.3860	0.0039	0.4029	0.0039	0.1614
0.0039	0.3113	0.0039	0.4125	0.0039	0.3730	0.0039	0.2962	0.0039	0.3879	0.0039	0.3869	0.0039	0.4036	0.0039	0.1500
0.0039	0.3061	0.0039	0.4121	0.0039	0.3735	0.0039	0.3028	0.0039	0.3884	0.0039	0.3880	0.0039	0.4044	0.0039	0.1389
0.0039	0.3010	0.0039	0.4116	0.0039	0.3741	0.0039	0.3096	0.0039	0.3888	0.0039	0.3891	0.0039	0.4053	0.0039	0.1282
0.0039	0.2957	0.0039	0.4111	0.0039	0.3747	0.0039	0.3166	0.0039	0.3894	0.0039	0.3902	0.0039	0.4062	0.0039	0.1180
0.0039	0.2905	0.0039	0.4105	0.0039	0.3754	0.0039	0.3236	0.0039	0.3899	0.0039	0.3915	0.0039	0.4073	0.0039	0.1082
0.0039	0.2851	0.0039	0.4098	0.0039	0.3762	0.0039	0.3306	0.0039	0.3905	0.0039	0.3928	0.0039	0.4084	0.0039	0.0988

Table 2: AKN model data at heat flux of 23 kW/m^2

Position [0.0, 1.0, 0.0] (m)-0.8 m	Velocity: Component 0-0.8 m (m/s)	Position [0.0, 1.0, 0.0] (m)-1.0 m	Velocity: Component 0-1.0 m (m/s)	Position [0.0, 1.0, 0.0] (m)-1.2 m	Velocity: Component 0-1.2 m (m/s)	Position [0.0, 1.0, 0.0] (m)-1.4 m	Velocity: Component 0-1.4 m (m/s)	Position [0.0, 1.0, 0.0] (m)-1.6 m	Velocity: Component 0-1.6 m (m/s)	Position [0.0, 1.0, 0.0] (m)-1.8 m	Velocity: Component 0-1.8 m (m/s)	Position [0.0, 1.0, 0.0] (m)-2.0 m	Velocity: Component 0-2.0 m (m/s)	Position [0.0, 1.0, 0.0] (m)-0.01 m	Velocity: Component 0-0.01 m (m/s)
0.0039	0.0008	0.0035	0.3577	0.0001	0.3211	0.0039	0.3773	0.0039	0.0030	0.0039	0.0029	0.0039	0.0029	0.0039	0.0011
0.0039	0.0026	0.0035	0.3543	0.0002	0.3212	0.0039	0.3774	0.0039	0.0092	0.0039	0.0091	0.0039	0.0089	0.0039	0.0034
0.0039	0.0045	0.0036	0.3507	0.0003	0.3213	0.0039	0.3775	0.0039	0.0160	0.0039	0.0158	0.0039	0.0154	0.0039	0.0060
0.0039	0.0067	0.0036	0.3469	0.0004	0.3215	0.0039	0.3778	0.0039	0.0234	0.0039	0.0231	0.0039	0.0226	0.0039	0.0087
0.0039	0.0090	0.0036	0.3430	0.0005	0.3218	0.0039	0.3780	0.0039	0.0315	0.0039	0.0311	0.0039	0.0304	0.0039	0.0117
0.0039	0.0115	0.0037	0.3389	0.0006	0.3221	0.0039	0.3784	0.0039	0.0402	0.0039	0.0398	0.0039	0.0389	0.0039	0.0150
0.0039	0.0144	0.0037	0.3347	0.0007	0.3225	0.0039	0.3788	0.0039	0.0498	0.0039	0.0493	0.0039	0.0481	0.0039	0.0186
0.0039	0.0174	0.0037	0.3303	0.0008	0.3229	0.0039	0.3793	0.0039	0.0602	0.0039	0.0595	0.0039	0.0582	0.0039	0.0224
0.0039	0.0208	0.0037	0.3256	0.0009	0.3234	0.0039	0.3799	0.0039	0.0715	0.0039	0.0707	0.0039	0.0691	0.0039	0.0266
0.0039	0.0245	0.0037	0.3208	0.0010	0.3240	0.0039	0.3805	0.0039	0.0837	0.0039	0.0828	0.0039	0.0810	0.0039	0.0311
0.0039	0.0286	0.0037	0.3157	0.0011	0.3247	0.0039	0.3812	0.0039	0.0969	0.0039	0.0959	0.0039	0.0938	0.0039	0.0359
0.0039	0.0330	0.0038	0.3103	0.0012	0.3254	0.0039	0.3819	0.0039	0.1111	0.0039	0.1100	0.0039	0.1077	0.0039	0.0412
0.0039	0.0379	0.0038	0.3045	0.0013	0.3262	0.0039	0.3827	0.0039	0.1264	0.0039	0.1252	0.0039	0.1226	0.0039	0.0468
0.0039	0.0432	0.0038	0.2984	0.0014	0.3272	0.0039	0.3836	0.0039	0.1428	0.0039	0.1415	0.0039	0.1387	0.0039	0.0529
0.0039	0.0490	0.0038	0.2920	0.0015	0.3282	0.0039	0.3845	0.0039	0.1604	0.0039	0.1590	0.0039	0.1560	0.0039	0.0594

Table 3: AKN model data at heat flux of 30 kW/m^2

Position [0.0, 1.0, 0.0] (m)-0.8 m	Velocity: Component 0-0.8 m (m/s)	Position [0.0, 1.0, 0.0] (m)-1.0 m	Velocity: Component 0-1.0 m (m/s)	Position [0.0, 1.0, 0.0] (m)-1.2 m	Velocity: Component 0-1.2 m (m/s)	Position [0.0, 1.0, 0.0] (m)-1.4 m	Velocity: Component 0-1.4 m (m/s)	Position [0.0, 1.0, 0.0] (m)-1.6 m	Velocity: Component 0-1.6 m (m/s)	Position [0.0, 1.0, 0.0] (m)-1.8 m	Velocity: Component 0-1.8 m (m/s)	Position [0.0, 1.0, 0.0] (m)-2.0 m	Velocity: Component 0-2.0 m (m/s)	Position [0.0, 1.0, 0.0] (m)-0.01 m	Velocity: Component 0-0.01 m (m/s)
0.0039	0.0047	0.0035	0.4046	0.0039	0.3452	0.0039	0.3787	0.0039	0.0163	0.0039	0.0162	0.0039	0.0153	0.0039	0.0061
0.0039	0.0065	0.0035	0.4088	0.0039	0.3454	0.0039	0.3788	0.0039	0.0224	0.0039	0.0223	0.0039	0.0211	0.0039	0.0084
0.0039	0.0084	0.0036	0.4130	0.0039	0.3458	0.0039	0.3789	0.0039	0.0291	0.0039	0.0289	0.0039	0.0274	0.0039	0.0109
0.0039	0.0106	0.0036	0.4171	0.0039	0.3465	0.0039	0.3792	0.0039	0.0365	0.0039	0.0362	0.0039	0.0343	0.0039	0.0136
0.0039	0.0130	0.0036	0.4212	0.0039	0.3473	0.0039	0.3795	0.0039	0.0444	0.0039	0.0441	0.0039	0.0418	0.0039	0.0166
0.0039	0.0155	0.0037	0.4252	0.0039	0.3484	0.0039	0.3799	0.0039	0.0531	0.0039	0.0527	0.0039	0.0500	0.0039	0.0198
0.0039	0.0184	0.0037	0.4292	0.0039	0.3497	0.0039	0.3803	0.0039	0.0626	0.0039	0.0622	0.0039	0.0590	0.0039	0.0233
0.0039	0.0215	0.0037	0.4331	0.0039	0.3511	0.0039	0.3809	0.0039	0.0728	0.0039	0.0724	0.0039	0.0687	0.0039	0.0271
0.0039	0.0249	0.0037	0.4371	0.0039	0.3527	0.0039	0.3815	0.0039	0.0840	0.0039	0.0835	0.0039	0.0793	0.0039	0.0313
0.0039	0.0286	0.0037	0.4410	0.0039	0.3544	0.0039	0.3822	0.0039	0.0961	0.0039	0.0956	0.0039	0.0909	0.0039	0.0357
0.0039	0.0326	0.0037	0.4450	0.0039	0.3562	0.0039	0.3830	0.0039	0.1091	0.0039	0.1086	0.0039	0.1034	0.0039	0.0405
0.0039	0.0371	0.0038	0.4490	0.0039	0.3582	0.0039	0.3839	0.0039	0.1232	0.0039	0.1227	0.0039	0.1169	0.0039	0.0457
0.0039	0.0420	0.0038	0.4530	0.0039	0.3602	0.0039	0.3848	0.0039	0.1384	0.0039	0.1379	0.0039	0.1316	0.0039	0.0513
0.0039	0.0473	0.0038	0.4570	0.0039	0.3624	0.0039	0.3858	0.0039	0.1547	0.0039	0.1543	0.0039	0.1474	0.0039	0.0573
0.0039	0.0531	0.0038	0.4610	0.0039	0.3646	0.0039	0.3869	0.0039	0.1722	0.0039	0.1719	0.0039	0.1643	0.0039	0.0637

Table 4: AKN model data at heat flux of 40 kW/m^2

Position [0.0, 1.0, 0.0] (m)-0.8 m	Velocity: Component 0-0.8 m (m/s)	Position [0.0, 1.0, 0.0] (m)-1.0 m	Velocity: Component 0-1.0 m (m/s)	Position [0.0, 1.0, 0.0] (m)-1.2 m	Velocity: Component 0-1.2 m (m/s)	Position [0.0, 1.0, 0.0] (m)-1.4 m	Velocity: Component 0-1.4 m (m/s)	Position [0.0, 1.0, 0.0] (m)-1.6 m	Velocity: Component 0-1.6 m (m/s)	Position [0.0, 1.0, 0.0] (m)-1.8 m	Velocity: Component 0-1.8 m (m/s)	Position [0.0, 1.0, 0.0] (m)-2.0 m	Velocity: Component 0-2.0 m (m/s)	Position [0.0, 1.0, 0.0] (m)-0.01 m	Velocity: Component 0-0.01 m (m/s)
0.004	0.001	0.003	0.427	0.004	0.376	0.004	0.387	0.004	0.003	0.004	0.003	0.004	0.003	0.004	0.001
0.004	0.003	0.004	0.430	0.004	0.376	0.004	0.387	0.004	0.009	0.004	0.009	0.004	0.008	0.004	0.003
0.004	0.005	0.004	0.433	0.004	0.376	0.004	0.387	0.004	0.016	0.004	0.015	0.004	0.014	0.004	0.006
0.004	0.007	0.004	0.436	0.004	0.376	0.004	0.387	0.004	0.023	0.004	0.023	0.004	0.021	0.004	0.009
0.004	0.010	0.004	0.438	0.004	0.377	0.004	0.388	0.004	0.031	0.004	0.030	0.004	0.028	0.004	0.012
0.004	0.012	0.004	0.441	0.004	0.377	0.004	0.389	0.004	0.040	0.004	0.039	0.004	0.036	0.004	0.015
0.004	0.015	0.004	0.443	0.004	0.378	0.004	0.389	0.004	0.049	0.004	0.048	0.004	0.044	0.004	0.019
0.004	0.019	0.004	0.446	0.004	0.378	0.004	0.390	0.004	0.060	0.004	0.059	0.004	0.054	0.004	0.022
0.004	0.022	0.004	0.448	0.004	0.379	0.004	0.391	0.004	0.071	0.004	0.070	0.004	0.064	0.004	0.027
0.004	0.026	0.004	0.451	0.004	0.380	0.004	0.393	0.004	0.083	0.004	0.082	0.004	0.075	0.004	0.031
0.004	0.030	0.004	0.454	0.004	0.381	0.004	0.394	0.004	0.096	0.004	0.095	0.004	0.088	0.004	0.036
0.004	0.035	0.004	0.456	0.004	0.382	0.004	0.395	0.004	0.111	0.004	0.109	0.004	0.101	0.004	0.041
0.004	0.040	0.004	0.459	0.004	0.383	0.004	0.397	0.004	0.126	0.004	0.124	0.004	0.115	0.004	0.047
0.004	0.046	0.004	0.462	0.004	0.384	0.004	0.398	0.004	0.143	0.004	0.141	0.004	0.131	0.004	0.053
0.004	0.052	0.004	0.465	0.004	0.385	0.004	0.400	0.004	0.161	0.004	0.159	0.004	0.148	0.004	0.059

I-2 EB model simulation results data

Table 5: EB model data at heat flux of 20 kW/m^2

Position [0.0, 1.0, 0.0] (m)-0.8 m	Velocity: Component 0-0.8 m (m/s)	Position [0.0, 1.0, 0.0] (m)-1.0 m	Velocity: Component 0-1.0 m (m/s)	Position [0.0, 1.0, 0.0] (m)-1.2 m	Velocity: Component 0-1.2 m (m/s)	Position [0.0, 1.0, 0.0] (m)-1.4 m	Velocity: Component 0-1.4 m (m/s)	Position [0.0, 1.0, 0.0] (m)-1.6 m	Velocity: Component 0-1.6 m (m/s)	Position [0.0, 1.0, 0.0] (m)-1.8 m	Velocity: Component 0-1.8 m (m/s)	Position [0.0, 1.0, 0.0] (m)-2.0 m	Velocity: Component 0-2.0 m (m/s)	Position [0.0, 1.0, 0.0] (m)-0.01 m	Velocity: Component 0-0.01 m (m/s)
0.0039	0.4348	0.0039	0.4117	0.0039	0.3822	0.0039	0.3097	0.0039	0.3726	0.0039	0.3802	0.0039	0.3938	0.0038	0.2587
0.0039	0.4347	0.0039	0.4117	0.0039	0.3823	0.0039	0.3100	0.0039	0.3727	0.0039	0.3803	0.0039	0.3939	0.0038	0.2467
0.0039	0.4345	0.0039	0.4116	0.0039	0.3823	0.0039	0.3107	0.0039	0.3729	0.0039	0.3805	0.0039	0.3940	0.0038	0.2346
0.0039	0.4341	0.0039	0.4115	0.0039	0.3825	0.0039	0.3116	0.0039	0.3731	0.0039	0.3808	0.0039	0.3943	0.0038	0.2224
0.0039	0.4336	0.0039	0.4114	0.0039	0.3826	0.0039	0.3129	0.0039	0.3734	0.0039	0.3811	0.0039	0.3947	0.0038	0.2102
0.0039	0.4329	0.0039	0.4112	0.0039	0.3828	0.0039	0.3145	0.0039	0.3738	0.0039	0.3816	0.0039	0.3951	0.0038	0.1981
0.0039	0.4321	0.0039	0.4110	0.0039	0.3830	0.0039	0.3164	0.0039	0.3743	0.0039	0.3822	0.0039	0.3956	0.0039	0.1861
0.0039	0.4312	0.0039	0.4107	0.0039	0.3833	0.0039	0.3186	0.0039	0.3749	0.0039	0.3828	0.0039	0.3962	0.0039	0.1743
0.0039	0.3161	0.0039	0.4104	0.0039	0.3836	0.0039	0.3210	0.0039	0.3755	0.0039	0.3836	0.0039	0.3969	0.0039	0.1627
0.0039	0.3109	0.0039	0.4101	0.0039	0.3840	0.0039	0.3236	0.0039	0.3762	0.0039	0.3844	0.0039	0.3977	0.0039	0.1514
0.0039	0.3057	0.0039	0.4097	0.0039	0.3844	0.0039	0.3265	0.0039	0.3770	0.0039	0.3853	0.0039	0.3986	0.0039	0.1405
0.0039	0.3004	0.0039	0.4093	0.0039	0.3848	0.0039	0.3295	0.0039	0.3779	0.0039	0.3863	0.0039	0.3996	0.0039	0.1299
0.0039	0.2951	0.0039	0.4088	0.0039	0.3853	0.0039	0.3327	0.0039	0.3789	0.0039	0.3875	0.0039	0.4006	0.0039	0.1197
0.0039	0.2898	0.0039	0.4083	0.0039	0.3858	0.0039	0.3361	0.0039	0.3799	0.0039	0.3886	0.0039	0.4017	0.0039	0.1099

Table 6**:** EB model data at heat flux of 23 kW/m^2

Position [0.0, 1.0, 0.0] (m)-0.8 m	Velocity: Component 0-0.8 m (m/s)	Position [0.0, 1.0, 0.0] (m)-1.0 m	Velocity: Component 0-1.0 m (m/s)	Position [0.0, 1.0, 0.0] (m)-1.2 m	Velocity: Component 0-1.2 m (m/s)	Position [0.0, 1.0, 0.0] (m)-1.4 m	Velocity: Component 0-1.4 m (m/s)	Position [0.0, 1.0, 0.0] (m)-1.6 m	Velocity: Component 0-1.6 m (m/s)	Position [0.0, 1.0, 0.0] (m)-1.8 m	Velocity: Component 0-1.8 m (m/s)	Position [0.0, 1.0, 0.0] (m)-2.0 m	Velocity: Component 0-2.0 m (m/s)	Position [0.0, 1.0, 0.0] (m)-0.01 m	Velocity: Component 0-0.01 m (m/s)
0.0039	0.4348	0.0039	0.3959	0.0039	0.0031	0.0039	0.0029	0.0039	0.0029	0.0039	0.3895	0.0039	0.4037	0.0039	0.3640
0.0039	0.4347	0.0039	0.3962	0.0039	0.0094	0.0039	0.0088	0.0039	0.0090	0.0039	0.3896	0.0039	0.4038	0.0039	0.3640
0.0039	0.4344	0.0039	0.3965	0.0039	0.0164	0.0039	0.0154	0.0039	0.0156	0.0039	0.3898	0.0039	0.4040	0.0039	0.3640
0.0039	0.4340	0.0039	0.3974	0.0039	0.0240	0.0039	0.0225	0.0039	0.0228	0.0039	0.3901	0.0039	0.4043	0.0039	0.3640
0.0039	0.4335	0.0039	0.3975	0.0039	0.0322	0.0039	0.0302	0.0039	0.0306	0.0039	0.3904	0.0039	0.4047	0.0039	0.3640
0.0039	0.4329	0.0039	0.3977	0.0039	0.0412	0.0039	0.0387	0.0039	0.0392	0.0039	0.3909	0.0039	0.4051	0.0039	0.3640
0.0039	0.4321	0.0039	0.3978	0.0039	0.0510	0.0039	0.0478	0.0039	0.0485	0.0039	0.3914	0.0039	0.4057	0.0039	0.3640
0.0039	0.4311	0.0039	0.3979	0.0039	0.0617	0.0039	0.0578	0.0039	0.0586	0.0039	0.3921	0.0039	0.4064	0.0039	0.3640
0.0039	0.4301	0.0039	0.3980	0.0039	0.0732	0.0039	0.0686	0.0039	0.0696	0.0039	0.3928	0.0039	0.4071	0.0039	0.3640
0.0039	0.4289	0.0039	0.3980	0.0039	0.0856	0.0039	0.0802	0.0039	0.0815	0.0039	0.3936	0.0039	0.4080	0.0039	0.3640
0.0039	0.4275	0.0039	0.3981	0.0039	0.0991	0.0039	0.0928	0.0039	0.0943	0.0039	0.3945	0.0039	0.4089	0.0039	0.3640
0.0039	0.4260	0.0039	0.3981	0.0039	0.1135	0.0039	0.1063	0.0039	0.1082	0.0039	0.3955	0.0039	0.4100	0.0039	0.3640
0.0039	0.4244	0.0039	0.3972	0.0039	0.1291	0.0039	0.1209	0.0039	0.1231	0.0039	0.3966	0.0039	0.4111	0.0039	0.3640
0.0039	0.4227	0.0039	0.3970	0.0039	0.1457	0.0039	0.1364	0.0039	0.1391	0.0039	0.3978	0.0039	0.4124	0.0039	0.3640

Table 7: EB model data at heat flux of 30 kW/m^2

Position [0.0, 1.0, 0.0] (m)-0.8 m	Velocity: Component 0-0.8 m (m/s)	Position [0.0, 1.0, 0.0] (m)-1.0 m	Velocity: Component 0-1.0 m (m/s)	Position [0.0, 1.0, 0.0] (m)-1.2 m	Velocity: Component 0-1.2 m (m/s)	Position [0.0, 1.0, 0.0] (m)-1.4 m	Velocity: Component 0-1.4 m (m/s)	Position [0.0, 1.0, 0.0] (m)-1.6 m	Velocity: Component 0-1.6 m (m/s)	Position [0.0, 1.0, 0.0] (m)-1.8 m	Velocity: Component 0-1.8 m (m/s)	Position [0.0, 1.0, 0.0] (m)-2.0 m	Velocity: Component 0-2.0 m (m/s)	Position [0.0, 1.0, 0.0] (m)-0.01 m	Velocity: Component 0-0.01 m (m/s)
0.0039	0.4347	0.0035	0.3988	0.0039	0.3435	0.0039	0.3710	0.0039	0.0029	0.0039	0.0029	0.0039	0.0028	0.0039	0.0011
0.0039	0.4346	0.0035	0.4025	0.0039	0.3436	0.0039	0.3711	0.0039	0.0090	0.0039	0.0090	0.0039	0.0085	0.0039	0.0035
0.0039	0.4343	0.0036	0.4065	0.0039	0.3440	0.0039	0.3713	0.0039	0.0157	0.0039	0.0156	0.0039	0.0149	0.0039	0.0061
0.0039	0.4340	0.0036	0.4108	0.0039	0.3445	0.0039	0.3716	0.0039	0.0230	0.0039	0.0229	0.0039	0.0218	0.0039	0.0089
0.0039	0.4334	0.0036	0.4154	0.0039	0.3451	0.0039	0.3720	0.0039	0.0309	0.0039	0.0308	0.0039	0.0293	0.0039	0.0119
0.0039	0.4328	0.0037	0.4203	0.0039	0.3459	0.0039	0.3725	0.0039	0.0396	0.0039	0.0394	0.0039	0.0375	0.0039	0.0153
0.0039	0.4320	0.0037	0.4254	0.0039	0.3469	0.0039	0.3731	0.0039	0.0490	0.0039	0.0488	0.0039	0.0465	0.0039	0.0189
0.0039	0.4311	0.0037	0.4308	0.0039	0.3480	0.0039	0.3738	0.0039	0.0592	0.0039	0.0590	0.0039	0.0563	0.0039	0.0228
0.0039	0.4300	0.0037	0.4364	0.0039	0.3492	0.0039	0.3746	0.0039	0.0704	0.0039	0.0701	0.0039	0.0669	0.0039	0.0270
0.0039	0.4288	0.0037	0.4422	0.0039	0.3506	0.0039	0.3755	0.0039	0.0824	0.0039	0.0822	0.0039	0.0785	0.0039	0.0316
0.0039	0.4274	0.0037	0.4481	0.0039	0.3521	0.0039	0.3765	0.0039	0.0955	0.0039	0.0952	0.0039	0.0911	0.0039	0.0365
0.0039	0.4260	0.0038	0.4541	0.0039	0.3538	0.0039	0.3776	0.0039	0.1095	0.0039	0.1093	0.0039	0.1047	0.0039	0.0419
0.0039	0.4244	0.0038	0.4601	0.0039	0.3556	0.0039	0.3788	0.0039	0.1247	0.0039	0.1246	0.0039	0.1194	0.0039	0.0476
0.0039	0.4226	0.0038	0.4660	0.0039	0.3575	0.0039	0.3801	0.0039	0.1410	0.0039	0.1410	0.0039	0.1353	0.0039	0.0538

Table 8: EB model data at heat flux of 40 kW/m^2

Position [0.0, 1.0, 0.0] (m)-0.8 m	Velocity: Component 0-0.8 m (m/s)	Position [0.0, 1.0, 0.0] (m)-1.0 m	Velocity: Component 0-1.0 m (m/s)	Position [0.0, 1.0, 0.0] (m)-1.2 m	Velocity: Component 0-1.2 m (m/s)	Position [0.0, 1.0, 0.0] (m)-1.4 m	Velocity: Component 0-1.4 m (m/s)	Position [0.0, 1.0, 0.0] (m)-1.6 m	Velocity: Component 0-1.6 m (m/s)	Position [0.0, 1.0, 0.0] (m)-1.8 m	Velocity: Component 0-1.8 m (m/s)	Position [0.0, 1.0, 0.0] (m)-2.0 m	Velocity: Component 0-2.0 m (m/s)	Position [0.0, 1.0, 0.0] (m)-0.01 m	Velocity: Component 0-0.01 m (m/s)
0.0039	0.0009	0.0035	0.4314	0.0039	0.3625	0.0039	0.3840	0.0039	0.0029	0.0039	0.0029	0.0039	0.0026	0.0039	0.0011
0.0039	0.0027	0.0035	0.4355	0.0039	0.3626	0.0039	0.3841	0.0039	0.0090	0.0039	0.0088	0.0039	0.0081	0.0039	0.0035
0.0039	0.0047	0.0036	0.4393	0.0039	0.3628	0.0039	0.3843	0.0039	0.0156	0.0039	0.0153	0.0039	0.0141	0.0039	0.0061
0.0039	0.0070	0.0036	0.4429	0.0039	0.3632	0.0039	0.3847	0.0039	0.0228	0.0039	0.0225	0.0039	0.0206	0.0039	0.0089
0.0039	0.0094	0.0036	0.4463	0.0039	0.3636	0.0039	0.3851	0.0039	0.0307	0.0039	0.0303	0.0039	0.0278	0.0039	0.0119
0.0039	0.0120	0.0037	0.4494	0.0039	0.3642	0.0039	0.3857	0.0039	0.0394	0.0039	0.0388	0.0039	0.0357	0.0039	0.0152
0.0039	0.0149	0.0037	0.4524	0.0039	0.3649	0.0039	0.3864	0.0039	0.0488	0.0039	0.0481	0.0039	0.0442	0.0039	0.0188
0.0039	0.0181	0.0037	0.4551	0.0039	0.3657	0.0039	0.3873	0.0039	0.0590	0.0039	0.0582	0.0039	0.0536	0.0039	0.0228
0.0039	0.0216	0.0037	0.4576	0.0039	0.3666	0.0039	0.3882	0.0039	0.0701	0.0039	0.0692	0.0039	0.0638	0.0039	0.0270
0.0039	0.0253	0.0037	0.4599	0.0039	0.3676	0.0039	0.3892	0.0039	0.0823	0.0039	0.0812	0.0039	0.0750	0.0039	0.0316
0.0039	0.0295	0.0037	0.4620	0.0039	0.3688	0.0039	0.3904	0.0039	0.0954	0.0039	0.0942	0.0039	0.0871	0.0039	0.0365
0.0039	0.0340	0.0038	0.4639	0.0039	0.3700	0.0039	0.3917	0.0039	0.1096	0.0039	0.1084	0.0039	0.1003	0.0039	0.0418
0.0039	0.0389	0.0038	0.4657	0.0039	0.3714	0.0039	0.3931	0.0039	0.1250	0.0039	0.1237	0.0039	0.1147	0.0039	0.0476
0.0039	0.0442	0.0038	0.4672	0.0039	0.3728	0.0039	0.3946	0.0039	0.1416	0.0039	0.1402	0.0039	0.1303	0.0039	0.0537

I-3: Standard low-Re model simulation results data

Table 9: Standard low-Re model data at heat flux of 20 kW/m^2

Position [0.0, 1.0, 0.0] (m)-0.8 m	Velocity: Component 0-0.8 m (m/s)	Position [0.0, 1.0, 0.0] (m)-1.0 m	Velocity: Component 0-1.0 m (m/s)	Position [0.0, 1.0, 0.0] (m)-1.2 m	Velocity: Component 0-1.2 m (m/s)	Position [0.0, 1.0, 0.0] (m)-1.4 m	Velocity: Component 0-1.4 m (m/s)	Position [0.0, 1.0, 0.0] (m)-1.6 m	Velocity: Component 0-1.6 m (m/s)	Position [0.0, 1.0, 0.0] (m)-1.8 m	Velocity: Component 0-1.8 m (m/s)	Position [0.0, 1.0, 0.0] (m)-2.0 m	Velocity: Component 0-2.0 m (m/s)	Position [0.0, 1.0, 0.0] (m)-0.01 m	Velocity: Component 0-0.01 m (m/s)
0.0039	0.4332	0.0039	0.4096	0.0039	0.3704	0.0039	0.3521	0.0039	0.3796	0.0039	0.3858	0.0039	0.3948	0.0038	0.2600
0.0039	0.4331	0.0039	0.4096	0.0039	0.3705	0.0039	0.3523	0.0039	0.3797	0.0039	0.3858	0.0039	0.3948	0.0038	0.2475
0.0039	0.4329	0.0039	0.4095	0.0039	0.3705	0.0039	0.3526	0.0039	0.3798	0.0039	0.3860	0.0039	0.3950	0.0038	0.2349
0.0039	0.4325	0.0039	0.4094	0.0039	0.3707	0.0039	0.3530	0.0039	0.3800	0.0039	0.3862	0.0039	0.3952	0.0038	0.2222
0.0039	0.4321	0.0039	0.4093	0.0039	0.3708	0.0039	0.3536	0.0039	0.3803	0.0039	0.3865	0.0039	0.3954	0.0038	0.2096
0.0039	0.4315	0.0039	0.4091	0.0039	0.3710	0.0039	0.3543	0.0039	0.3806	0.0039	0.3868	0.0039	0.3958	0.0038	0.1970
0.0039	0.4307	0.0039	0.4089	0.0039	0.3713	0.0039	0.3552	0.0039	0.3809	0.0039	0.3873	0.0039	0.3962	0.0039	0.1847
0.0039	0.4299	0.0039	0.4087	0.0039	0.3716	0.0039	0.3563	0.0039	0.3814	0.0039	0.3878	0.0039	0.3967	0.0039	0.1726
0.0039	0.3160	0.0039	0.4084	0.0039	0.3719	0.0039	0.3574	0.0039	0.3819	0.0039	0.3883	0.0039	0.3972	0.0039	0.1608
0.0039	0.3111	0.0039	0.4081	0.0039	0.3723	0.0039	0.3587	0.0039	0.3824	0.0039	0.3890	0.0039	0.3979	0.0039	0.1493
0.0039	0.3062	0.0039	0.4077	0.0039	0.3727	0.0039	0.3601	0.0039	0.3830	0.0039	0.3897	0.0039	0.3985	0.0039	0.1382
0.0039	0.3013	0.0039	0.4073	0.0039	0.3732	0.0039	0.3617	0.0039	0.3837	0.0039	0.3905	0.0039	0.3993	0.0039	0.1275
0.0039	0.2963	0.0039	0.4068	0.0039	0.3738	0.0039	0.3633	0.0039	0.3844	0.0039	0.3913	0.0039	0.4001	0.0039	0.1173
0.0039	0.2913	0.0039	0.4063	0.0039	0.3743	0.0039	0.3651	0.0039	0.3852	0.0039	0.3922	0.0039	0.4010	0.0039	0.1076

Table: 10 Standard low-Re model data at heat flux of 23 kW/m^2

Position [0.0, 1.0, 0.0] (m)-0.8 m	Velocity: Component 0-0.8 m (m/s)	Position [0.0, 1.0, 0.0] (m)-1.0 m	Velocity: Component 0-1.0 m (m/s)	Position [0.0, 1.0, 0.0] (m)-1.2 m	Velocity: Component 0-1.2 m (m/s)	Position [0.0, 1.0, 0.0] (m)-1.4 m	Velocity: Component 0-1.4 m (m/s)	Position [0.0, 1.0, 0.0] (m)-1.6 m	Velocity: Component 0-1.6 m (m/s)	Position [0.0, 1.0, 0.0] (m)-1.8 m	Velocity: Component 0-1.8 m (m/s)	Position [0.0, 1.0, 0.0] (m)-2.0 m	Velocity: Component 0-2.0 m (m/s)	Position [0.0, 1.0, 0.0] (m)-0.01 m	Velocity: Component 0-0.01 m (m/s)
0.0039	0.0008	0.0035	0.3668	0.0001	0.3234	0.0001	0.3764	0.0039	0.0028	0.0039	0.0028	0.0039	0.0028	0.0039	0.0011
0.0039	0.0026	0.0035	0.3650	0.0002	0.3235	0.0002	0.3764	0.0039	0.0087	0.0039	0.0087	0.0039	0.0085	0.0039	0.0034
0.0039	0.0045	0.0036	0.3631	0.0003	0.3239	0.0003	0.3766	0.0039	0.0152	0.0039	0.0151	0.0039	0.0148	0.0039	0.0059
0.0039	0.0067	0.0036	0.3610	0.0004	0.3244	0.0004	0.3768	0.0039	0.0222	0.0039	0.0222	0.0039	0.0216	0.0039	0.0087
0.0039	0.0090	0.0036	0.3589	0.0005	0.3251	0.0005	0.3770	0.0039	0.0298	0.0039	0.0298	0.0039	0.0291	0.0039	0.0117
0.0039	0.0116	0.0037	0.3566	0.0006	0.3260	0.0006	0.3773	0.0039	0.0382	0.0039	0.0381	0.0039	0.0372	0.0039	0.0149
0.0039	0.0144	0.0037	0.3541	0.0007	0.3271	0.0007	0.3777	0.0039	0.0472	0.0039	0.0472	0.0039	0.0461	0.0039	0.0184
0.0039	0.0175	0.0037	0.3515	0.0008	0.3285	0.0008	0.3782	0.0039	0.0571	0.0039	0.0571	0.0039	0.0557	0.0039	0.0223
0.0039	0.0208	0.0037	0.3486	0.0009	0.3300	0.0009	0.3787	0.0039	0.0677	0.0039	0.0677	0.0039	0.0662	0.0039	0.0264
0.0039	0.0246	0.0037	0.3454	0.0010	0.3317	0.0010	0.3793	0.0039	0.0793	0.0039	0.0793	0.0039	0.0776	0.0039	0.0309
0.0039	0.0286	0.0037	0.3419	0.0011	0.3337	0.0011	0.3799	0.0039	0.0917	0.0039	0.0918	0.0039	0.0899	0.0039	0.0357
0.0039	0.0331	0.0038	0.3381	0.0012	0.3359	0.0012	0.3806	0.0039	0.1051	0.0039	0.1053	0.0039	0.1032	0.0039	0.0409
0.0039	0.0379	0.0038	0.3338	0.0013	0.3383	0.0013	0.3814	0.0039	0.1195	0.0039	0.1199	0.0039	0.1175	0.0039	0.0465
0.0039	0.0433	0.0038	0.3291	0.0014	0.3409	0.0014	0.3822	0.0039	0.1350	0.0039	0.1354	0.0039	0.1329	0.0039	0.0526

Table 11: Standard low-Re model data heat at flux of 30 kW/m^2

Position [0.0, 1.0, 0.0] (m)-0.8 m	Velocity: Component 0-0.8 m (m/s)	Position [0.0, 1.0, 0.0] (m)-1.0 m	Velocity: Component 0-1.0 m (m/s)	Position [0.0, 1.0, 0.0] (m)-1.2 m	Velocity: Component 0-1.2 m (m/s)	Position [0.0, 1.0, 0.0] (m)-1.4 m	Velocity: Component 0-1.4 m (m/s)	Position [0.0, 1.0, 0.0] (m)-1.6 m	Velocity: Component 0-1.6 m (m/s)	Position [0.0, 1.0, 0.0] (m)-1.8 m	Velocity: Component 0-1.8 m (m/s)	Position [0.0, 1.0, 0.0] (m)-2.0 m	Velocity: Component 0-2.0 m (m/s)	Position [0.0, 1.0, 0.0] (m)-0.01 m	Velocity: Component 0-0.01 m (m/s)
0.0039	0.0009	0.0035	0.4154	0.0001	0.3755	0.0001	0.3945	0.0039	0.0028	0.0039	0.0028	0.0039	0.0026	0.0039	0.0011
0.0039	0.0028	0.0035	0.4174	0.0002	0.3755	0.0002	0.3946	0.0039	0.0088	0.0039	0.0087	0.0039	0.0080	0.0039	0.0034
0.0039	0.0049	0.0036	0.4194	0.0003	0.3757	0.0003	0.3948	0.0039	0.0153	0.0039	0.0151	0.0039	0.0139	0.0039	0.0059
0.0039	0.0072	0.0036	0.4212	0.0004	0.3760	0.0004	0.3951	0.0039	0.0224	0.0039	0.0221	0.0039	0.0204	0.0039	0.0087
0.0039	0.0097	0.0036	0.4229	0.0005	0.3763	0.0005	0.3955	0.0039	0.0302	0.0039	0.0298	0.0039	0.0275	0.0039	0.0117
0.0039	0.0125	0.0037	0.4245	0.0006	0.3767	0.0006	0.3960	0.0039	0.0386	0.0039	0.0381	0.0039	0.0352	0.0039	0.0149
0.0039	0.0155	0.0037	0.4260	0.0007	0.3773	0.0007	0.3966	0.0039	0.0478	0.0039	0.0473	0.0039	0.0437	0.0039	0.0184
0.0039	0.0188	0.0037	0.4274	0.0008	0.3779	0.0008	0.3973	0.0039	0.0579	0.0039	0.0572	0.0039	0.0529	0.0039	0.0223
0.0039	0.0224	0.0037	0.4287	0.0009	0.3785	0.0009	0.3981	0.0039	0.0688	0.0039	0.0680	0.0039	0.0630	0.0039	0.0264
0.0039	0.0263	0.0037	0.4299	0.0010	0.3793	0.0010	0.3990	0.0039	0.0806	0.0039	0.0798	0.0039	0.0740	0.0039	0.0309
0.0039	0.0306	0.0037	0.4310	0.0011	0.3802	0.0011	0.4000	0.0039	0.0935	0.0039	0.0926	0.0039	0.0860	0.0039	0.0357
0.0039	0.0353	0.0038	0.4321	0.0012	0.3811	0.0012	0.4011	0.0039	0.1074	0.0039	0.1065	0.0039	0.0990	0.0039	0.0409
0.0039	0.0404	0.0038	0.4330	0.0013	0.3821	0.0013	0.4023	0.0039	0.1224	0.0039	0.1214	0.0039	0.1131	0.0039	0.0465
0.0039	0.0460	0.0038	0.4338	0.0014	0.3832	0.0014	0.4036	0.0039	0.1386	0.0039	0.1376	0.0039	0.1285	0.0039	0.0526

Table 12: Standard low-Re model data heat at flux of 40 kW/m^2

Position [0.0, 1.0, 0.0] (m)-0.8 m	Velocity: Component 0-0.8 m (m/s)	Position [0.0, 1.0, 0.0] (m)-1.0 m	Velocity: Component 0-1.0 m (m/s)	Position [0.0, 1.0, 0.0] (m)-1.2 m	Velocity: Component 0-1.2 m (m/s)	Position [0.0, 1.0, 0.0] (m)-1.4 m	Velocity: Component 0-1.4 m (m/s)	Position [0.0, 1.0, 0.0] (m)-1.6 m	Velocity: Component 0-1.6 m (m/s)	Position [0.0, 1.0, 0.0] (m)-1.8 m	Velocity: Component 0-1.8 m (m/s)	Position [0.0, 1.0, 0.0] (m)-2.0 m	Velocity: Component 0-2.0 m (m/s)	Position [0.0, 1.0, 0.0] (m)-0.01 m	Velocity: Component 0-0.01 m (m/s)
0.0039	0.0009	0.0035	0.4154	0.0039	0.3755	0.0039	0.3945	0.0039	0.0028	0.0039	0.0028	0.0039	0.0026	0.0039	0.0011
0.0039	0.0028	0.0035	0.4174	0.0039	0.3755	0.0039	0.3946	0.0039	0.0088	0.0039	0.0087	0.0039	0.0080	0.0039	0.0034
0.0039	0.0049	0.0036	0.4194	0.0039	0.3757	0.0039	0.3948	0.0039	0.0153	0.0039	0.0151	0.0039	0.0139	0.0039	0.0059
0.0039	0.0072	0.0036	0.4212	0.0039	0.3760	0.0039	0.3951	0.0039	0.0224	0.0039	0.0221	0.0039	0.0204	0.0039	0.0087
0.0039	0.0097	0.0036	0.4229	0.0039	0.3763	0.0039	0.3955	0.0039	0.0302	0.0039	0.0298	0.0039	0.0275	0.0039	0.0117
0.0039	0.0125	0.0037	0.4245	0.0039	0.3767	0.0039	0.3960	0.0039	0.0386	0.0039	0.0381	0.0039	0.0352	0.0039	0.0149
0.0039	0.0155	0.0037	0.4260	0.0039	0.3773	0.0039	0.3966	0.0039	0.0478	0.0039	0.0473	0.0039	0.0437	0.0039	0.0184
0.0039	0.0188	0.0037	0.4274	0.0039	0.3779	0.0039	0.3973	0.0039	0.0579	0.0039	0.0572	0.0039	0.0529	0.0039	0.0223
0.0039	0.0224	0.0037	0.4287	0.0039	0.3785	0.0039	0.3981	0.0039	0.0688	0.0039	0.0680	0.0039	0.0630	0.0039	0.0264
0.0039	0.0263	0.0037	0.4299	0.0039	0.3793	0.0039	0.3990	0.0039	0.0806	0.0039	0.0798	0.0039	0.0740	0.0039	0.0309
0.0039	0.0306	0.0037	0.4310	0.0039	0.3802	0.0039	0.4000	0.0039	0.0935	0.0039	0.0926	0.0039	0.0860	0.0039	0.0357
0.0039	0.0353	0.0038	0.4321	0.0039	0.3811	0.0039	0.4011	0.0039	0.1074	0.0039	0.1065	0.0039	0.0990	0.0039	0.0409
0.0039	0.0404	0.0038	0.4330	0.0039	0.3821	0.0039	0.4023	0.0039	0.1224	0.0039	0.1214	0.0039	0.1131	0.0039	0.0465
0.0039	0.0460	0.0038	0.4338	0.0039	0.3832	0.0039	0.4036	0.0039	0.1386	0.0039	0.1376	0.0039	0.1285	0.0039	0.0526
0.0039	0.0520	0.0038	0.4344	0.0039	0.3844	0.0039	0.4049	0.0039	0.1559	0.0039	0.1551	0.0039	0.1451	0.0039	0.0590

I-4 V2F model simulation results data

Table 13: V2F model data at heat flux of 20 kW/m^2

Position [0.0, 1.0, 0.0] (m)-0.8 m	Velocity: Component 0-0.8 m (m/s)	Position [0.0, 1.0, 0.0] (m)-1.0 m	Velocity: Component 0-1.0 m (m/s)	Position [0.0, 1.0, 0.0] (m)-1.2 m	Velocity: Component 0-1.2 m (m/s)	Position [0.0, 1.0, 0.0] (m)-1.4 m	Velocity: Component 0-1.4 m (m/s)	Position [0.0, 1.0, 0.0] (m)-1.6 m	Velocity: Component 0-1.6 m (m/s)	Position [0.0, 1.0, 0.0] (m)-1.8 m	Velocity: Component 0-1.8 m (m/s)	Position [0.0, 1.0, 0.0] (m)-2.0 m	Velocity: Component 0-2.0 m (m/s)	Position [0.0, 1.0, 0.0] (m)-0.01 m	Velocity: Component 0-0.01 m (m/s)
0.0039	0.4681	0.0039	0.4412	0.0039	0.3600	0.0039	0.2976	0.0039	0.3826	0.0039	0.3759	0.0001	0.3984	0.0038	0.2602
0.0039	0.4680	0.0039	0.4411	0.0039	0.3600	0.0039	0.2980	0.0039	0.3826	0.0039	0.3760	0.0002	0.3985	0.0038	0.2480
0.0039	0.4676	0.0039	0.4407	0.0039	0.3601	0.0039	0.2989	0.0039	0.3827	0.0039	0.3762	0.0003	0.3986	0.0038	0.2355
0.0039	0.4671	0.0039	0.4402	0.0039	0.3602	0.0039	0.3002	0.0039	0.3829	0.0039	0.3765	0.0004	0.3988	0.0038	0.2230
0.0039	0.4665	0.0039	0.4394	0.0039	0.3603	0.0039	0.3019	0.0039	0.3831	0.0039	0.3769	0.0005	0.3991	0.0038	0.2105
0.0039	0.4656	0.0039	0.4385	0.0039	0.3605	0.0039	0.3040	0.0039	0.3833	0.0039	0.3774	0.0006	0.3994	0.0038	0.1981
0.0039	0.4646	0.0039	0.4372	0.0039	0.3607	0.0039	0.3065	0.0039	0.3836	0.0039	0.3780	0.0007	0.3999	0.0039	0.1858
0.0039	0.4631	0.0039	0.4354	0.0039	0.3611	0.0039	0.3094	0.0039	0.3839	0.0039	0.3787	0.0008	0.4003	0.0039	0.1738
0.0039	0.3102	0.0039	0.4333	0.0039	0.3617	0.0039	0.3127	0.0039	0.3843	0.0039	0.3796	0.0009	0.4009	0.0039	0.1620
0.0039	0.3048	0.0039	0.4311	0.0039	0.3625	0.0039	0.3163	0.0039	0.3847	0.0039	0.3805	0.0010	0.4015	0.0039	0.1506
0.0039	0.2993	0.0039	0.4287	0.0039	0.3634	0.0039	0.3203	0.0039	0.3852	0.0039	0.3815	0.0011	0.4022	0.0039	0.1395
0.0039	0.2936	0.0039	0.4262	0.0039	0.3645	0.0039	0.3245	0.0039	0.3857	0.0039	0.3826	0.0012	0.4030	0.0039	0.1288
0.0039	0.2878	0.0039	0.4238	0.0039	0.3657	0.0039	0.3289	0.0039	0.3863	0.0039	0.3838	0.0013	0.4039	0.0039	0.1186
0.0039	0.2818	0.0039	0.4213	0.0039	0.3670	0.0039	0.3336	0.0039	0.3869	0.0039	0.3852	0.0014	0.4049	0.0039	0.1088
0.0039	0.2756	0.0039	0.4187	0.0039	0.3685	0.0039	0.3384	0.0039	0.3876	0.0039	0.3867	0.0015	0.4059	0.0039	0.0994

Table 14: V2F model data at heat flux of 23 kW/m^2

Position [0.0, 1.0, 0.0] (m)-0.8 m	Velocity: Component 0-0.8 m (m/s)	Position [0.0, 1.0, 0.0] (m)-1.0 m	Velocity: Component 0-1.0 m (m/s)	Position [0.0, 1.0, 0.0] (m)-1.2 m	Velocity: Component 0-1.2 m (m/s)	Position [0.0, 1.0, 0.0] (m)-1.4 m	Velocity: Component 0-1.4 m (m/s)	Position [0.0, 1.0, 0.0] (m)-1.6 m	Velocity: Component 0-1.6 m (m/s)	Position [0.0, 1.0, 0.0] (m)-1.8 m	Velocity: Component 0-1.8 m (m/s)	Position [0.0, 1.0, 0.0] (m)-2.0 m	Velocity: Component 0-2.0 m (m/s)	Position [0.0, 1.0, 0.0] (m)-0.01 m	Velocity: Component 0-0.01 m (m/s)
0.0039	0.4681	0.0039	0.4412	0.0039	0.3600	0.0039	0.2976	0.0039	0.3826	0.0039	0.3759	0.0039	0.3984	0.0038	0.2602
0.0039	0.4680	0.0039	0.4411	0.0039	0.3600	0.0039	0.2980	0.0039	0.3826	0.0039	0.3760	0.0039	0.3985	0.0038	0.2480
0.0039	0.4676	0.0039	0.4407	0.0039	0.3601	0.0039	0.2989	0.0039	0.3827	0.0039	0.3762	0.0039	0.3986	0.0038	0.2355
0.0039	0.4671	0.0039	0.4402	0.0039	0.3602	0.0039	0.3002	0.0039	0.3829	0.0039	0.3765	0.0039	0.3988	0.0038	0.2230
0.0039	0.4665	0.0039	0.4394	0.0039	0.3603	0.0039	0.3019	0.0039	0.3831	0.0039	0.3769	0.0039	0.3991	0.0038	0.2105
0.0039	0.4656	0.0039	0.4385	0.0039	0.3605	0.0039	0.3040	0.0039	0.3833	0.0039	0.3774	0.0039	0.3994	0.0038	0.1981
0.0039	0.4646	0.0039	0.4372	0.0039	0.3607	0.0039	0.3065	0.0039	0.3836	0.0039	0.3780	0.0039	0.3999	0.0039	0.1858
0.0039	0.4631	0.0039	0.4354	0.0039	0.3611	0.0039	0.3094	0.0039	0.3839	0.0039	0.3787	0.0039	0.4003	0.0039	0.1738
0.0039	0.3102	0.0039	0.4333	0.0039	0.3617	0.0039	0.3127	0.0039	0.3843	0.0039	0.3796	0.0039	0.4009	0.0039	0.1620
0.0039	0.3048	0.0039	0.4311	0.0039	0.3625	0.0039	0.3163	0.0039	0.3847	0.0039	0.3805	0.0039	0.4015	0.0039	0.1506
0.0039	0.2993	0.0039	0.4287	0.0039	0.3634	0.0039	0.3203	0.0039	0.3852	0.0039	0.3815	0.0039	0.4022	0.0039	0.1395
0.0039	0.2936	0.0039	0.4262	0.0039	0.3645	0.0039	0.3245	0.0039	0.3857	0.0039	0.3826	0.0039	0.4030	0.0039	0.1288
0.0039	0.2878	0.0039	0.4238	0.0039	0.3657	0.0039	0.3289	0.0039	0.3863	0.0039	0.3838	0.0039	0.4039	0.0039	0.1186
0.0039	0.2818	0.0039	0.4213	0.0039	0.3670	0.0039	0.3336	0.0039	0.3869	0.0039	0.3852	0.0039	0.4049	0.0039	0.1088
0.0039	0.2756	0.0039	0.4187	0.0039	0.3685	0.0039	0.3384	0.0039	0.3876	0.0039	0.3867	0.0039	0.4059	0.0039	0.0994

Table 15: V2F model data at heat flux of 30 kW/m^2

Position [0.0, 1.0, 0.0] (m)-0.8 m	Velocity: Component 0-0.8 m (m/s)	Position [0.0, 1.0, 0.0] (m)-1.0 m	Velocity: Component 0-1.0 m (m/s)	Position [0.0, 1.0, 0.0] (m)-1.2 m	Velocity: Component 0-1.2 m (m/s)	Position [0.0, 1.0, 0.0] (m)-1.4 m	Velocity: Component 0-1.4 m (m/s)	Position [0.0, 1.0, 0.0] (m)-1.6 m	Velocity: Component 0-1.6 m (m/s)	Position [0.0, 1.0, 0.0] (m)-1.8 m	Velocity: Component 0-1.8 m (m/s)	Position [0.0, 1.0, 0.0] (m)-2.0 m	Velocity: Component 0-2.0 m (m/s)	Position [0.0, 1.0, 0.0] (m)-0.01 m	Velocity: Component 0-0.01 m (m/s)
0.0039	0.0008	0.0035	0.3876	0.0039	0.3011	0.0039	0.3765	0.0039	0.0029	0.0039	0.0029	0.0039	0.0027	0.0039	0.0011
0.0039	0.0025	0.0035	0.3898	0.0039	0.3017	0.0039	0.3766	0.0039	0.0089	0.0039	0.0088	0.0039	0.0085	0.0039	0.0035
0.0039	0.0044	0.0036	0.3922	0.0039	0.3029	0.0039	0.3767	0.0039	0.0154	0.0039	0.0154	0.0039	0.0147	0.0039	0.0060
0.0039	0.0065	0.0036	0.3948	0.0039	0.3047	0.0039	0.3769	0.0039	0.0226	0.0039	0.0225	0.0039	0.0215	0.0039	0.0088
0.0039	0.0088	0.0036	0.3977	0.0039	0.3070	0.0039	0.3772	0.0039	0.0304	0.0039	0.0303	0.0039	0.0290	0.0039	0.0118
0.0039	0.0113	0.0037	0.4009	0.0039	0.3098	0.0039	0.3776	0.0039	0.0389	0.0039	0.0388	0.0039	0.0371	0.0039	0.0151
0.0039	0.0140	0.0037	0.4043	0.0039	0.3130	0.0039	0.3780	0.0039	0.0481	0.0039	0.0480	0.0039	0.0460	0.0039	0.0187
0.0039	0.0170	0.0037	0.4081	0.0039	0.3166	0.0039	0.3785	0.0039	0.0582	0.0039	0.0581	0.0039	0.0557	0.0039	0.0226
0.0039	0.0203	0.0037	0.4121	0.0039	0.3204	0.0039	0.3792	0.0039	0.0691	0.0039	0.0690	0.0039	0.0662	0.0039	0.0268
0.0039	0.0239	0.0037	0.4163	0.0039	0.3245	0.0039	0.3798	0.0039	0.0809	0.0039	0.0808	0.0039	0.0776	0.0039	0.0313
0.0039	0.0278	0.0037	0.4207	0.0039	0.3287	0.0039	0.3806	0.0039	0.0937	0.0039	0.0936	0.0039	0.0900	0.0039	0.0362
0.0039	0.0321	0.0038	0.4251	0.0039	0.3329	0.0039	0.3815	0.0039	0.1074	0.0039	0.1075	0.0039	0.1034	0.0039	0.0415
0.0039	0.0367	0.0038	0.4296	0.0039	0.3373	0.0039	0.3824	0.0039	0.1223	0.0039	0.1224	0.0039	0.1179	0.0039	0.0472
0.0039	0.0418	0.0038	0.4339	0.0039	0.3416	0.0039	0.3835	0.0039	0.1383	0.0039	0.1384	0.0039	0.1335	0.0039	0.0533
0.0039	0.0473	0.0038	0.4379	0.0039	0.3460	0.0039	0.3846	0.0039	0.1553	0.0039	0.1556	0.0039	0.1503	0.0039	0.0598

Table 16: V2F model data at heat flux of 40 kW/m^2

Position [0.0, 1.0, 0.0] (m)-0.8 m	Velocity: Component 0-0.8 m (m/s)	Position [0.0, 1.0, 0.0] (m)-1.0 m	Velocity: Component 0-1.0 m (m/s)	Position [0.0, 1.0, 0.0] (m)-1.2 m	Velocity: Component 0-1.2 m (m/s)	Position [0.0, 1.0, 0.0] (m)-1.4 m	Velocity: Component 0-1.4 m (m/s)	Position [0.0, 1.0, 0.0] (m)-1.6 m	Velocity: Component 0-1.6 m (m/s)	Position [0.0, 1.0, 0.0] (m)-1.8 m	Velocity: Component 0-1.8 m (m/s)	Position [0.0, 1.0, 0.0] (m)-2.0 m	Velocity: Component 0-2.0 m (m/s)	Position [0.0, 1.0, 0.0] (m)-0.01 m	Velocity: Component 0-0.01 m (m/s)
0.0039	0.0009	0.0035	0.4208	0.0001	0.3583	0.0001	0.3912	0.0039	0.0029	0.0039	0.0029	0.0039	0.0027	0.0039	0.0011
0.0039	0.0027	0.0035	0.4252	0.0002	0.3584	0.0002	0.3912	0.0039	0.0089	0.0039	0.0088	0.0039	0.0082	0.0039	0.0035
0.0039	0.0046	0.0036	0.4295	0.0003	0.3586	0.0003	0.3914	0.0039	0.0155	0.0039	0.0153	0.0039	0.0143	0.0039	0.0060
0.0039	0.0068	0.0036	0.4336	0.0004	0.3590	0.0004	0.3917	0.0039	0.0227	0.0039	0.0225	0.0039	0.0210	0.0039	0.0088
0.0039	0.0092	0.0036	0.4375	0.0005	0.3595	0.0005	0.3920	0.0039	0.0306	0.0039	0.0302	0.0039	0.0283	0.0039	0.0118
0.0039	0.0118	0.0037	0.4411	0.0006	0.3602	0.0006	0.3925	0.0039	0.0392	0.0039	0.0387	0.0039	0.0363	0.0039	0.0151
0.0039	0.0146	0.0037	0.4444	0.0007	0.3610	0.0007	0.3930	0.0039	0.0485	0.0039	0.0480	0.0039	0.0450	0.0039	0.0187
0.0039	0.0177	0.0037	0.4475	0.0008	0.3619	0.0008	0.3937	0.0039	0.0587	0.0039	0.0581	0.0039	0.0545	0.0039	0.0226
0.0039	0.0211	0.0037	0.4503	0.0009	0.3630	0.0009	0.3944	0.0039	0.0698	0.0039	0.0691	0.0039	0.0649	0.0039	0.0268
0.0039	0.0248	0.0037	0.4529	0.0010	0.3642	0.0010	0.3952	0.0039	0.0818	0.0039	0.0811	0.0039	0.0763	0.0039	0.0313
0.0039	0.0289	0.0037	0.4551	0.0011	0.3655	0.0011	0.3961	0.0039	0.0949	0.0039	0.0940	0.0039	0.0886	0.0039	0.0362
0.0039	0.0333	0.0038	0.4571	0.0012	0.3670	0.0012	0.3971	0.0039	0.1090	0.0039	0.1081	0.0039	0.1020	0.0039	0.0415
0.0039	0.0381	0.0038	0.4587	0.0013	0.3686	0.0013	0.3982	0.0039	0.1242	0.0039	0.1233	0.0039	0.1166	0.0039	0.0472
0.0039	0.0433	0.0038	0.4601	0.0014	0.3704	0.0014	0.3993	0.0039	0.1406	0.0039	0.1398	0.0039	0.1324	0.0039	0.0533
0.0039	0.0489	0.0038	0.4611	0.0015	0.3722	0.0015	0.4006	0.0039	0.1582	0.0039	0.1575	0.0039	0.1495	0.0039	0.0598

APENDIX II: Radial density data at different axial distances and heat fluxes

II-1 AKN model simulation result data

Table 17: AKN model data for density at heat flux of 20 kW/m^2

Position [0.0, 1.0, 0.0] (m)-0.8 m	Density-0.8 m (kg/m^3)	Position [0.0, 1.0, 0.0] (m)-1.0 m	Density-1.0 m (kg/m^3)	Position [0.0, 1.0, 0.0] (m)-1.2 m	Density-1.2 m (kg/m^3)	Position [0.0, 1.0, 0.0] (m)-1.4 m	Density-1.4 m (kg/m^3)	Position [0.0, 1.0, 0.0] (m)-1.6 m	Density-1.6 m (kg/m^3)	Position [0.0, 1.0, 0.0] (m)-1.8 m	Density-1.8 m (kg/m^3)	Position [0.0, 1.0, 0.0] (m)-2.0 m	Density-2.0 m (kg/m^3)	Position [0.0, 1.0, 0.0] (m)-0.01 m	Density-0.01 m (kg/m^3)
0.0039	868.4071	0.0039	862.3625	0.0039	853.6688	0.0039	844.5688	0.0039	804.2379	0.0039	786.1609	0.0039	762.4382	0.0038	868.4073
0.0039	868.4071	0.0039	862.3471	0.0039	853.6498	0.0039	844.4349	0.0039	804.2265	0.0039	786.1381	0.0039	762.4213	0.0038	868.4073
0.0039	868.4071	0.0039	862.3132	0.0039	853.6080	0.0039	844.1439	0.0039	804.2009	0.0039	786.0880	0.0039	762.3840	0.0038	868.4073
0.0039	868.4071	0.0039	862.2617	0.0039	853.5438	0.0039	843.7121	0.0039	804.1623	0.0039	786.0114	0.0039	762.3265	0.0038	868.4073
0.0039	868.4071	0.0039	862.1918	0.0039	853.4570	0.0039	843.1545	0.0039	804.1105	0.0039	785.9096	0.0039	762.2485	0.0038	868.4073
0.0039	868.4071	0.0039	862.1040	0.0039	853.3474	0.0039	842.4866	0.0039	804.0453	0.0039	785.7825	0.0039	762.1505	0.0038	868.4073
0.0039	868.4071	0.0039	861.9972	0.0039	853.2137	0.0039	841.7220	0.0039	803.9669	0.0039	785.6299	0.0039	762.0314	0.0039	868.4073
0.0039	868.4071	0.0039	861.8710	0.0039	853.0554	0.0039	840.8646	0.0039	803.8748	0.0039	785.4521	0.0039	761.8914	0.0039	868.4073
0.0039	868.0302	0.0039	861.7247	0.0039	852.8708	0.0039	839.9086	0.0039	803.7694	0.0039	785.2495	0.0039	761.7302	0.0039	868.4073
0.0039	867.9606	0.0039	861.5576	0.0039	852.6588	0.0039	838.8592	0.0039	803.6500	0.0039	785.0219	0.0039	761.5476	0.0039	868.4073
0.0039	867.8823	0.0039	861.3683	0.0039	852.4174	0.0039	837.7344	0.0039	803.5166	0.0039	784.7700	0.0039	761.3434	0.0039	868.4073
0.0039	867.7940	0.0039	861.1556	0.0039	852.1445	0.0039	836.5553	0.0039	803.3688	0.0039	784.4932	0.0039	761.1171	0.0039	868.4073
0.0039	867.6950	0.0039	860.9183	0.0039	851.8377	0.0039	835.3395	0.0039	803.2061	0.0039	784.1918	0.0039	760.8686	0.0039	868.4073
0.0039	867.5846	0.0039	860.6547	0.0039	851.4938	0.0039	834.0995	0.0039	803.0286	0.0039	783.8660	0.0039	760.5975	0.0039	868.4073
0.0039	867.4613	0.0039	860.3630	0.0039	851.1097	0.0039	832.8447	0.0039	802.8350	0.0039	783.5150	0.0039	760.3031	0.0039	868.4073

Table 18: AKN model data for density at heat flux of 30 kW/m^2

Position [0.0, 1.0, 0.0] (m)-0.8 m	Density-0.8 m (kg/m^3)	Position [0.0, 1.0, 0.0] (m)-1.0 m	Density-1.0 m (kg/m^3)	Position [0.0, 1.0, 0.0] (m)-1.2 m	Density-1.2 m (kg/m^3)	Position [0.0, 1.0, 0.0] (m)-1.4 m	Density-1.4 m (kg/m^3)	Position [0.0, 1.0, 0.0] (m)-1.6 m	Density-1.6 m (kg/m^3)	Position [0.0, 1.0, 0.0] (m)-1.8 m	Density-1.8 m (kg/m^3)	Position [0.0, 1.0, 0.0] (m)-2.0 m	Density-2.0 m (kg/m^3)	Position [0.0, 1.0, 0.0] (m)-0.01 m	Density-0.01 m (kg/m^3)
0.0039	816.0386	0.0035	832.0316	0.0001	830.9107	0.0001	799.1793	0.0039	150.8146	0.0039	148.5333	0.0039	146.4386	0.0039	868.4073
0.0039	816.6332	0.0035	829.0297	0.0002	830.8705	0.0002	799.1590	0.0039	151.1276	0.0039	148.7974	0.0039	146.6649	0.0039	868.4073
0.0039	817.2845	0.0036	825.9344	0.0003	830.7825	0.0003	799.1140	0.0039	151.4801	0.0039	149.0942	0.0039	146.9180	0.0039	868.4073
0.0039	817.9973	0.0036	822.7302	0.0004	830.6499	0.0004	799.0452	0.0039	151.8781	0.0039	149.4286	0.0039	147.2017	0.0039	868.4073
0.0039	818.7765	0.0036	819.3947	0.0005	830.4749	0.0005	798.9531	0.0039	152.3284	0.0039	149.8063	0.0039	147.5205	0.0039	868.4073
0.0039	819.6276	0.0037	815.8998	0.0006	830.2590	0.0006	798.8372	0.0039	152.8396	0.0039	150.2342	0.0039	147.8801	0.0039	868.4073
0.0039	820.5565	0.0037	812.2111	0.0007	830.0038	0.0007	798.6974	0.0039	153.4216	0.0039	150.7208	0.0039	148.2871	0.0039	868.4073
0.0039	821.5695	0.0037	808.2769	0.0008	829.7116	0.0008	798.5333	0.0039	154.0867	0.0039	151.2760	0.0039	148.7496	0.0039	868.4073
0.0039	822.6727	0.0037	804.0271	0.0009	829.3839	0.0009	798.3444	0.0039	154.8497	0.0039	151.9123	0.0039	149.2776	0.0039	868.4073
0.0039	823.8724	0.0037	799.3691	0.0010	829.0228	0.0010	798.1306	0.0039	155.7284	0.0039	152.6448	0.0039	149.8833	0.0039	868.4073
0.0039	825.1757	0.0037	794.1768	0.0011	828.6298	0.0011	797.8909	0.0039	156.7449	0.0039	153.4922	0.0039	150.5820	0.0039	868.4073
0.0039	826.5891	0.0038	788.2720	0.0012	828.2060	0.0012	797.6247	0.0039	157.9259	0.0039	154.4778	0.0039	151.3928	0.0039	868.4073
0.0039	828.1190	0.0038	781.4006	0.0013	827.7529	0.0013	797.3315	0.0039	159.3046	0.0039	155.6301	0.0039	152.3395	0.0039	868.4073
0.0039	829.7717	0.0038	773.1890	0.0014	827.2709	0.0014	797.0099	0.0039	160.9216	0.0039	156.9848	0.0039	153.4525	0.0039	868.4073
0.0039	831.5531	0.0038	763.0800	0.0015	826.7610	0.0015	796.6592	0.0039	162.8272	0.0039	158.5866	0.0039	154.7698	0.0039	868.4073

II-2 EB mode simulation results data

Table 19: EB model data for density at heat flux of 20 kW/m^2

Position [0.0, 1.0, 0.0] (m)-0.8 m	Density-0.8 m (kg/m^3)	Position [0.0, 1.0, 0.0] (m)-1.0 m	Density-1.0 m (kg/m^3)	Position [0.0, 1.0, 0.0] (m)-1.2 m	Density-1.2 m (kg/m^3)	Position [0.0, 1.0, 0.0] (m)-1.4 m	Density-1.4 m (kg/m^3)	Position [0.0, 1.0, 0.0] (m)-1.6 m	Density-1.6 m (kg/m^3)	Position [0.0, 1.0, 0.0] (m)-1.8 m	Density-1.8 m (kg/m^3)	Position [0.0, 1.0, 0.0] (m)-2.0 m	Density-2.0 m (kg/m^3)	Position [0.0, 1.0, 0.0] (m)-0.01 m	Density-0.01 m (kg/m^3)
0.0039	868.4073	0.0039	861.6011	0.0039	851.4882	0.0001	838.1832	0.0001	806.7712	0.0039	786.3462	0.0039	763.6329	0.0038	868.4073
0.0039	868.4073	0.0039	861.5873	0.0039	851.4691	0.0002	838.1306	0.0002	806.7554	0.0039	786.3271	0.0039	763.6169	0.0038	868.4073
0.0039	868.4073	0.0039	861.5569	0.0039	851.4268	0.0003	838.0148	0.0003	806.7203	0.0039	786.2848	0.0039	763.5806	0.0038	868.4073
0.0039	868.4073	0.0039	861.5103	0.0039	851.3622	0.0004	837.8383	0.0004	806.6671	0.0039	786.2207	0.0039	763.5248	0.0038	868.4073
0.0039	868.4073	0.0039	861.4475	0.0039	851.2749	0.0005	837.6017	0.0005	806.5955	0.0039	786.1347	0.0039	763.4493	0.0038	868.4073
0.0039	868.4073	0.0039	861.3683	0.0039	851.1642	0.0006	837.3060	0.0006	806.5056	0.0039	786.0265	0.0039	763.3536	0.0038	868.4073
0.0039	868.4073	0.0039	861.2720	0.0039	851.0294	0.0007	836.9527	0.0007	806.3971	0.0039	785.8963	0.0039	763.2370	0.0039	868.4073
0.0039	868.4073	0.0039	861.1580	0.0039	850.8691	0.0008	836.5448	0.0008	806.2693	0.0039	785.7438	0.0039	763.0996	0.0039	868.4073
0.0039	868.0402	0.0039	861.0259	0.0039	850.6820	0.0009	836.0849	0.0009	806.1225	0.0039	785.5686	0.0039	762.9405	0.0039	868.4073
0.0039	867.9709	0.0039	860.8744	0.0039	850.4663	0.0010	835.5766	0.0010	805.9557	0.0039	785.3702	0.0039	762.7589	0.0039	868.4073
0.0039	867.8925	0.0039	860.7031	0.0039	850.2199	0.0011	835.0228	0.0011	805.7682	0.0039	785.1486	0.0039	762.5546	0.0039	868.4073
0.0039	867.8038	0.0039	860.5103	0.0039	849.9408	0.0012	834.4254	0.0012	805.5598	0.0039	784.9030	0.0039	762.3265	0.0039	868.4073
0.0039	867.7039	0.0039	860.2950	0.0039	849.6260	0.0013	833.7856	0.0013	805.3290	0.0039	784.6326	0.0039	762.0736	0.0039	868.4073
0.0039	867.5919	0.0039	860.0554	0.0039	849.2722	0.0014	833.1043	0.0014	805.0756	0.0039	784.3367	0.0039	761.7950	0.0039	868.4073
0.0039	867.4663	0.0039	859.7896	0.0039	848.8754	0.0015	832.3807	0.0015	804.7975	0.0039	784.0135	0.0039	761.4894	0.0039	868.4073

Table 20: EB model data for density at heat flux of 30 kW/m^2

Position [0.0, 1.0, 0.0] (m)-0.8 m	Density-0.8 m (kg/m^3)	Position [0.0, 1.0, 0.0] (m)-1.0 m	Density-1.0 m (kg/m^3)	Position [0.0, 1.0, 0.0] (m)-1.2 m	Density-1.2 m (kg/m^3)	Position [0.0, 1.0, 0.0] (m)-1.4 m	Density-1.4 m (kg/m^3)	Position [0.0, 1.0, 0.0] (m)-1.6 m	Density-1.6 m (kg/m^3)	Position [0.0, 1.0, 0.0] (m)-1.8 m	Density-1.8 m (kg/m^3)	Position [0.0, 1.0, 0.0] (m)-2.0 m	Density-2.0 m (kg/m^3)	Position [0.0, 1.0, 0.0] (m)-0.01 m	Density-0.01 m (kg/m^3)
0.0039	816.3332	0.0035	837.6431	0.0001	832.4799	0.0001	800.6833	0.0039	150.5665	0.0039	147.8380	0.0039	145.2818	0.0039	868.4071
0.0039	816.9275	0.0035	835.2264	0.0002	832.4489	0.0002	800.6600	0.0039	150.8740	0.0039	148.0885	0.0039	145.4926	0.0039	868.4071
0.0039	817.5781	0.0036	832.5146	0.0003	832.3804	0.0003	800.6085	0.0039	151.2202	0.0039	148.3697	0.0039	145.7272	0.0039	868.4073
0.0039	818.2907	0.0036	829.4653	0.0004	832.2767	0.0004	800.5304	0.0039	151.6111	0.0039	148.6861	0.0039	145.9892	0.0039	868.4073
0.0039	819.0702	0.0036	826.0310	0.0005	832.1381	0.0005	800.4255	0.0039	152.0534	0.0039	149.0432	0.0039	146.2824	0.0039	868.4073
0.0039	819.9221	0.0037	822.1567	0.0006	831.9649	0.0006	800.2939	0.0039	152.5556	0.0039	149.4474	0.0039	146.6116	0.0039	868.4073
0.0039	820.8525	0.0037	817.7805	0.0007	831.7575	0.0007	800.1350	0.0039	153.1277	0.0039	149.9066	0.0039	146.9824	0.0039	868.4073
0.0039	821.8676	0.0037	812.8298	0.0008	831.5163	0.0008	799.9488	0.0039	153.7818	0.0039	150.4305	0.0039	147.4020	0.0039	868.4073
0.0039	822.9736	0.0037	807.2152	0.0009	831.2410	0.0009	799.7346	0.0039	154.5325	0.0039	151.0307	0.0039	147.8791	0.0039	868.4073
0.0039	824.1765	0.0037	800.8229	0.0010	830.9319	0.0010	799.4923	0.0039	155.3978	0.0039	151.7217	0.0039	148.4243	0.0039	868.4073
0.0039	825.4824	0.0037	793.5114	0.0011	830.5887	0.0011	799.2208	0.0039	156.3997	0.0039	152.5213	0.0039	149.0512	0.0039	868.4073
0.0039	826.8970	0.0038	785.0978	0.0012	830.2112	0.0012	798.9197	0.0039	157.5652	0.0039	153.4519	0.0039	149.7769	0.0039	868.4073
0.0039	828.4250	0.0038	775.3483	0.0013	829.7982	0.0013	798.5880	0.0039	158.9280	0.0039	154.5413	0.0039	150.6229	0.0039	868.4073
0.0039	830.0698	0.0038	763.9442	0.0014	829.3495	0.0014	798.2243	0.0039	160.5295	0.0039	155.8246	0.0039	151.6168	0.0039	868.4073
0.0039	831.8328	0.0038	750.4019	0.0015	828.8638	0.0015	797.8270	0.0039	162.4216	0.0039	157.3459	0.0039	152.7942	0.0039	868.4073
0.0039	833.7126	0.0038	733.8808	0.0016	828.3397	0.0016	797.3946	0.0039	164.6688	0.0039	159.1613	0.0039	154.2005	0.0039	868.4073
0.0039	835.7032	0.0038	712.7719	0.0017	827.7753	0.0017	796.9249	0.0039	167.3518	0.0039	161.3416	0.0039	155.8946	0.0039	868.4073

II-3 Standard low-Re model simulation results

Table 21: Standard low-Re model data for density at heat flux of 20 kW/m^2

Position [0.0, 1.0, 0.0] (m)-0.8 m	Density-0.8 m (kg/m^3)	Position [0.0, 1.0, 0.0] (m)-1.0 m	Density-1.0 m (kg/m^3)	Position [0.0, 1.0, 0.0] (m)-1.2 m	Density-1.2 m (kg/m^3)	Position [0.0, 1.0, 0.0] (m)-1.4 m	Density-1.4 m (kg/m^3)	Position [0.0, 1.0, 0.0] (m)-1.6 m	Density-1.6 m (kg/m^3)	Position [0.0, 1.0, 0.0] (m)-1.8 m	Density-1.8 m (kg/m^3)	Position [0.0, 1.0, 0.0] (m)-2.0 m	Density-2.0 m (kg/m^3)	Position [0.0, 1.0, 0.0] (m)-0.01 m	Density-0.01 m (kg/m^3)
0.0039	868.4073	0.0039	861.5627	0.0039	852.0599	0.0039	833.1541	0.0039	811.9954	0.0001	795.6461	0.0039	780.1360	0.0038	868.4073
0.0039	868.4073	0.0039	861.5491	0.0039	852.0426	0.0039	833.1232	0.0039	811.9797	0.0002	795.6279	0.0039	780.1198	0.0038	868.4073
0.0039	868.4073	0.0039	861.5192	0.0039	852.0043	0.0039	833.0558	0.0039	811.9447	0.0003	795.5881	0.0039	780.0845	0.0038	868.4073
0.0039	868.4073	0.0039	861.4738	0.0039	851.9460	0.0039	832.9532	0.0039	811.8920	0.0004	795.5283	0.0039	780.0304	0.0038	868.4073
0.0039	868.4073	0.0039	861.4121	0.0039	851.8674	0.0039	832.8159	0.0039	811.8212	0.0005	795.4480	0.0039	779.9572	0.0038	868.4073
0.0039	868.4073	0.0039	861.3345	0.0039	851.7684	0.0039	832.6438	0.0039	811.7322	0.0006	795.3470	0.0039	779.8648	0.0038	868.4073
0.0039	868.4073	0.0039	861.2401	0.0039	851.6479	0.0039	832.4374	0.0039	811.6251	0.0007	795.2255	0.0039	779.7526	0.0039	868.4073
0.0039	868.4073	0.0039	861.1287	0.0039	851.5060	0.0039	832.1962	0.0039	811.4993	0.0008	795.0831	0.0039	779.6204	0.0039	868.4073
0.0039	868.0272	0.0039	860.9991	0.0039	851.3414	0.0039	831.9210	0.0039	811.3547	0.0009	794.9196	0.0039	779.4672	0.0039	868.4073
0.0039	867.9597	0.0039	860.8507	0.0039	851.1537	0.0039	831.6119	0.0039	811.1906	0.0010	794.7344	0.0039	779.2930	0.0039	868.4073
0.0039	867.8839	0.0039	860.6827	0.0039	850.9414	0.0039	831.2690	0.0039	811.0070	0.0011	794.5276	0.0039	779.0969	0.0039	868.4073
0.0039	867.7990	0.0039	860.4937	0.0039	850.7036	0.0039	830.8929	0.0039	810.8033	0.0012	794.2980	0.0039	778.8784	0.0039	868.4073
0.0039	867.7042	0.0039	860.2825	0.0039	850.4391	0.0039	830.4841	0.0039	810.5789	0.0013	794.0457	0.0039	778.6373	0.0039	868.4073
0.0039	867.5987	0.0039	860.0476	0.0039	850.1454	0.0039	830.0425	0.0039	810.3329	0.0014	793.7698	0.0039	778.3729	0.0039	868.4073
0.0039	867.4811	0.0039	859.7873	0.0039	849.8217	0.0039	829.5683	0.0039	810.0651	0.0015	793.4695	0.0039	778.0838	0.0039	868.4073

Table 22: Standard low-Re model data for density at heat flux of 40 kW/m^2

Position [0.0, 1.0, 0.0] (m)-0.8 m	Density-0.8 m (kg/m^3)	Position [0.0, 1.0, 0.0] (m)-1.0 m	Density-1.0 m (kg/m^3)	Position [0.0, 1.0, 0.0] (m)-1.2 m	Density-1.2 m (kg/m^3)	Position [0.0, 1.0, 0.0] (m)-1.4 m	Density-1.4 m (kg/m^3)	Position [0.0, 1.0, 0.0] (m)-1.6 m	Density-1.6 m (kg/m^3)	Position [0.0, 1.0, 0.0] (m)-1.8 m	Density-1.8 m (kg/m^3)	Position [0.0, 1.0, 0.0] (m)-2.0 m	Density-2.0 m (kg/m^3)	Position [0.0, 1.0, 0.0] (m)-0.01 m	Density-0.01 m (kg/m^3)
0.0039	793.8714	0.0035	816.9090	0.0001	810.4592	0.0001	768.9386	0.0039	140.8183	0.0039	137.3532	0.0039	132.0662	0.0039	868.4071
0.0039	794.7955	0.0035	814.7242	0.0002	810.4332	0.0002	768.9088	0.0039	141.0938	0.0039	137.6500	0.0039	132.3789	0.0039	868.4071
0.0039	795.8051	0.0036	812.5020	0.0003	810.3762	0.0003	768.8430	0.0039	141.3943	0.0039	137.9749	0.0039	132.7224	0.0039	868.4071
0.0039	796.9069	0.0036	810.2283	0.0004	810.2890	0.0004	768.7428	0.0039	141.7218	0.0039	138.3302	0.0039	133.0995	0.0039	868.4073
0.0039	798.1079	0.0036	807.8865	0.0005	810.1722	0.0005	768.6081	0.0039	142.0784	0.0039	138.7183	0.0039	133.5134	0.0039	868.4073
0.0039	799.4163	0.0037	805.4575	0.0006	810.0250	0.0006	768.4388	0.0039	142.4669	0.0039	139.1420	0.0039	133.9673	0.0039	868.4073
0.0039	800.8398	0.0037	802.9193	0.0007	809.8478	0.0007	768.2341	0.0039	142.8917	0.0039	139.6037	0.0039	134.4648	0.0039	868.4073
0.0039	802.3860	0.0037	800.2438	0.0008	809.6400	0.0008	767.9941	0.0039	143.3581	0.0039	140.1061	0.0039	135.0096	0.0039	868.4073
0.0039	804.0632	0.0037	797.3959	0.0009	809.4006	0.0009	767.7177	0.0039	143.8732	0.0039	140.6518	0.0039	135.6055	0.0039	868.4073
0.0039	805.8796	0.0037	794.3293	0.0010	809.1297	0.0010	767.4045	0.0039	144.4465	0.0039	141.2430	0.0039	136.2563	0.0039	868.4073
0.0039	807.8426	0.0037	790.9821	0.0011	808.8262	0.0011	767.0533	0.0039	145.0907	0.0039	141.8816	0.0039	136.9661	0.0039	868.4073
0.0039	809.9598	0.0038	787.2675	0.0012	808.4894	0.0012	766.6634	0.0039	145.8232	0.0039	142.5713	0.0039	137.7384	0.0039	868.4073
0.0039	812.2377	0.0038	783.0626	0.0013	808.1183	0.0013	766.2338	0.0039	146.6680	0.0039	143.3232	0.0039	138.5765	0.0039	868.4073
0.0039	814.6821	0.0038	778.1875	0.0014	807.7125	0.0014	765.7630	0.0039	147.6575	0.0039	144.1551	0.0039	139.4830	0.0039	868.4073
0.0039	817.2975	0.0038	772.3681	0.0015	807.2702	0.0015	765.2498	0.0039	148.8367	0.0039	145.0933	0.0039	140.4592	0.0039	868.4073

II-4 SST κ - ω model simulation results data

Table 23: SST κ - ω model data for density at heat flux of 20 kW/m^2

Position [0.0, 1.0, 0.0] (m)-0.8 m	Density-0.8 m (kg/m^3)	Position [0.0, 1.0, 0.0] (m)-1.0 m	Density-1.0 m (kg/m^3)	Position [0.0, 1.0, 0.0] (m)-1.2 m	Density-1.2 m (kg/m^3)	Position [0.0, 1.0, 0.0] (m)-1.4 m	Density-1.4 m (kg/m^3)	Position [0.0, 1.0, 0.0] (m)-1.6 m	Density-1.6 m (kg/m^3)	Position [0.0, 1.0, 0.0] (m)-1.8 m	Density-1.8 m (kg/m^3)	Position [0.0, 1.0, 0.0] (m)-2.0 m	Density-2.0 m (kg/m^3)	Position [0.0, 1.0, 0.0] (m)-0.01 m	Density-0.01 m (kg/m^3)
0.0039	837.1182	0.0039	714.5988	0.0039	664.6717	0.0039	598.4286	0.0039	459.9487	0.0039	359.5194	0.0039	332.3214	0.0001	868.4073
0.0039	837.4637	0.0039	716.3219	0.0039	667.4453	0.0039	603.4453	0.0039	471.4078	0.0039	364.6240	0.0039	336.1731	0.0002	868.4073
0.0039	837.8428	0.0039	718.1860	0.0039	670.3904	0.0039	608.5289	0.0039	484.1429	0.0039	370.7534	0.0039	340.5968	0.0003	868.4073
0.0039	838.2583	0.0039	720.2013	0.0039	673.5143	0.0039	613.7331	0.0039	498.1739	0.0039	378.2333	0.0039	345.6892	0.0004	868.4073
0.0039	838.7140	0.0039	722.3771	0.0039	676.8256	0.0039	619.1808	0.0039	513.4538	0.0039	387.4557	0.0039	351.5604	0.0005	868.4073
0.0039	839.2132	0.0039	724.7241	0.0039	680.3372	0.0039	625.0216	0.0039	529.7603	0.0039	398.8780	0.0039	358.3755	0.0006	868.4073
0.0039	839.7598	0.0039	727.2538	0.0039	684.0682	0.0039	631.2759	0.0039	546.5894	0.0039	413.0591	0.0039	366.6494	0.0007	868.4073
0.0039	840.3582	0.0039	729.9765	0.0039	688.0443	0.0039	637.9221	0.0039	562.9892	0.0039	430.6732	0.0039	377.1581	0.0008	868.4073
0.0039	841.0124	0.0039	732.9016	0.0039	692.2744	0.0039	644.9122	0.0039	578.2476	0.0039	451.8211	0.0039	390.7726	0.0009	868.4073
0.0039	841.7272	0.0039	736.0381	0.0039	696.7572	0.0039	652.1625	0.0039	592.0318	0.0039	476.0622	0.0039	408.3935	0.0010	868.4073
0.0039	842.5073	0.0039	739.3943	0.0039	701.4871	0.0039	659.5413	0.0039	604.2854	0.0039	502.7669	0.0039	430.9194	0.0011	868.4073
0.0039	843.3573	0.0039	742.9773	0.0039	706.4520	0.0039	666.9322	0.0039	615.4553	0.0039	530.7472	0.0039	457.9041	0.0012	868.4073
0.0039	844.2819	0.0039	746.7915	0.0039	711.6343	0.0039	674.3093	0.0039	626.5638	0.0039	557.5400	0.0039	487.4245	0.0013	868.4073
0.0039	845.2854	0.0039	750.8359	0.0039	717.0168	0.0039	681.6929	0.0039	637.9333	0.0039	580.1984	0.0039	517.4884	0.0014	868.4073
0.0039	846.3710	0.0039	755.1022	0.0039	722.5769	0.0039	689.1447	0.0039	649.2151	0.0039	598.2557	0.0039	545.8737	0.0015	868.4073

Table 24: SST k-omega model data for density at heat flux of 40 kW/m^2

Position [0.0, 1.0, 0.0] (m)-0.8 m	Density-0.8 m (kg/m^3)	Position [0.0, 1.0, 0.0] (m)-1.0 m	Density-1.0 m (kg/m^3)	Position [0.0, 1.0, 0.0] (m)-1.2 m	Density-1.2 m (kg/m^3)	Position [0.0, 1.0, 0.0] (m)-1.4 m	Density-1.4 m (kg/m^3)	Position [0.0, 1.0, 0.0] (m)-1.6 m	Density-1.6 m (kg/m^3)	Position [0.0, 1.0, 0.0] (m)-1.8 m	Density-1.8 m (kg/m^3)	Position [0.0, 1.0, 0.0] (m)-2.0 m	Density-2.0 m (kg/m^3)	Position [0.0, 1.0, 0.0] (m)-0.01 m	Density-0.01 m (kg/m^3)
0.0039	837.1182	0.0039	714.5988	0.0039	664.6717	0.0039	598.4286	0.0039	459.9487	0.0039	359.5194	0.0039	332.3214	0.0001	868.4073
0.0039	837.4637	0.0039	716.3219	0.0039	667.4453	0.0039	603.4453	0.0039	471.4078	0.0039	364.6240	0.0039	336.1731	0.0002	868.4073
0.0039	837.8428	0.0039	718.1860	0.0039	670.3904	0.0039	608.5289	0.0039	484.1429	0.0039	370.7534	0.0039	340.5968	0.0003	868.4073
0.0039	838.2583	0.0039	720.2013	0.0039	673.5143	0.0039	613.7331	0.0039	498.1739	0.0039	378.2333	0.0039	345.6892	0.0004	868.4073
0.0039	838.7140	0.0039	722.3771	0.0039	676.8256	0.0039	619.1808	0.0039	513.4538	0.0039	387.4557	0.0039	351.5604	0.0005	868.4073
0.0039	839.2132	0.0039	724.7241	0.0039	680.3372	0.0039	625.0216	0.0039	529.7603	0.0039	398.8780	0.0039	358.3755	0.0006	868.4073
0.0039	839.7598	0.0039	727.2538	0.0039	684.0682	0.0039	631.2759	0.0039	546.5894	0.0039	413.0591	0.0039	366.6494	0.0007	868.4073
0.0039	840.3582	0.0039	729.9765	0.0039	688.0443	0.0039	637.9221	0.0039	562.9892	0.0039	430.6732	0.0039	377.1581	0.0008	868.4073
0.0039	841.0124	0.0039	732.9016	0.0039	692.2744	0.0039	644.9122	0.0039	578.2476	0.0039	451.8211	0.0039	390.7726	0.0009	868.4073
0.0039	841.7272	0.0039	736.0381	0.0039	696.7572	0.0039	652.1625	0.0039	592.0318	0.0039	476.0622	0.0039	408.3935	0.0010	868.4073
0.0039	842.5073	0.0039	739.3943	0.0039	701.4871	0.0039	659.5413	0.0039	604.2854	0.0039	502.7669	0.0039	430.9194	0.0011	868.4073
0.0039	843.3573	0.0039	742.9773	0.0039	706.4520	0.0039	666.9322	0.0039	615.4553	0.0039	530.7472	0.0039	457.9041	0.0012	868.4073
0.0039	844.2819	0.0039	746.7915	0.0039	711.6343	0.0039	674.3093	0.0039	626.5638	0.0039	557.5400	0.0039	487.4245	0.0013	868.4073
0.0039	845.2854	0.0039	750.8359	0.0039	717.0168	0.0039	681.6929	0.0039	637.9333	0.0039	580.1984	0.0039	517.4884	0.0014	868.4073
0.0039	846.3710	0.0039	755.1022	0.0039	722.5769	0.0039	689.1447	0.0039	649.2151	0.0039	598.2557	0.0039	545.8737	0.0015	868.4073

II-5 Standard Wilcox k-omega modelimulation results data

Table 25: Standard Wilcox k-omega model data for heat flux at 20 kW/m^2

Position [0.0, 1.0, 0.0] (m)-0.8 m	Density-0.8 m (kg/m^3)	Position [0.0, 1.0, 0.0] (m)-1.0 m	Density-1.0 m (kg/m^3)	Position [0.0, 1.0, 0.0] (m)-1.2 m	Density-1.2 m (kg/m^3)	Position [0.0, 1.0, 0.0] (m)-1.4 m	Density-1.4 m (kg/m^3)	Position [0.0, 1.0, 0.0] (m)-1.6 m	Density-1.6 m (kg/m^3)	Position [0.0, 1.0, 0.0] (m)-1.8 m	Density-1.8 m (kg/m^3)	Position [0.0, 1.0, 0.0] (m)-2.0 m	Density-2.0 m (kg/m^3)	Position [0.0, 1.0, 0.0] (m)-0.01 m	Density-0.01 m (kg/m^3)
0.0039	799.9296	0.0039	152.8899	0.0039	209.5265	0.0039	168.9424	0.0039	201.8792	0.0039	209.9437	0.0039	209.0749	0.0001	868.4073
0.0039	800.8150	0.0039	153.3720	0.0039	211.2646	0.0039	169.8856	0.0039	203.5001	0.0039	211.6877	0.0039	210.8067	0.0002	868.4073
0.0039	801.7822	0.0039	153.9195	0.0039	213.2042	0.0039	170.9514	0.0039	205.3136	0.0039	213.6334	0.0039	212.7395	0.0003	868.4073
0.0039	802.8378	0.0039	154.5433	0.0039	215.3697	0.0039	172.1582	0.0039	207.3449	0.0039	215.8053	0.0039	214.8981	0.0004	868.4073
0.0039	803.9894	0.0039	155.2566	0.0039	217.7879	0.0039	173.5282	0.0039	209.6227	0.0039	218.2302	0.0039	217.3091	0.0005	868.4073
0.0039	805.2447	0.0039	156.0752	0.0039	220.4883	0.0039	175.0872	0.0039	212.1786	0.0039	220.9369	0.0039	220.0022	0.0006	868.4073
0.0039	806.6110	0.0039	157.0185	0.0039	223.5028	0.0039	176.8659	0.0039	215.0480	0.0039	223.9583	0.0039	223.0087	0.0007	868.4073
0.0039	808.0969	0.0039	158.1102	0.0039	226.8812	0.0039	178.9006	0.0039	218.2686	0.0039	227.3463	0.0039	226.3742	0.0008	868.4073
0.0039	809.7107	0.0039	159.3792	0.0039	230.6994	0.0039	181.2343	0.0039	221.8798	0.0039	231.1767	0.0039	230.1709	0.0009	868.4073
0.0039	811.4607	0.0039	160.8614	0.0039	235.0559	0.0039	183.9176	0.0039	225.9314	0.0039	235.5450	0.0039	234.4899	0.0010	868.4073
0.0039	813.3558	0.0039	162.6008	0.0039	240.0780	0.0039	187.0100	0.0039	230.5197	0.0039	240.5706	0.0039	239.4428	0.0011	868.4073
0.0039	815.4036	0.0039	164.6523	0.0039	245.9296	0.0039	190.5809	0.0039	235.7767	0.0039	246.3968	0.0039	245.1569	0.0012	868.4073
0.0039	817.6110	0.0039	167.0835	0.0039	252.9237	0.0039	194.7111	0.0039	241.8652	0.0039	253.2998	0.0039	251.8268	0.0013	868.4073
0.0039	819.9824	0.0039	169.9780	0.0039	261.7796	0.0039	199.4928	0.0039	248.9868	0.0039	261.8457	0.0039	259.9069	0.0014	868.4073
0.0039	822.5191	0.0039	173.4388	0.0039	273.3281	0.0039	205.0272	0.0039	257.6676	0.0039	272.4861	0.0039	269.7343	0.0015	868.4073

Table 26: Standard Wilcox k-omega model data for heat flux at 40 kW/m^2

Position [0.0, 1.0, 0.0] (m)-0.8 m	Density-0.8 m (kg/m^3)	Position [0.0, 1.0, 0.0] (m)-1.0 m	Density-1.0 m (kg/m^3)	Position [0.0, 1.0, 0.0] (m)-1.2 m	Density-1.2 m (kg/m^3)	Position [0.0, 1.0, 0.0] (m)-1.4 m	Density-1.4 m (kg/m^3)	Position [0.0, 1.0, 0.0] (m)-1.6 m	Density-1.6 m (kg/m^3)	Position [0.0, 1.0, 0.0] (m)-1.8 m	Density-1.8 m (kg/m^3)	Position [0.0, 1.0, 0.0] (m)-2.0 m	Density-2.0 m (kg/m^3)	Position [0.0, 1.0, 0.0] (m)-0.01 m	Density-0.01 m (kg/m^3)
0.0039	799.9296	0.0039	152.8899	0.0039	209.5265	0.0039	168.9424	0.0039	201.8792	0.0039	209.9437	0.0039	209.0749	0.0001	868.4073
0.0039	800.8150	0.0039	153.3720	0.0039	211.2646	0.0039	169.8856	0.0039	203.5001	0.0039	211.6877	0.0039	210.8067	0.0002	868.4073
0.0039	801.7822	0.0039	153.9195	0.0039	213.2042	0.0039	170.9514	0.0039	205.3136	0.0039	213.6334	0.0039	212.7395	0.0003	868.4073
0.0039	802.8378	0.0039	154.5433	0.0039	215.3697	0.0039	172.1582	0.0039	207.3449	0.0039	215.8053	0.0039	214.8981	0.0004	868.4073
0.0039	803.9894	0.0039	155.2566	0.0039	217.7879	0.0039	173.5282	0.0039	209.6227	0.0039	218.2302	0.0039	217.3091	0.0005	868.4073
0.0039	805.2447	0.0039	156.0752	0.0039	220.4883	0.0039	175.0872	0.0039	212.1786	0.0039	220.9369	0.0039	220.0022	0.0006	868.4073
0.0039	806.6110	0.0039	157.0185	0.0039	223.5028	0.0039	176.8659	0.0039	215.0480	0.0039	223.9583	0.0039	223.0087	0.0007	868.4073
0.0039	808.0969	0.0039	158.1102	0.0039	226.8812	0.0039	178.9006	0.0039	218.2686	0.0039	227.3463	0.0039	226.3742	0.0008	868.4073
0.0039	809.7107	0.0039	159.3792	0.0039	230.6994	0.0039	181.2343	0.0039	221.8798	0.0039	231.1767	0.0039	230.1709	0.0009	868.4073
0.0039	811.4607	0.0039	160.8614	0.0039	235.0559	0.0039	183.9176	0.0039	225.9314	0.0039	235.5450	0.0039	234.4899	0.0010	868.4073
0.0039	813.3558	0.0039	162.6008	0.0039	240.0780	0.0039	187.0100	0.0039	230.5197	0.0039	240.5706	0.0039	239.4428	0.0011	868.4073
0.0039	815.4036	0.0039	164.6523	0.0039	245.9296	0.0039	190.5809	0.0039	235.7767	0.0039	246.3968	0.0039	245.1569	0.0012	868.4073
0.0039	817.6110	0.0039	167.0835	0.0039	252.9237	0.0039	194.7111	0.0039	241.8652	0.0039	253.2998	0.0039	251.8268	0.0013	868.4073
0.0039	819.9824	0.0039	169.9780	0.0039	261.7796	0.0039	199.4928	0.0039	248.9868	0.0039	261.8457	0.0039	259.9069	0.0014	868.4073
0.0039	822.5191	0.0039	173.4388	0.0039	273.3281	0.0039	205.0272	0.0039	257.6676	0.0039	272.4861	0.0039	269.7343	0.0015	868.4073